Theoretical study of ligand migration in Hemeproteins: Truncated Hemoglobin N and Nitrophorin 7

Ana Luísa Novo de Oliveira

Departament de Fisicoquímica
Facultat de Farmàcia
Universitat de Barcelona

Theoretical study of ligand migration in Hemeproteins: Truncated Hemoglobin N and Nitrophorin 7

Ana Luísa Novo de Oliveira
2013

Programa de doctorado de Biotecnologia (2010-2013)
Directores: Dr. F. Javier Luque Garriga y Dr. Axel Bidon-Chanal Badia

UNIVERSITAT DE BARCELONA

FACULTAT DE FARMÀCIA

DEPARTAMENT FISICOQUIMICA

PROGRAMA DE DOCTORAT DE BIOTECNOLOGIA

THEORETICAL STUDY OF LIGAND MIGRATION IN PROTEINS:

TRUNCATED HEMOGLOBION N AND NITROPHORIN 7

Memòria presentada per Ana Luísa Novo de Oliveira per optar al títol de doctor per la Universitat de Barcelona

Javier Luque Garriga

Axel Bidon-Chanal Badia

Ana Luísa Novo de Oliveira

Esta tesis doctoral fue realizada en el departamento de Fisicoquímica de la Facultad de Farmàcia de la Universidad de Barcelona bajo la dirección de los Dr. F. Javier Luque y Axel Bidon-Chanal.

El presente trabajo fue financiado por el Ministerio de Educación y Ciencia (proyectos SAF2008-05595-C02-00, PCI2006-A7-0688, PIB2010-AR-00455) y por la comisión europea (proyecto FP7-HEATH-2007-B-223335). Los cálculos computacionales fueran realizados al supercomputador Mare Nostrum del Barcelona Supercomputing Center.

À tia Lila,

Agradecimientos

A todas aquellas personas que en algún momento durante estos últimos 4 años me han ayudado en modo alguno en la realización de esta tesis, quisiera darles las gracias.

Esta etapa nunca poderia ter começado sem as curiosidades que o Dr. Pedro Alexandrino Fernandes despertou em mim ainda durante a licenciatura em Bioquímica.

Sin embargo, sólo se tornó realidad porque mis directores de tesis, Prof. Javier Luque y Dr. Axel Bidon-Chanal, creyeron en mí. Os lo agradezco, por la oportunidad que me habéis dado y por haberme formado.

A mis compañeros de grupo, con los que disfruté en el trabajo, Carles, Campa, Jordi y Salomé, Marina, Silvana, Andreana y a los que ya no están, como Ignacio, Patricio y Flavio, pero que siguen estando presentes.

Al Dr. Xavier Barril y sus "Xavi's", mis compañeros y amigos: Montse, Dani, Yvonne, Mousumi, Sergi, Kevin, Aida y Laura, por todo lo que hemos compartido, sea científicamente, sea personalmente, habéis marcado mi etapa en Barcelona. Porque trabajar con vosotros significa aprender día a día y disfrutar.

Quiero agradecer a los que me acogieron durante mis estancias fuera, en Parma: Prof. Cristiano Viapiani y Francesca Spyrakis, en la India: Dr. Kanak Dikshit, Chahaat y Sandeep, y en Argentina: Dr. Adrian Turjansky, Dr. Marcelo Marti y Prof. Dario Estrín.

A los compañeros y amigos con quiénes, fuera, compartí muchas experiencias: Pau, Susan y Lucas.

A mis amigos Jonh, Magdalena y Anna García, por siempre haberen estado a mi lado; e aos que apesar da distancia sempre me animaram: Catarina, Cristina e André Teixeira.

A mi grande amigo Dr. Ramon Pouplana, le agradezco por todo el apoyo y cariño, por las tertulias que tanto disfruté, y sobretodo por orientarme y ser un ejemplo a seguir. Muchas gracias "Gamon"!

Por otro lado, quiero agradecer a mi familia catalana: Assumpta, Ramon y Marta. Os agradezco muchísimo porque siempre me recibiste con todo el cariño y siempre me he sentido como en casa, y sin embargo… estoy tan lejos!

Muito obrigada a toda a minha família, aos meus Avós, ao Tio Nelo e Paula, aos tios Dino e Julieta e sobretudo, à Tia Lila e Tia Nene, por formarem um pilar sólido na minha vida.

E finalmente, quero agradecer aos meus pais, porque nunca seria quem sou sem a vossa ajuda, apoio e carinho!

ABSTRACT

The diversity of functional roles played by heme proteins in all kingdoms of life is to a large extent regulated by the thermodynamic and kinetic properties of their interaction with small gaseous molecules.

The aim of this PhD thesis is to examine the structural and dynamical properties of two hemeproteins, the truncated hemoglobin N from *M. Tuberculosis* and nitrophorin 7 from *R. Proxilus*, and to examine their relationships with the biological role of these proteins. Particular attention has been paid to the diffusion of small ligands between the internal cavities in the two hemeproteins, and the entry/release pathways from the protein matrix to the solvent. Qualitative and semi-quantitative agreements between experiment and simulations are obtained for the identities of the cavities that physically trap the ligand and for the connections between them.

The truncated hemoglobin N (trHbN) is believed to constitute a defense mechanism of *M. Tuberculosis* against NO produced by the macrophages during the initial growth infection stage, which is converted to the harmless nitrate anion, through the chemical reaction $NO + FE_{(II)}\text{-}O_2 \rightarrow FE_{(III)} + [NO_3]^-$. The dual path ligand-dependent mechanism proposed in previous studies of the group ensures the access of NO to the heme cavity in the oxygenated form of the protein, which should warrant survival of the microorganism under stress conditions and allowing the bacillus to stay in latency. As a consequence, the processes mediated by trHbN are worth for searching a therapeutical intervention, since the inactivation of the NO scavenging should reduce significantly the bacteria resistance.

In this work we have validated the importance of the PheE15 residue in the previous proposed dual path mechanism, as PheE15 was proposed to act as a gate that regulates the access of NO to the heme cavity in the oxygenated form of the protein. Thus, we have studied the impact of three residue mutations of the gate residue, PheE15Ala, PheE15Ile and PheE15Tyr, in the ligand migration mechanism and in the NO detoxification activity. The results support the gating role played by PheE15, because all the mutations are predicted to either block the long branch of the tunnel (PheE15Ile, PheE15Tyr) or to induce structural alterations that affect the passage of NO at the entrance of the tunnel (PheE15Ala).

After release of the NO_3^- anion, the protein, which rests in its ferric form, is assumed to be recycled by a putative reductase, rendering trHbN in the ferrous form suitable to bind a new O_2 molecule, thus ensuring an efficient detoxification mechanism. In order to gain insight into the reduction process, we have examined the interaction between trHbN and a flavodoxin reductase (FdR) from *E. Coli*, which has shown to be very efficient in restoring the ferrous form of the protein. Thus, our studies have yielded a 3D model of the complex between trHbN and FdR, which allows to identify the residues implicated in the binding of the two proteins. Moreover, the model predicts that the heme and flavin cofactors are close (between 6 and 9 Å) in the complex, which facilitates an efficient electron transfer, as reinforced by the calculated electron couplings.

Nitrophorin 7 is a hemeprotein implicated in the NO transport, which can be found in the saliva of blood feeding insects. One of the bugs, *Rhodnius prolixus*, is the causative agent of Chagas disease, and is responsible for a high number of deaths (approximately 15000 each year). Among the nitrophorin family, we have examined nitrophorin 7, which presents three extra residues in N-terminal sequence and the unique ability to bind membranes negatively charged. The results point out the existence of up to three inner cavities, which may define an internal pathway for migration of a gaseous ligand (NO) from the heme to the back of the protein. This topological feature is not present in other nitrphorins, such as NP4, and justifies a more complex kinetic rebinding scheme in NP7. In conjunction with the ability to interact with membranes, these findings might support a specific role in NO-controlled release.

Both projects are carried out in closed collaboration with experimental groups, and we believe that in the future such collaborations will allow the development of new strategies with therapeutically implications in these diseases.

RESUMEN

El proyecto desarrollado en esta tesis tiene por objeto el estudio de los aspectos dinámicos del transporte de ligandos en dos hemoproteínas: la hemoglobina truncada N de *Mycobacterium tuberculosis*, y la nitroforina NP7 de *Rhodnius prolixus*.

La primera desempeña un papel muy importante como mecanismo de defensa del microorganismo que causa la enfermedad de Tuberculosis y su transmisión, *Mycobacterium tuberculosis*, al transformar el óxido nítrico (NO) generado por los macrófagos en anión nitrato durante las etapas iniciales de la infección mediante la reacción $NO + FE_{(II)}\text{-}O_2 \rightarrow FE_{(III)} + [NO_3]^-$. Mientras que el anión nitrato es inocuo, el óxido nítrico destruye la cadena respiratoria de la bacteria causando así su muerte. Con este mecanismo, el microorganismo es capaz de subsistir en estado latente dificultando su completa eliminación y la total recuperación del paciente de tuberculosis.

En consecuencia, dicha proteína aparece como una diana de potencial valor terapéutico dado que su inactivación debería reducir significativamente la resistencia del microorganismo. Para abordar esta posibilidad, en primer lugar se ha validado el modelo propuesto de mecanismo de transporte de ligandos mediante el examen de diversos mutantes: PheE15Ala, PheE15Ile y PheE15Tyr obtenidos al modificar el residuo que controla la migración a través del canal para la llegada de oxígeno y óxido nítrico al centro activo, y en segundo lugar se ha estudiado el mecanismo de reconversión de la forma oxidada a la forma reducida una vez liberado el anión nitrato.

Las nitroforinas son hemoproteínas transportadoras de NO que se hallan en la saliva de insectos que se alimentan de sangre. Uno de ellos, *Rhodnius prolixus*, es el causante de la transmisión la enfermedad de Chagas, que causa aproximadamente 15000 muertes por año. De entre los diversos tipos de nitroforinas, nuestro interés se centra en la nitroforina 7 (NP7) que difiere en el extremo N-terminal respecto a otras nitroforinas y en su capacidad de unión a membranas cargadas negativamente. El objetivo del trabajo se centra en determinar el efecto de dichas diferencias sobre la capacidad de captación y transporte de NO.

En ambos casos, los proyectos se llevan a cabo en colaboración con grupos experimentales, y confiamos que dicha colaboración permita abrir en el futuro nuevas vías de intervención terapéutica para estas enfermedades.

INDEX

Chapter 1: Introduction

1. Iron and life

Iron is one of the most abundant elements in the earth's crust, and most organisms have developed mechanisms that make use of iron to regulate biochemical processes fundamental for their living. Aerobic organisms use iron in the intracellular respiration, oxygen transport and storage, nitrogen fixation and photosynthesis and energy generation (1). Furthermore, in its ferrous state iron is highly reactive: Fe^{2+} may transfer an electron to hydrogen peroxide produced from the oxygen metabolic pathways in aerobic organisms, then generating a hydroxyl radical through the Fenton reaction that causes damage to proteins, lipids and DNA, and results in cell death. Accordingly, the biochemical role of iron must be finely controlled in order to avoid damage by radical species (2).

To exert its functional role, the iron is generally associated to hemeproteins that contains an iron-porphyrin complex as a prostetic group (3). They perform a wide variety of tasks ranging from electron transport to oxidation of organic compounds, sensing and transport of small molecules, like O_2, CO and NO, electron transfer and chemical reactions, such as NO detoxification. (4,5,6).

Hemeproteins play a crucial function in all aspects of NO biology: NO generation (i.e., NO synthase) (7), NO transport (i.e., nitrophorins) (8), and NO sensing (i.e., guanylate cyclase) (9). Another important role played by NO is related to the immunological response, since the macrophages release NO as a defense mechanism in front of infectious organisms (10). The NO release pursues to inactivate key metabolic enzymes used by the pathogens, such as the terminal respiratory oxidases and superoxide dismutase. This mechanism usually is carry out by heme proteins, especially globins (11).

2. The complex ligand- protein

The affinity of gaseous ligands and their kinetic rate constant for association and dissociation are key parameters for gaining insight into the function of globins. The protein-ligand complex reflects a dynamical equilibrium that implicates 3 species: free ligand, free protein and the complex formed by the interaction between the two. This equilibrium can be translated by the follow chemical equation:

$$[E] + [L] \rightarrow [EL]$$

The affinity of a protein for a ligand is characterized by the equilibrium constant K, which in turn can be related with the ratio between the apparent kinetic rate constants for the association and dissociation processes, called k_{on} and k_{off}, respectively. k_{off} is inversely proportional to the half life of the complex [(ES)], while k_{on} is biomolecular and reflects the probability of the complex formation.

The association rate constant depends on two processes:

i) ligand migration from the solvent to the heme active site, and

ii) ligand coordination to the heme iron (12).

The ligand migration through the protein matrix is regulated by the presence of internal pockets or even tunnels. Often, the ligand accesses the protein using one or more internal transient channels of the enzyme that connect with the protein surface. These channels can be controlled by conformational changes on the amino acid side chains, the presence of specific residues that are capable to act as "gates" or by the high flexibility exhibited by loops (13). In some cases, a distal site residue (mainly His, Tyr) is able to bind to the Fe atom in the so-called internal hexacoordination, which affects the entire process (14). In addition, non-coordinated water molecules located in the distal site can also modulate the k_{on}, adding another variable to the complexity of the association process (15).

The coordination step depends on the spin state of the ligand and the relative in-plane position of the iron (16). For these reasons, in most cases the value of k_{on} for O_2 is higher than for CO, whereas the kon value for NO is even higher (17). The association rates span a wide range of values (spanning up to five orders of magnitude), starting at about 10^4 $M^{-1}s^{-1}$ in those systems with very low accessibility to the iron, and rising to 10^9 $M^{-1}s^{-1}$ when the association rate is mainly controlled by the diffusion from the solvent to reach the protein, as observed for isolated porphyrins (18).

The dissociation constant (k_{off}) involves two processes: i) thermal breaking of the protein-ligand interactions, and ii) ligand escape from the active site into the solvent. The dissociation rate constants are generally regulated mainly by the protein-ligand thermal breaking step. It is mainly determined by the nature of interaction between the ligands and the heme protein, which depends upon the strength of the iron-ligand bond, and on interactions involving the protein matrix, like H bond interactions between the ligand and the surround amino acids. On the basis of these interactions, the dissociation rate constant spans a range of roughly seven orders of magnitude (i.e., from 10^{-3} s^{-1} to 10^4 s^{-1}; (19)). Both diffusion and breaking of protein-ligand interaction are processes

that vary from ligand to ligand, thus leading to a wide range of ligand affinities.

Oxygen binds exclusively to ferrous heme, and its dissociation rate constant is strongly influenced by interactions between the coordinated O_2 and the protein matrix (20). For CO and NO, the dissociation from ferrous heme is mostly dominated by breaking of the Fe-ligand bond, and similarly low values ($\approx 1 \times 10^{-2}$ s^{-1}) are observed for many different proteins. In the O_2 case, the energy required for breaking the protein-ligand bond is regulated by several factors (21), including:

a) distal effect, which accounts for the interaction of the ligand with hydrogen-bond donor residues present in the distal cavity,
b) proximal effect, which takes into account the influence of the local structure of the axial histidine, and
c) heme distortion, which alters the strength of the Fe-ligand bond.

The diffusion can be the limitant reaction step in cases that the reaction is much more faster than the dissociation of the complex. In these proteins, the catalitical efficiency uses to be very high to allow that all the substract that reaches the active site is converted in product.

3. Globins

Globins are a family of heme-containing proteins found in all kingdoms of life. They belong to the hemeprotein superfamily, though they share some distinctive characteristics. The globin folding was identified in 1958 in myoglobin (Mb) (22), which was the first protein whose structure became solved by X-ray diffraction and in this sense, the *globin fold* was the first protein fold to be discovered.

Currently, in the Protein Data Bank more than 2300 hemeproteins can be found, and they can be clustered in 34 different groups with very diverse structural and functional characteristics (23). As members of this superfamily, globins are supposed to have evolved from a common ancestor and their characteristic tertiary structure is typically known as *globin fold*.

The *globin fold* is an all-alpha protein fold, since the only secondary structure found is the alpha-helix. Though primary sequences of globins can have as low as 16% sequence identity, the *globin fold* is highly conserved throughout the family. Typically, it consists of 3 alpha helices that are superposed onto another set of three helices

(A/BC/E and F/G/H helices), forming the 3-over-3 sandwich motif (see Fig.1).

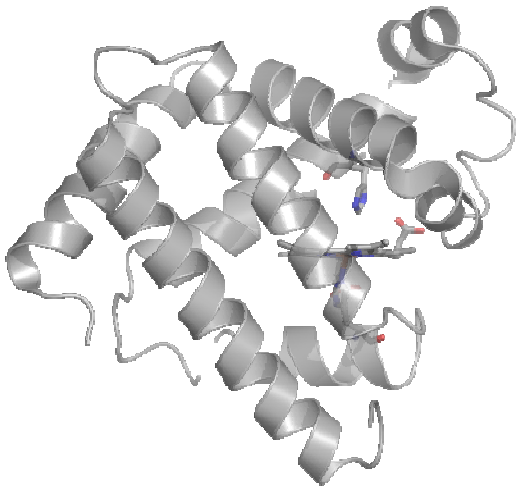

Figure 1: 3-over-3 helical sandwich folding of sperm whale Myoglobin (PDB ID. 1VXA) X–ray structure

Globins have evolved to play a variety of biological roles, such as transport and sensing of gases and catalysis of reactions between nitrogen and reactive oxygen species (21). Some of them are present as monomers under physiological conditions, though others form multimeric species, as illustrated by the prototypical cases of mammalian Mb –monomeric– and hemoglobin (Hb) –tetrameric (24,25).

As mentioned before, globins generally adopt a common *globin fold*, which contains the hydrophobic pocket that accommodates the heme group. The heme iron is coordinated to the only fully conserved residue along this family: the proximal HisF8 (26), leaving the sixth coordination position in the distal side usually free for binding of the exogenous ligand. Typical exogenous ligands are NO, CO and O_2, being molecular oxygen the most abundant and the one with the lowest affinity for free heme.

In most of the hemeproteins, the active site, where one of these small ligands can bind, consists on a cavity on the top of the heme group usually known as distal pocket (Fig. 2). The iron atom is coordinated equatorially to the four nitrogens of the porphyrin macrocycle, and axially to a fifth or proximal ligand under the heme ring, typically a His, Cys or Tyr residue.

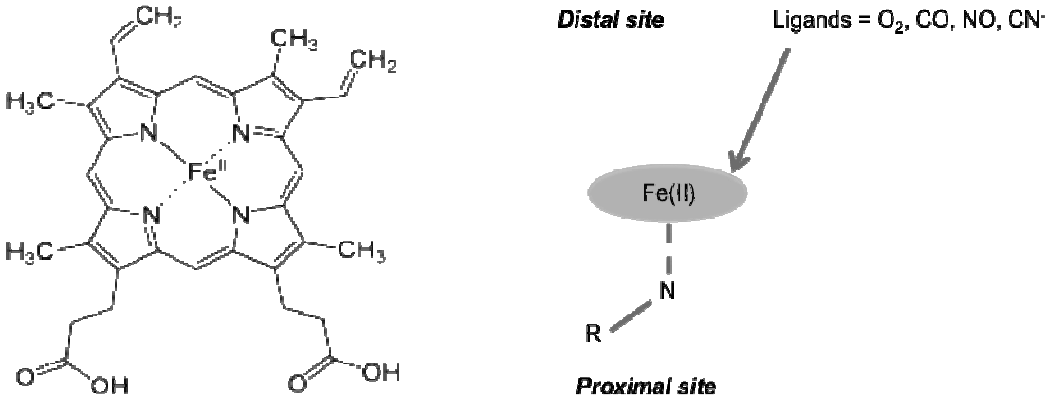

Figure 2. Schematic representation of hemeproteins active site.

3.1 Truncated Hemoglobins

In the last decades new members of the globin family have been discovered, greatly expanding the globin world. Globins are widely distributed in all kingdoms of life and exhibit an intricate and complex phylogenetic network, which has been proposed to be divided in three main lineages (27). The novel globins show distinct structural and functional features when compared to mammalian Mb and Hb. Apart from the canonical 3/3 Mb fold, which encompasses many different globins, another lineage shows a characteristic fold denoted as 2/2 Hb, which has been found in the three domains of life (28).

Among the globins that have been classified as 2/2 Hb are the truncated hemoglobins (trHbs). These are around 20 to 30 residues shorter than Mb and exhibit a 2-over-2 sandwich fold involving only B/E and G/H helices, in contrast to the classical 3-over-3 fold.

The 2/2 Hbs have been proposed to act as small gas molecule sensors, oxygen carriers and pseudoenzimes (29). In some cases, they have been related to the defense of the bacteria against nitrosative stress (30) and are present in bacteria, unicellular eukaryotes and higher plants.

The 2/2 Hb family can be further divided into three groups: I, II, III also known as N, O and P. It has been shown that certain Hbs that are present in some microorganisms are related to its ability to detoxify NO (31,32). This defense mechanism would be related to O_2-bound globins that could convert NO to nitrate anion following the reaction Fe(II) - O_2 + NO → Fe(III) + NO_3^-. In *M. tuberculosis* two 2/2

Hbs are capable of performing such detoxifying reaction: *truncated Hb N* and *truncated Hb O.*

On the present thesis we will focus on group I trHbs, and more specifically on the truncated hemoglobin N from Mycobacterium tuberculosis.

3.1.1. The tuberculosis epidemiology

Current epidemiological statistics indicate that about one-third of the world human population is latently infected with *Mycobaterium tuberculosis*, the causative agent of Tuberculosis (33). In most healthy individuals, the initial *M. Tuberculosis* infection is contained by the immune system, which forces the bacteria to enter a latent state for several years with possible reactivation later in life. The initial event after infection involves multiplication of *M. Tuberculosis* inside the host macrophage. Later infected macrophages are isolated from the circulation by newly recruited macrophages to form the so-called gaseous granuloma, whose chemical environment restricts growth of the bacteria (34).

Several independent lines of evidence indicate that macrophage-generated oxygen and nitrogen reactive species can restrict the development of *M. Tuberculosis* infection in host. Interestingly, nitric oxide and related reactive species are produced by inducible NO-synthase in the macrophages during the initial infection stage, and may be involved in restricting the bacteria during latent stage (35).

The gene encoding for the soluble trHb of the cyanobacterium *Nostoc commune* trHb is coexpressed with genes of the nitrogen fixation complex, and is expressed only under anaerobic conditions (36).

The dynamical balance/competition between host immunity and mycobacterium growth has been related to the presence of an endogenous mechanism for NO resistance, whereby oxygenated *M. tuberculosis* trHbN could scavenge macrophage NO through a deoxygenated reaction (yielding nitrate) as observed in human oxy-Hb, oxy-Mb and *E.coli* flavohemoglobin.

3.1.2 The Mt-trHbN case

As a member of the 2/2 Hb family, trHbN tertiary structure is based on a 2-over-2 alpha helical sandwich rather than the 3–over-3 alpha-helical sandwich of the classical

Hb fold. The heme linked proximal HisF8 is the only residue conserved throughout the Hb and trHbN families (37). An unprecedented N-terminal alpha-helix and an extended cavity/tunnel system, which may be a conserved route for ligand diffusion to/from the heme, are the main characteristics that differentiate trHbN from other truncated hemoglobins.

The crystal structure of the oxygenated Mt-trNHb (PDB code 1IDR (38), displays two perpendicular tunnels: the so-called Short Tunnel (ST), which is around 8 Å long and is delineated by residues in helices G and B, and the Long Tunnel (LT), which is around 20 Å long and is mainly defined by helices B and E (See Fig. 3). The access to the LT is located between the AB and GH hinge regions, while the second tunnel access (ST) is defined by the G and H helix residues AlaG9(95), LeuG12(98) and IleH11(119).

As a consequence, the tunnel can be seen as two orthogonal branches, with a diameter of 5 to 7Å, with one restriction (4Å) at the mutually facing residues PheE15(62) and LeuG12(98). The residues defining both tunnel access sites and lining the inner surface are all of apolar nature.

The heme pocket falls in the intersection of the two tunnel branches, where the distal residues TyrB10(33) and GlnE11(58) are located.

A network of hydrogen bonds stabilizing the exogenous ligand in the heme distal site is found in all three groups of truncated hemoglobins that greatly contribute to this high affinity. Thus, the high oxygen affinity of trHbN (p_{50} ~ 0,001mmHg) may ensure a low but critical oxygen level, granting survival of *M. tuberculosis* in the granuloma hypoxic environment when the bacilli enter latency (39).

The crystal structure also reveals that PheE15, which is placed in the middle of the LT, may adopt two conformations defined by a rotation of ~63º along the C_{α}-$C_{ß}$ bond. In one conformation, the benzene ring is parallel to the tunnel axis, while in the other it is roughly perpendicular, which will be denoted open and closed states, respectively (40). Thus, PheE15(62) may reflect a gating role played by this residue in modulating ligand diffusion to/from the heme iron atom, along the longer branch (41).

Such hypothesis, together with the finding that NO-dioxygenase activity in trHbN is limited by the rate of ligand diffusion to the heme cavity, stimulated several experimental and theoretical studies of the *wild type* protein and several mutants.

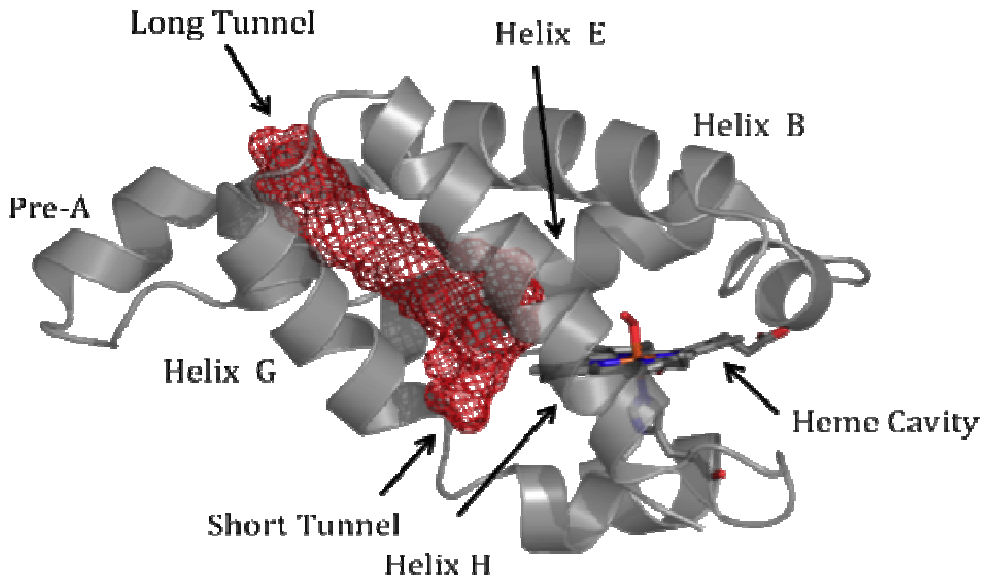

Figure 3. 2-over-2 helical sandwich folding of Truncated Hemoglobin N from *Mycobacterium Tuberculosis* (PDB ID. 1IDR) -ray crystal structure of oxy-trHbN, showing the labels of the helices, the location of the heme group and the two branches of the tunnel system. The long branch (20 Å long) is vertical in the figure, and can be seen as roughly perpendicular to the heme distal face. The short branch (8 Å long) lies roughly parallel to the heme plane (horizontal in the figure), accessing the heme distal site pocket from the inner part of the heme crevice. Residues 1–15 build the N-terminal tail.

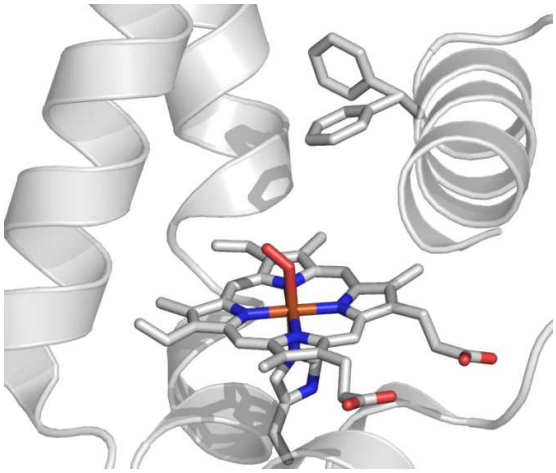

Figure 4. Conformational change of PheE15 side chain along the C_α–C_β dihedral angle leading to *open* and *closed* states viewed along the tunnel long branch leading to the heme in oxy-trHbN.

In agreement to the published studies, the proposed mechanism seems to occur in two steps:

1) ***The access of O_2 through the tunnel short branch (see image) and the subsequent binding to the heme group, rendering the oxygenated protein, which leads to the rearrangement of helices B and E.***

$$FE_{(II)} + O_2 \rightarrow FE_{(II)}\text{-}O_2$$

Oxygen entry is supposed to be achieved through the ST, as supported by the free energy profiles for ligand migration through this tunnel for the oxygenated and deoxygenated forms (42).

In the deoxygenated protein, the GlnE11 and TyrB10 residues interact by hydrogen bonding between the amide group in GlnE11 and the hydroxyl group in TyrB10. The union of O_2 to the hemeporphyrin leads the TyrB10 to form a hydrogen-bond with the heme-bound O_2 which may polarize the gas molecule, promoting partial electron transfer from the heme Fe atom and stabilizing the species with partial superoxide character (43).

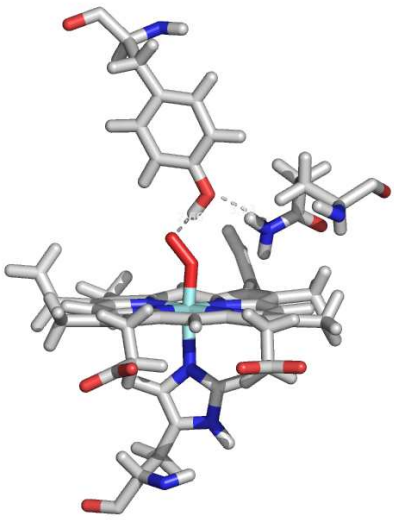

Figure 5. Representation of the active site hydrogen bond network: O_2, TyrB10 and GlnE11.

On the other hand, the hydrogen bond between the diatomic ligand and TyrB10 forces GlnE11 to adopt a folded conformation in order to maintain a hydrogen-bond network with TyrB10 and O_2 molecule. The GlnE11 primarily found in an extended *all-trans* conformation changes its conformation to *gauche* conformational state (see figure 5), thus the side chain of GlnE11 is now much closer to PheE15, and the thermal fluctuations of the side chains may favor the conformational change in PheE15, which triggers the afore mentioned opening events (44).

The dioxygen ligand in trHbN is fully buried within the distal active site cavity. In fact, due to the orientation of the E helix close to the heme distal site, and to the location of the side chains of ThrCD4(49), ArgE6(53), LeuE7(54) and LysE10(57), solvent access to the distal heme cavity through the classical E7-gate path is completely impaired.

This is consistent with the free energy barrier for the open/closed torsional transition obtained by *Umbrella Sampling*: while the open↔closed transition involves a barrier of 3 kcal/mol in the oxygenated protein, the barrier increases up to 6 kcal/mol in the deoxygenated protein (Fig. 6) (45).

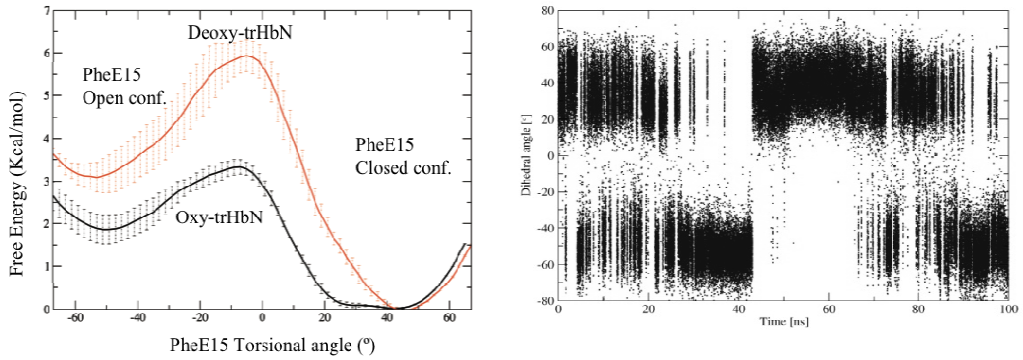

Figure 6: (Left) Potential of mean force for the conformational change in PheE15 C_α–$C_\beta$dihedral angle leading to conversion between open and closed states in deoxy- and oxy-trHbN. (Right) Open and closed transition states of PheE15 are characterized by the torsional dihedral Hα-Cα-Cβ-Cγ

2) The protein oxygenated is now able to facilitate the diffusion of nitric oxide, which should access the protein by the long branch of the tunnel.

The access of NO to the ligand heme cavity in the oxygenated form of Mt-trHbN was proposed to occur mainly through the LT. This process may be regulated by several transitions between two conformational states of PheE15, in agreement with the conformational flexibility seen in the X-ray structure. The functional implications of these findings analyzed by *Multiple Steered Molecular Dynamics* simulations coupled with Jarzinski's equality revelead that when PheE15 is in the open conformation, a small barrier (around 2 kcal/mol) has to be surpassed in order to access the heme cavity. On the other hand, for the closed state access to the active site is accompanied by a step increase in the free energy, leading to a barrier of around 5 kcal/mol (Fig. 7) (45).

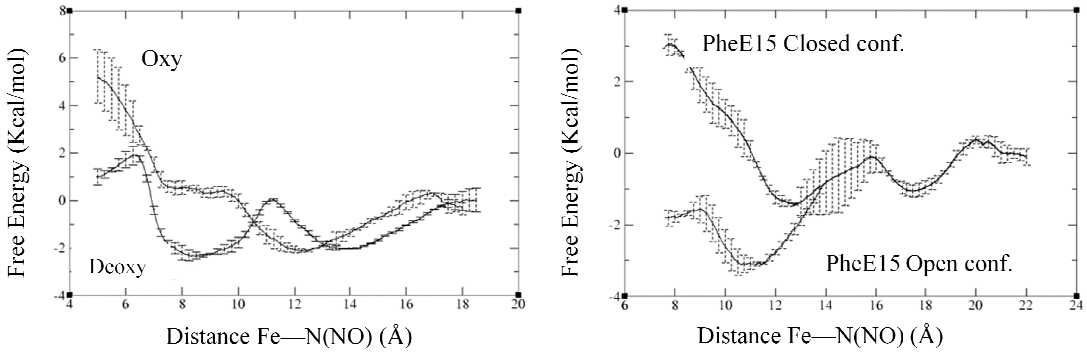

Figure 7. (Left) Free energy profile for diatomic ligand (NO) migration along the short tunnel branch deoxy-trHbN and oxy-trHbN; (Right) Free energy profile for diatomic ligand (NO) migration along the long tunnel branch. The distance from the Fe atom to oxygen (NO) atoms is used as the driven coordinate.

3) ***Next, the NO reaches the heme cavity, and is transformed to nitrate anion, which is then released-assisted by hydration water molecules that enter the heme cavity.***

$$NO + FE_{(II)}\text{-}O_2 \rightarrow FE_{(III)} + [NO_3]^-$$

The formation of NO_3^- anion generates a re-organization of the residues that surround the distal cavity, thus lead the access of water molecules to the heme cavity, and to the formation of a new tunnel located at the loop CD. As a consequence of the presence of water molecules, the Fe - NO_3^- bound is weakened, favoring the disruption of the bond and the release of NO_3^- anion. The estimated energy barrier is under 4Kcal/mol, and should occur in a small fraction of time (Fig. 8) (46).

After release of the NO_3^- anion, the protein is assumed to be recycled by a flavodoxin reductase, rendering trHbN suitable to bind a new O_2 molecule, thus ensuring an efficient detoxification mechanism.

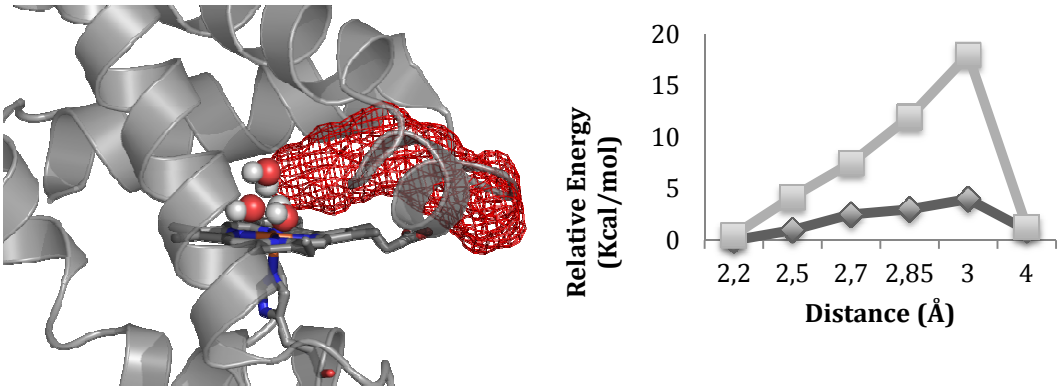

Figure 8: (Left) Representative egression pathway of the solvated nitrate anion in trHbN. The heme group and TyrB10 are shown as sticks. The egression pathways are shown in dark yellow. (Right) Energy profile (kcal/mol) obtained for the breaking of the Fe−O bond (distance in Å) for the heme-bound nitrate anion in the wet large (△) and dry ( ) models.

4. Nitrophorins

4.1. The Lipocalin fold

Lipocalins are found in all types of living organisms and serve a variety of functions from hormone transport to coloration (47). Normally, lipocalins act by binding a small-molecule ligand, but they can also act by binding proteins in solution or receptors.

Blood feeding in insects has evolved independently multiple times, resulting in a diverse array of molecules designed to circumvent host hemostatic defenses (48). Among the most remarkable of these substances are the Nitrophorins (NPs), hemeproteins found in the saliva of the bug *Rhodnius proxilus*, which can act as a vector of the parasite *Trypanosoma cruzi*, the causative agent of Chagas disease (49).

In the process of blood feeding, arthropods must overcome the physiological defense response of the host. Ingestion of blood would be impossible without some mechanism to inhibit normal clotting processes. Additionally, penetration of the skin and vasculature during feeding evokes an inflammatory response that may lead to defensive behavior by the host, and longer term attachment can cause immune responses that negatively affect feeding (50,51). The major role of salivary proteins in arthropods is to overcome these obstacles and maintain a free flow of blood through the

mouthparts and into the gut, this is accomplished through the combined action of numerous salivary proteins and, in some cases, small molecules acting together to inhibit the coagulation cascade, limiting platelet activation and prevent vasoconstriction responses. Depending on necessity, additional substances may be present that modulate inflammatory and immune responses (52).

As referred in a previous section, in the mammalian host, NO is a hormone-like molecule produced by the vascular tone. By activating soluble guanylate cyclase, NO stimulates signaling pathways that ultimately result in relaxation of the vascular wall (53). NO is also produced by immune effector cells as a toxicant aimed at invading microorganisms, and is important as a platelet aggregation inhibitor.

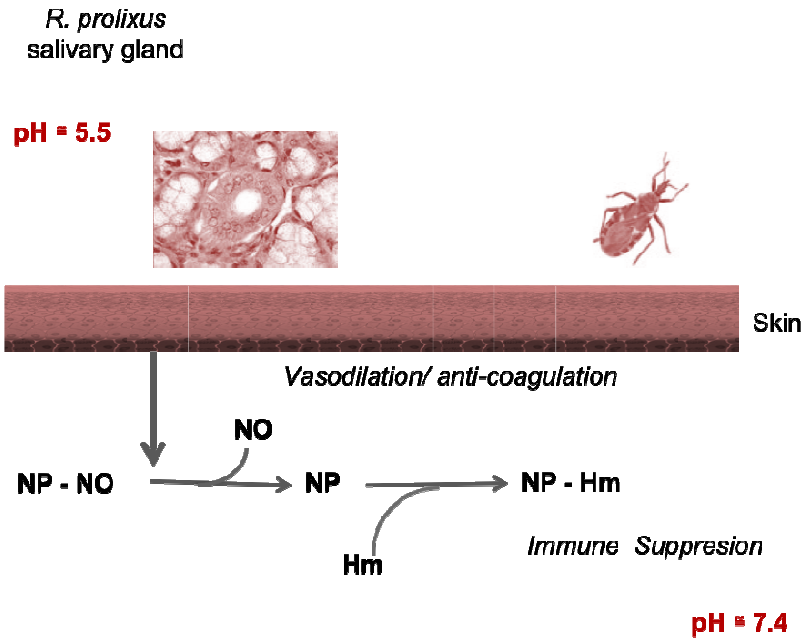

Figure 9. Scheme of NPs infection mechanism: In the salivary gland, NO is synthesized in the epithelium, secreted into the salivary gland lumen, and coordinated with iron on the distal side of the heme. After the bug bit, NO is released in the bloodstream and the ligand is replaced by histamine.

Rhodnius proxilus produces NO in the salivary gland and delivery it to the circulation where it induces a vasodilatory response (54). The stability of NO in solution is low, it therefore must be protected from oxidation by protein binding. Protection is provided by NPs, which transport a single molecule of NO per molecule of protein from the gland to the host while protecting it from oxidation (55,56). Once, in

the host tissue or circulation, the NO is released where it can act as a vasodilator and platelet aggregation inhibitor. Besides NO, remarkably high affinities of NP1-4 for histamine (Hm) were reported. Thus, Hm, which is released from mast cells at the site of the bite as an immune stimulus (57), may be trapped by NPs upon the release of NO, and, therefore, contribute to the immune response suppression (58) during the time of feeding (10–30 min) (59, 60) (Fig. 10).

NPs have a lipocalin fold consisting of an eight-stranded antiparallel beta-barrel containing a central hydrophobic ligand-binding cavity and two dissulfite bonds (61). The loops connecting the strands of the beta-barrel and forming the entrance of the ligand binding cavity are flexible and can tolerate a relatively free substitution of amino acid side chains without alteration of the basic protein fold.

The heme ligand is contained within the central cavity of the NPs and is bonded to the protein via coordination with the imidazole portion of His on the proximal side of the heme, the union of small ligands is a common mechanism of salivary lipocalin action. In the absence of NO and histamine, NPs contain a 5-coordinated ferric heme bound by a proximal histidine (62,63) (Fig 9).

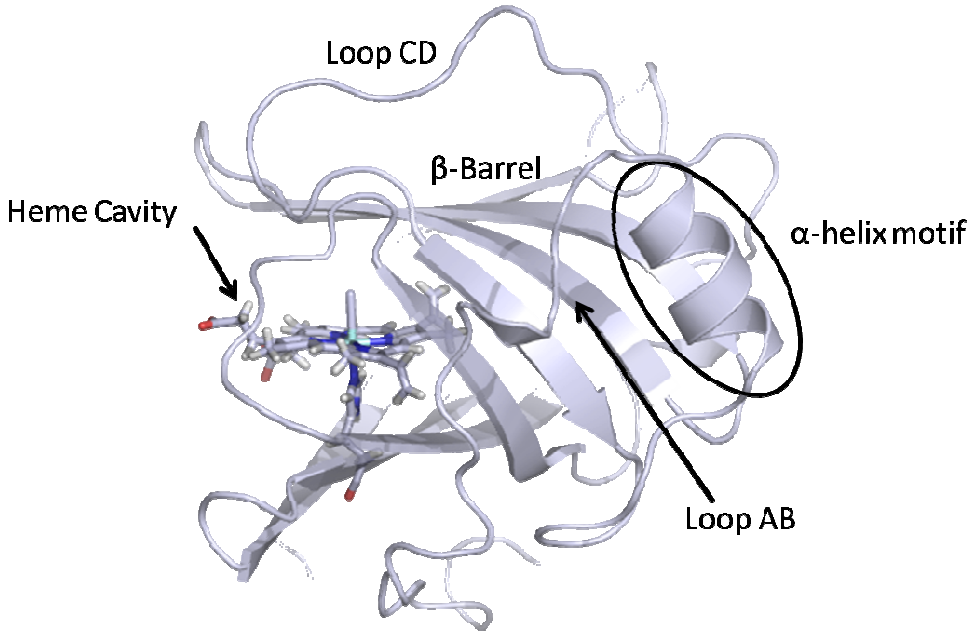

Figure 10. Representation of NPs lipocalin folding.

In 1997, Yuda and coworkers reported that the NO complex of NPs is more stable at pH 5-6 than at pH 7.4 (64). This difference is thought to be physiologically relevant in enhancing the delivery of NO in the hits. The pH of the saliva is reported

near 6.0, providing a relatively stable complex in the salivary gland. Later, in 2000, Andersen et al. reported that the injection into the host raised the pH surrounding the NP to 7.4, resulting in an increase in the release rate of NO of approximately 5-10 fold (65).

Table 1: NO release is a biphasic ($k_{off,1}$ and $k_{off,2}$) and pH sensitive mechanism, according to the equilibrium equation NP +NO → NP-NO → NP'-NO.

	pH 5		pH 8	
Nitrophorin	$k_{off,1}$	$k_{off,2}$	$k_{off,1}$	$k_{off,2}$
NP1	2 s^{-1}	0.6 s^{-1}	0.2 s^{-1}	0.02 s^{-1}
NP2	0.1 s^{-1}	0.01 s^{-1}	0.05 s^{-1}	0.005 s^{-1}
NP3	0.1 s^{-1}	0.01 s^{-1}	0.05 s^{-1}	0.005 s^{-1}
NP4	0.1 s^{-1}	0.01 s^{-1}	0.2 s^{-1}	0.02 s^{-1}

Among all the nitrophorin family members, NP4 is the most studied. The crystal structure of NP4-NO complex at low pH has revealed the occurrence of a substantial change in the protein conformation. In the absence of NO, the distal heme pocket is open with the A-B loop (31-37 residues) poorly ordered and the G-H loop (residues 125-133) located away from the heme. When NP4 binds NO, the AB and GH loops collapse into the distal pocket (66,67,68).

The fact that NO binding is tighter at low pH and induces a closed conformation with a buried carboxylate suggests that the loop dynamics may be related to the pH dependence (69,70). These evidences were corroborated by several structural mutations of residues D30N and D30A, which alter the AB loop, D129A L130A, which alter the GH loop and T121V that alters the hydrophobicity of the distal pocket (71). Kinetic and structural results suggested that the pH dependency for NO release is due to changes in loop dynamics. The *wt* NP4-NO structures at 5.6 and 7.5 are consistent with the mutagenesis results, at higher pH the hydrogen bond network stabilizing the closed conformation being largely disrupted.

4.2) The case of Nitrophorin 7

The most recently identified NP, termed NP7, appeared from a cDNA library generated from salivary glands of R. *proxilus* V^{th} instar nymphs (72).

The amino acid sequence identity between NP7 and the other *R. prolixus*

nitrophorins amount to 41% (NP1), 60% (NP2), 61% (NP3), and 42% (NP4), respectively. In Fig. 11 the amino acid sequence alignment between NP2 and NP7 is presented, which shows how accurately the sequences align; thus, a very similar protein fold is expected. Although NP1-4 have been extensively studied and are structurally well-characterized, it remains still a matter of debate why *R. prolixus* uses a whole bundle of NPs rather than just one, as seems to be the case with *Cimex lectularius* (the bedbug) (73). In addition, the six life stages of *R. prolixus* (five instar nymphs and the adult stage) use different expression patterns of NP1-NP6 (74), but it is not clear why. The detailed understanding of the similarities and differences of the isoforms on the molecular level is a prerequisite to answering these questions. Therefore, Knipp *et al.* initiated the careful characterization of the specific chemical and physical properties of NP7 (75).

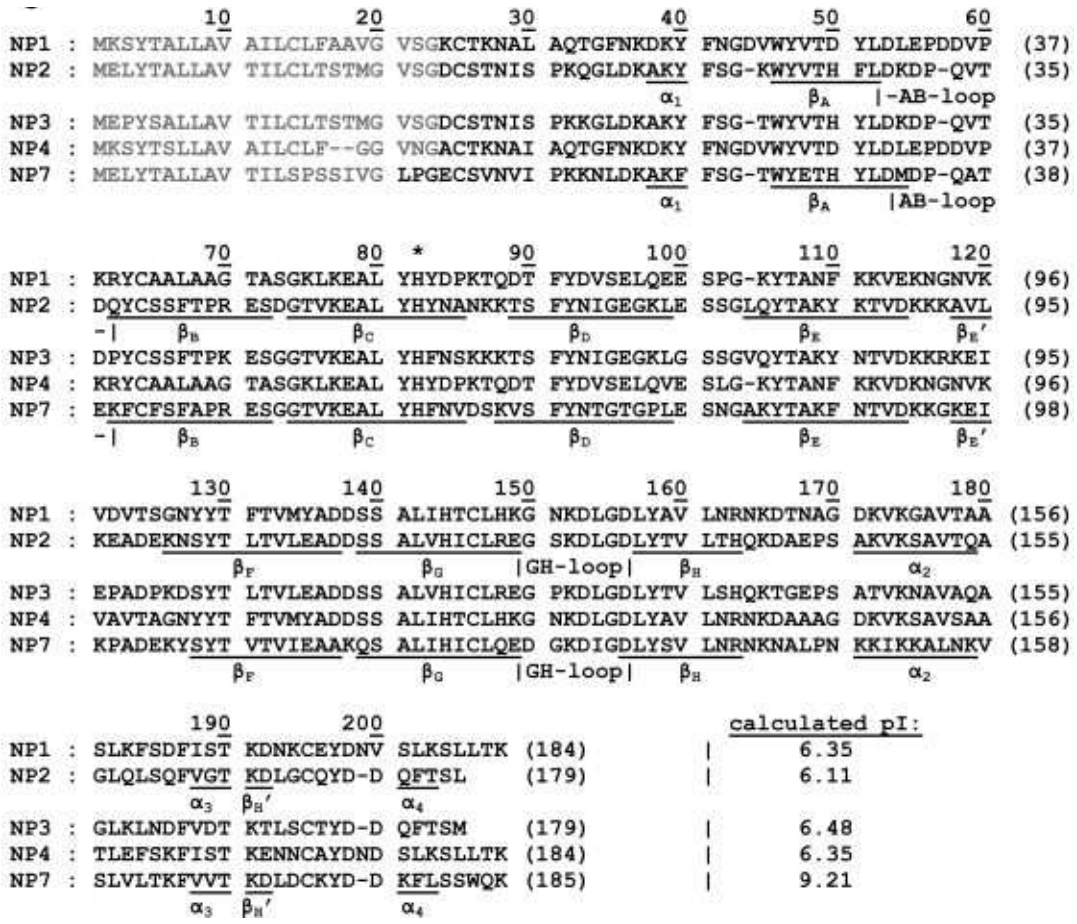

Figure 11. Amino acid sequences alignment of *R. prolixus* NP1 (Swiss-Prot entry Q26239), NP2 (Swiss-Prot entry Q26241), NP3 (Swiss-Prot entry Q94733), NP4 (Swiss-Prot entry Q94734), and NP7 (Swiss-Prot entry Q6PQK2). Signal sequences for secretion are displayed in gray. The proximal His is indicated with an asterisk.

Because the mature amino acid sequence of secreted proteins such as NPs can not be predicted with certainty based on computational methods, two N-terminals forms, wt NP7 and NP7Δ(1-3), were characterized by numerous biophysical techniques (76). The results strongly suggest that NP7 has an extended N-terminus to be functional in the biological context. However, the amino acid composition of NP7 exhibits interesting differences compared to NP1-4, the most exciting is the heme pocket residue Glu27. Remarkably, this residue is responsible for the orientation of the heme cofactor inside the pocket, that is, the cofactor can be rotated around the $C^{meso-\alpha} - C^{meso-\gamma}$ axis by the presence of this residue in NP7 and NP2, which was discovered using the variants NP7(E27V) and NP2(V24E) (77,78).

Of all the R. *prolixu*s NPs discovered, NP7 is especially interesting since it was found to bind to l-α-phosphatidyl-l-serine (PS)-bearing phospholipid membranes, which NP1-4 can not do (79,80,81). In platelets and mast cells, the loss of membrane asymmetry, which leads to the display of PS on the outer surface, is rapid and tightly coupled to other activation events (82). NP7 would thus be attracted to the negatively-charged surface of the activated platelets, while NP1-4 would remain in solution, diffusing away from the feeding site while releasing NO over a larger area. Besides its action as an NO delivery system, NP2 can also inhibit the intrinsic factor Xase complex, through binding with factor IX and IXa. NP7, however, was shown to inhibit prothrombinase activity through interaction with the prothrombinase activating PS (83). The binding to PS is accomplished through charge ↔ charge interactions with the positively charged NP7 surface on the protein surface opposite to the heme-binding site.

Once bound on an activated platelet, NP7 can release NO to inhibit platelet aggregation and act as an anticoagulant by blocking coagulation-factor binding sites. NO is highly reactive ($t_{½}$ < 1s in a biological environment), but is protected from oxidation when bound to the heme iron of the NPs (84). The targeted delivery to activated surfaces at the point of feeding may enhance the activity of NP7 as a platelet aggregation inhibitor by delivering NO in a protected form to its site of action and preventing its removal from the feeding area by diffusion and blood flow. The ability of the recombinantly prepared NP7 to bind to PS containing membrane surfaces was tested using large unilamellar vesicles composed of PC:PS (3:1). In contrast, none of the isoforms NP1-4 interacted with any of the phospholipids tested (85).

A comparison of the chemical structures of the eight phospholipids leads to the conclusion that a NP7·phospholipid complex is generally formed when the phospholipids carries a net negative charge, regardless of the headgroup attached as a second ester to the phosphate groups. The strong diversity of functionalities esterified to the phosphate group suggests that the negative charge on the latter is the major point of interaction between NP7 and the membrane surface (86).

Recognition of PS exposure by proteins is important in biological processes such as the assembly of coagulation complexes (87) and the triggering of apoptosis through Cytochrome c. Thus, NP7 recognizes PS bearing membrane surfaces as an indicator of activation and uses this as a means of targeting the surfaces of activated platelets. Activated platelets undergo changes in the plasma membrane that promote assembly of coagulation complexes at the wound site and allow the formation of a fibrin clot.

The NPs also bind histamine that is released from mast cells around the bite, the high specificity for Hm is a combination of the coordination with the ferriheme center plus the formation of a salt bridge of the Hm:NH_3^+ with Asp32:COO^- (67).

5. Molecular Dynamics Simulations

The protein structure obtained by X-ray diffraction provides information about protein internal tunnels and possible interactions between ligand and its receptor. However, is difficult to predict the dynamical motions about the interactions that stabilize such internal channels because the crystal geometry corresponds to a conformation representative of an average space and time. To study the conformational changes induced by the ligand union to its receptor or the ligand diffusion across the protein matrix, is necessary to have a methodology to follow the temporary evolution of the system.

In the last years, another technique to understand the tridimensional structure of macromecules has been improved: Nuclear Magnetic Resonance (NMR). The NMR spectroscopy is a powerful technique that can provide detailed information on the topology, dynamics and three-dimensional structure of molecules in solution and in solid state. The advantage of this methodology, with respect to X-ray crystallography, is the capture of dynamic movements in a larger scale (from microsecond to millisecond), such methodology can be applied for example to folding studies, although the technique is still limited to small systems.

The Molecular Dynamics (MD) simulations is theoretical computational technique, complementary to the experimental ones, that allows to study a system in an atomistic level and the temporary evolution of the macromecular systems such as proteins, the kinetic mechanisms and the thermodynamic processes associated with (88).

MD simulations were used by the first time in the 50's. In 1957, Alder and Wainright used this technique to simulate the evolution of a system composed by rigid spheres that interact by perfect collisions (89). In the next decades with the increased computer power, MD simulations passed to be an essential tool in molecular modeling. Nowadays, mostly applied on chemical physics and materials science fields, and on the modeling of biomolecules. In biophysics and structural biology, the method is frequently applied for ligand docking, simulations of lipid bilayers, homology modeling and even *ab initio* prediction of protein structure by simulating folding of the polypeptide chain from random coil.

This methodology gives detailed information about the movement of each particle and possible interactions between them. The analyzes of the dynamic motions of the protein can provide detailed information about conformational changes: both in the ligand and in the protein; possible pathways to ligand diffusion, involving the identification of new channels not present in the crystallographic structure; and more recently, is possible to predict protein folding.

To apply such methodology is necessary to have the 3D information of the molecular structure as the cartesian coordinates of each atom. The atoms and molecules are allowed to interact for a period of time, giving a view of the motion of the atoms. In the most common version, the trajectories of atoms and molecules are determined by numerically solving the Newton's equations of motion for a system of interacting particles, where forces between the particles and potential energy are defined by molecular mechanics force fields.

Limitations of the method are related mostly to the accuracy of the molecular mechanical force fields and to the simplified expressions used to represent both intramolecular and intermolecular interactions.

Bibliographic References

1. Voet D., Voet J. G., Biochemistry, 4th Edition ISBN 978-0-470-57095-1, (**2011)**
2. Takeda K., Sato J., Goto K., Fujita T., Watanabe T., Abo M., Yoshimura E., Nakagawa J., Abe A., Kawasaki S., Niimura Y., *Biometals*, (**2010)** 23, 727-737
3. Kundu S., Trent J. T., Hargrove M. S., *Trends Plant Sci*., (**2003**) 8, 387-393
4. Simonneaux G., Bondon A., *Chem. Rev.*, (**2005**) 105, 2627-2646
5. Shaik S., Kumar D., Visser S.P., Altun A., Thiel W., *Chem. Rev.*, (**2005**) 105, 2279-2328
6. Jai R., Chan M. K., *J. Biol. Inorganic Chem.*, (**2003**) 8, 1-11
7. Marletta M. A., *J. Biol. Chem.*, (**1993**) 268, 12231–12234
8. Montfort W. R., Weischsel A., Andersen J. F., *Biochim. Biophys Acta*, (**2000**) 1482, 110-118
9. Lucas K.A., Pitari G.M., Kazerounian S., Ruiz-Stewart I., Park J., Schulz S., Chepenik K.P., Waldman S.A., *Pharmacol Rev.,* (**2000**) 52, 375-414
10. Fenton, M. J., Vermeulen, M. W., *Infect. Immun.*, (**1996**) 64, 683-690
11. Fenton, M. J., *Curr. Opin. Hematol.*, (**1998**) 5, 72-78
12. MacMicking, J. D., North, R. J., LaCourse, R., Mudgett, J. S., Shah, S. K., Nathan, C. F., *Proc. Natl. Acad. Sci. U. S. A.*, (**1997**) 94, 5243-5248
13. Ghosh, A., The smallets biomolecules: diatomics and their interactions with heme proteins, Elsevier, **2007**
14. Scott E.E., Gibson Q.H., Olson J.S., *J. Biol. Chem.*, (**2001**) 276, 577-600
15. Boechi L., Martí M.A., Crespo A., Milani M., Orozco M., Bolognesi M., Luque F.J., Estrin D.A., *Proteins*, (**2008**) 73, 372-379
16. Boechi L., Manex P.A., Luque F.J., Martí M.A., Estrin D.A., *Proteins,* (**2009**) 78, 372-379
17. Nadra A. D., Martí M. A., Pesce A., Bolognesi M., Estrin D. A., *Proteins,* (**2007**) 71, 695-705
18. Goldbeck R. A., Pillsbury M. L., Jensen R. A., Mendoza J. L., Nguyen R. L., Olson J. S., Soman J., Kliger D. S., Esquerra R. M., *J. Am. Chem. Soc.*, (**2009**) 131 (34), 12265-12272
19. Goldbeck R. A., Bhaskara S., Ortega C., Mendoza J. L., Olson J. S., Soman J., Kliger D. S., Esquerra R. M., *Proc. Natl. Acad. Sci. USA,* (**2006**) 103, 1254-1259

20. Ouellet Y. H., Daigle R., Laguee P., Dantsker D., Milani M., Bolognesi M., Friedman J. M., Guertin M., *J. Biol. Chem.*, (**2008**) 283, 27270-27278

21. Bikiel D.E., Forti F., Boechi L., Nardini M., Luque F. J., Martí M.A, Estrin D.A., *J. Phys. Chem. B*, (**2010**) 114, 8536–8543

22. Scott E.E., Gibson Q.H., Olson J.S., *J. Biol. Chem.*,(**2011**) 276, 5177-5188

23. Laverman L. E., Ford P. C., *J. Am. Chem. Soc.*, (**2001**) 123, 11614-11622

24. Bikiel D. E., Boechi L., Capece L., Crespo A., De Biase P. M., Di Lella S., González Lebrero M. C., Martí M. A., Nadra A. D., Perissinotti L. L., Scherlis D. A., Estrin, D. A., *Phys. Chem. Chem. Phys.*, (**2006**) 8, 5611-5628

25. Martí M. A., Crespo A., Capece L., Boechi L., Bikiel D. E., Scherlis D. A., Estrin D. A., *J. Inorg. Biochem.*, (**2006**) 100, 761-770

26. Kendrew J.C., Bodo G., Dintzis H. M., Parish R.G., Wyckoff H., Phillips D.C., *Nature*, (**1958**) 181, 662-666

27. Smith L.J., Kahraman A., Thornton J.M., *Proteins*, (**2010**) 78, 2349-2368

28. Ghosh A., The smallets biomolecules: diatomics and their interactions with heme proteins, Elsevier (**2007**)

29. Vinogradov S.N., Moens L., *J. Biol. Chem.*, (**2008**) 283, 8773-8777

30. Frauenfelder H., McHahon B.H., Fenimore P. W., *Proc. Natl. Acad. Sci. U. S. A.*, (**2003**) 100, 8615-8617

31. Wittenberg J.B., Wittenberg B.A., J. Exp. Biol., (**2003**) 206, 2011-2020

32. Kapp O. H., Moens L., Vanfleteren J., Trotman C.N., Suzuki T., Vinogradov S.N., *Prot. Sci.*, (**1995**) 4, 2179-2190

33. Vinogradov S. N., Hoogewijs D., Bailly X., Mizuguchi K., Dewilde S., Moens, L., Vanfleteren J. R. , *Gene*, (**2007**) 398, 132-142

34. Pesce A., Couture M., Dewilde S., Guertin M., Tamauchi K., Ascenzi P., Moens L. and Bolognesi M., *EMBO J.*, (**2000**) 19, 2424-2434

35. Wittenberg J.B., Bolognesi M., Wittenberg B.A., Guertin M., *J. Biol. Chem.*, (**2002**) 277, 871-874

36. Eich R.F., Lemon T., Doherty D.H., Curry S.R., Aitken J.F.,Mathews A.J., John son K.A., Smith R.D., Phillips G.N., Jr. Olson J.S., *Biochemistry*, (**1996**) 35, 6976–6983

37. Styblo K., *Adv. Tuberc. Res.*, (**1980**) 20, 1–63

38. Cunningham A.F., Spreadbury C.L., *J. Bacteriol.*, (**1998**) 180, 801-808

39. MacMicking J.D., North R.J, LaCourse R.R., Mudgett J.S., Shah S.K., Nathan C.F., *Proc. Natl. Acad. Sci. U. S. A.*, (**1997**) 94, 5243-5248

40. Couture M., Yeh S.-R., Wittenberg B. A., Wittenberg J. B., Ouellet Y., Rousseau D. L., Guertin M., *Proc. Natl. Acad. Sci. U. S. A.*, (**1999**) 96, 11223-11228

41. Milani M., Pesce A., Ouellet Y., Ascenzi P., Guertin M., Bolognesi M., *EMBO J.*, (**2001**) 20, 3902-3909

42. Bidon-Chanal A., Marti M.A., Crespo A., Milani, Orozco M., Bolognesi M., Luque, F.J., Estrin, D.A., *Proteins*, (**2006**) 64, 457-464

43. Bidon-Chanal A., Marti M.A., Estrin D.A., Luque F.J., *J. Am. Chem. Soc.*, (**2007**) 129, 6782-6788

44. Ouellet Y.H., Daigle R., Lague P., Dantsker D., Milani M., Bolognesi M., Friedman J.M., Guertin M.J., *J. Biol. Chem*., **(2008**) 283, 27270-27278

45. Gardner P.R., Gardner A.M., Martin L.A., Salzman A.L., *Proc. Natl. Acad. Sci. U. S. A.*, (**1998**) 95, 10378–10383

46. Martí M.A., Bidon-Chanal A., Crespo A., Yeh SR, Guallar V., Luque F.J.., Estrin D.A., *J. Am. Chem. Soc*., (**2008**) 130, 1688-1693

47. Flower D.R., *Biochem. J.*, (**1996**), 3181–3214

48. Francischetti I.M., Sa-Nunes A., Mans B.J., Santos I.M., Ribeiro J.M., The role of saliva in tick feeding. *Front Biosci*. (**2009**) 14, 2051-2088

49. Kirchhoff L.V., N. *Engl. J. Med*., (**1993**) 329, 639–644

50. Andersen J.F., Francischetti I.M., Valenzuela J.G., Schuck P., Ribeiro J.M.., *J. Biol. Chem.*, (**2003**) 14, 4611-4617

51. Calvo E., Mans B.J., Ribeiro J.M., Andersen J.F., *Proc. Natl. Acad. Sci. U. S. A.*, (**2009**) 106, 728-3733

52. Fontaine A., Diouf I., Bakkali N., Missé D., Pagès F., Fusai T., Rogier C., Almeras L., *Parasites & Vectors*, (**2011**) 187, 1-17

53. Denninger J.W., Marletta M.A., *Biochim. Biophys. Acta*, (**1999**) 1411, 334−350

54. Ribeiro J.M.C., Hazzard J.M.H., Nussenzveig R.H., Champagne D.E., Walker F.A., *Science*, (**1993**) 260, 539−541

55. Ascenzi P., Nardini M., Bolognesi M., Montfort W. R., *Biochem. Mol. Biol. Ed.*, (**2002**) 30, 68–71

56. Montfort W.R., Weichsel A., Andersen J.F.., *Biochim Biophys Acta*, (**2000**)

1482, 110–118

57. Watt A. P., Ennis M., SpringMed Publishing Ltd., (**2004**)

58. Ribeiro J.M., Walker F.A., *J. Exp Med.,* (**1994**) 180, 2251-2257

59. Zeledón R., Rabinovich J.E., *Annual Rev Entomol.*, (1981) 26, 101-133

60. Lehane M. J., Cambridge University Press, (**2005**)

61. Knipp M., Taing J.J., He C., *J. Inorg. Biochem.*, (**2011**) 105, 1405-1412

62. Weichsel A., Andersen J.F., Champagne D.E., Walker F.A., Montfort W.R.., *Nat. Struct. Biol.*, (**1998**) 5, 304-309

63. Walker F.A., *J. Inorg Biochem.*, (**2005**) 99(1), 216-236

64. Yuda M., Hirai M., Miura K., Matsumura H., Ando K., Chinzei Y., *Eur. J. Biochem.*, (**1996)** 242, 807–812

65. Andersen J.F., Ding X.D., Balfour C., Shokhireva T.Kh., Champagne D.E., Walker F.A., Montfort W.R., *Biochemistry*, (**2000**) 39, 10118–10131

66. Martí M.A., González Lebrero M.C., Roitberg A.E., Estrin D.A., *J. Am. Chem. Soc.*, (**2008**), 8708-8719

67. Di Russo N.V., Estrin D.A., Martí M.A., Roitberg A.E., *Plos Comput. Biol.*, (**2012**) 8, 1-9

68. Kondrashov D.A., Roberts S.A., Weichsel A., Montfort W.R., *Biochemistry*, (**2004**) 43, 13637–13647

69. Kukić P., Farrell D., Søndergaard C.R., Bjarnadottir U., Bradley J., *Proteins*, (**2010**) 78, 971–984

70. Chakrabarty S., Namslauer I., Brzezinski P., Warshel A., *Biochim. Biophys. Acta* (**2011**) 1807, 413–426

71. Maes E.M., Weichsel A., Andersen J.F., Shepley D., Montfort W.R., *Biochemistry*, (**2004**) 43, 6679–6690

72. Ribeiro J.M., Andersen J., Silva-Neto M.A., Pham V.M., Garfield M.K., Valenzuela JG., *Insect. Biochem. Mol. Biol*., (**2004**) 34, 61-79

73. Weichsel A., Maes E. M., Andersen J. F., *Proc. Natl. Acad. Sci. USA*, (**2005**) 102, 594–599

74. Moreira M.F., Coelho H.S.L., Zingali R.B., Oliveira P.L., Masuda H., *Insect. Biochem. Mol. Biol.*, (**2003**) 33, 23–28

75. Knipp M., Zhang H., Berry R.E., Walker F.A., *Protein Expr Purif.*, (**2007**) 54, 183-91

76. Abbruzzetti S., He C., Ogata H., Bruno S., Viappiani C., Knipp M., *J. Am. Chem. Soc.*, (**2012**) 134, 9986–9998

77. Yang F., Zhan H., Knipp M., *Biochemistry*, (**2009**) 48, 235-241

78. He C., Neya S., Knipp M., *Biochemistry*, (**2011**) 50(40), 8559-75

79. Ding X.D., Weichsel A., Andersen J.F., Shokhireva T.K., Balfour C., Pierik A.J., Averill B.A., Montfort W.R., Walker F.A., *J. Am. Chem. Soc.*, (**1999**) 121, 128–138

80. Andersen J.F., Gudderra N.P., Francischetti I.M.B., Valenzuela J.G., Ribeiro J.M.C., *Biochemistry*, (**2004**) 43, 6987–6994

81. Hoshino M., Maeda M., Konishi R., Seki H., Ford P.C., *J. Am. Chem. Soc.*, (**1996**) 18, 5702–5707

82. Knipp M., Yang F., Berry R.E., Zhang H., Shokhirev M.N., Walker F.A., *Biochemistry*, (**2007**), 13254-13268

83. Yamaji-Hasegawa A., Tsujimoto M., *Biol. Pharmac. Bull.*, (**2006**) 29, 1547–1553

84. Ding X.D., Weichsel A., Andersen J.F., Shokhireva T.K., Balfour C., Pierik A.J., Averill B.A., Montfort W.R., Walker F.A., *J. Am. Chem. Soc.*, (**1999**) 121, 128–138

85. Martin S., Pombo I., Poncet P., David B., Arock M., Blank U., *Arch. Allergy Immunol.*, (**2000**) 123, 249–258

86. Daleke D.L., *J. Lipid Res.*, (**2003**) 44, 233–242

87. Andersen J.F., Montfort W.R., *Biochemistry* (**2000**) 275, 30496–30503

88. Adcock S.A., McCammon J.A., *Chem Rev.*, (**2006**) 106, 1589-1615

89. Alder B.J., Wainwright T.E., *J. Chem Phys.*, (**1957**) 27, 1208-1209

Chapter II: Objectives

The diversity of functional roles played by heme proteins in all kingdoms of life is to a large extent regulated by the thermodynamic and kinetic proprieties of their interaction with small molecules. In particular, ligand binding and unbinding of gaseous molecules are influenced by factors such as coordination to the heme, the nature of the residues in the distal cavity, and the migration through the protein matrix to reach the heme active site.

The presence of transient cavities or tunnels is intimately linked to the migration of ligands, and understanding their structural and dynamic properties is therefore crucial to gain insight into the functional role. Molecular Dynamics (MD) is a powerful tool to characterize the structural plasticity of internal cavities/tunnels, to determine the energetic details of ligand migration and to identify the factors that influence this process. The impact of MD is illustrated here by examinating the migration and binding of ligands in two biologically relevant hemeproteins: the truncated hemoglobin N from *M. tuberculosis*, and Nitrophorin 7 from *R. prolixus*.

With respect to trHbN, the main goals are:

a) Validate the importance of PheE15 residue in the previous proposed dual path mechanism. Thus, the impact of three residue mutations on the ligand migration mechanism has been examined:
    - PheE15Ala (smaller residue)
    - PheE15Ile (conserving initial residue size but losing the aromatic ring)
    - PheE15Tyr (conserving the aromaticity)

b) Understand the dynamical behavior of the trHbN and a putative reductase: Flavodoxin reductase from E. Coli.

Regarding Nitrophorin 7, the major aim of this work is twofold. First, to identify the molecular migration of the diatomic molecule NO across the protein matrix in two proposed –open and closed– conformations. Second, to understand the importance of the three extra residues in N-terminal sequence (Gly-Pro-Leu) by comparing the wtNP7 protein with the mutant protein Δ(1-3) NP7.

Chapter III: Publications

3.1 Journal Publications

3.1.1 Role of PheE15 Gate in Ligand Entry and Nitric Oxide Detoxification Function of Mycobacterium tuberculosis Truncated Hemoglobin N

The Truncated Hemoglobin N from *Mycobacterium tuberculosis* is likely involved in the detoxification of nitric oxide released by macrophages in the early stages of infection, as this protein is involved in the conversion of NO to nitrate anion. It has been suggested that the access of the ligands (O_2, NO) to the heme cavity takes places through a dual step mechanism. First, O_2 migrates through a short tunnel defined by helices G and H leading to the heme cavity. Second, binding of O_2 to the iron facilitates the migration of NO via the long branch of the tunnel, which is delineated by helices B and E.

The mechanism of NO entrance is regulated by PheE15, which can adopt two different conformations, open and closed, that enable or impede migration through the long branch, respectively. In order to check the gating role presumably played by PheE15, we performed several mutations of this residue, PheE15Ala, PheE15Ile and PheE15Tyr, and compared the structural and dynamical features of the mutated proteins with the wild type protein through molecular simulations.

The structural and dynamical properties of the mutants have been examined by means of extended Molecular Dynamics (MD) simulations, paying particular attention to the maintenance of the tunnel and the migration of ligands through the protein matrix. The results suggest that the protein fold and the hydrogen bond network in the distal pocket are preserved, but the mobility of the gate residue is largely affected by the mutation. Molecular simulations substantiated that mutation at the PheE15 gate confers significant changes in the long tunnel, and therefore may affect the migration of ligands.

The analysis of the tunnel topology was performed with MdPocket, which revealed that for the mutants PheE15Ile and PheE15Tyr there is a disruption around the region that surrounds the mutated residue, suggesting that ligand migration through the tunnel long branch is impeded by the steric hindrance imposed by the side chains of the mutated residues. In contrast, the mutant PheE15Ala displays a significant occlusion at the entrance of the long branch channel.

Due to the new evidences, we performed multiple MD simulations with free NO to check the ability of the ligand molecule to diffuse in the mutant protein matrix. The results suggest that PheE15Ile and PheE15Tyr display two major entrance pathways, between helices E and B and between E and G helices. Both pathways were previously described by A. Bidon-Chanal *et al.* and Guertin *et al*. Probably due to the disruption at the entrance of the long tunnel, PheE15Ala displays three alternative pathways, the two

previously described and a new one in which NO access the heme cavity by the short branch of the tunnel, the same pathway described for the O_2 access.

Multiple steered MD have been used to determine the energetic cost of a NO molecule travelling from the entrance of the long branch tunnel until the heme cavity. For the mutants PheE15Ile and PheE15Tyr the free energy profile reveals an intermediate state between the profiles found for the open and closed conformations of the wild type protein. These results are assigned to the difficulties displayed by the diatomic ligand molecule to jump over the gate residue.

The MD results could thus provide a molecular basis to explain the decrease in NO consumption activity measured experimentally for the mutants. PheE15Ala only displays 51% of the NOD activity detected for the wild type protein, and the enzymatic activity measurements for the mutations PheE15Ile and PheE15Tyr reveals even a larger decrease.

Overall, these findings point out the delicate structural balance imposed by the PheE15 gate, which not only regulates ligand migration, but also contributes to avoid the collapse of helices B and E, thus preserving the ligand accessibility along the tunnel long branch. The results presented herein demonstrate the pivotal role of PheE15 in modulating the NOD function of Mtb HbN.

OPEN ACCESS Freely available online

PLOS ONE

Role of PheE15 Gate in Ligand Entry and Nitric Oxide Detoxification Function of *Mycobacterium tuberculosis* Truncated Hemoglobin N

Ana Oliveira[1☯], Sandeep Singh[2☯], Axel Bidon-Chanal[1], Flavio Forti[1], Marcelo A. Martí[3], Leonardo Boechi[3], Dario A. Estrin[3], Kanak L. Dikshit[2]*, F. Javier Luque[1]*

1 Department of Physical Chemistry and Institute of Biomedicine (IBUB), Faculty of Pharmacy, University of Barcelona - Recinte Torribera, Santa Coloma de Gramenet, Spain, **2** CSIR-Institute of Microbial Technology, Chandigarh, India, **3** Departamento de Química Inorgánica, Analítica y Química Física/Instituto de Química Física de los Materiales, Medio Ambiente y Energía (INQUIMAE), Facultad de Ciencias Exactas y Naturales, Universidad de Buenos Aires, Buenos Aires, Argentina

Abstract

The truncated hemoglobin N, HbN, of *Mycobacterium tuberculosis* is endowed with a potent nitric oxide dioxygenase (NOD) activity that allows it to relieve nitrosative stress and enhance *in vivo* survival of its host. Despite its small size, the protein matrix of HbN hosts a two-branched tunnel, consisting of orthogonal short and long channels, that connects the heme active site to the protein surface. A novel dual-path mechanism has been suggested to drive migration of O_2 and NO to the distal heme cavity. While oxygen migrates mainly by the short path, a ligand-induced conformational change regulates opening of the long tunnel branch for NO, via a phenylalanine (PheE15) residue that acts as a gate. Site-directed mutagenesis and molecular simulations have been used to examine the gating role played by PheE15 in modulating the NOD function of HbN. Mutants carrying replacement of PheE15 with alanine, isoleucine, tyrosine and tryptophan have similar O_2/CO association kinetics, but display significant reduction in their NOD function. Molecular simulations substantiated that mutation at the PheE15 gate confers significant changes in the long tunnel, and therefore may affect the migration of ligands. These results support the pivotal role of PheE15 gate in modulating the diffusion of NO via the long tunnel branch in the oxygenated protein, and hence the NOD function of HbN.

Citation: Oliveira A, Singh S, Bidon-Chanal A, Forti F, Martí MA, et al. (2012) Role of PheE15 Gate in Ligand Entry and Nitric Oxide Detoxification Function of *Mycobacterium tuberculosis* Truncated Hemoglobin N. PLoS ONE 7(11): e49291. doi:10.1371/journal.pone.0049291

Editor: Paolo Carloni, German Research School for Simulation Science, Germany

Received August 5, 2012; **Accepted** October 8, 2012; **Published** November 8, 2012

Funding: The authors thank the Department of Biotechnology for providing research fellowship to SS, the Spanish Ministerio de Innovación y Ciencia (SAF2011-27642), Generalitat de Catalunya (2009SGR298), Xarxa de Recerca en Química Teòrica i Computacional (XRQTC), University of Buenos Aires (X074) and CONICET (PIP 2508) for financial support, and the Barcelona Supercomputation Center for computational resources. The funders had no role in study design, data collection and analysis, decision to publish, or preparation of the manuscript.

Competing Interests: The authors have declared that no competing interests exist.

* E-mail: kanak@imtech.res.in (KLD); fjluque@ub.edu (FJL)

☯ These authors contributed equally to this work.

Introduction

Mycobacterium tuberculosis (*Mtb*) poses a serious threat to the public health worldwide, infecting nearly one third of the global population. The remarkable adaptability of tubercle bacillus to cope with hazardous level of reactive nitrogen/oxygen species within the intracellular environment contributes to its pathogenicity. An enhanced level of nitric oxide (NO) and reactive nitrogen species produced within activated macrophages during infection act as a vital part of host defense, limit the intracellular survival of *Mtb*, and contributes in restricting the bacteria to latency. Nevertheless, *Mtb* has evolved efficient resistance mechanisms by which toxic effects of NO and nitrosative stress can be evaded. One of the unique defense mechanisms by which *Mtb* protects itself from the toxicity of NO relies on the oxygenated form of truncated hemoglobin N (HbN), which catalyzes the rapid oxidation of NO to harmless nitrate [1–3]. Compared to horse heart myoglobin, the nitric oxide dioxygenase (NOD) reaction catalyzed by *Mtb* HbN is ~15-fold faster, suggesting that it may be crucial in relieving nitrosative stress [4].

Despite having single domain architecture, the NO-scavenging ability of *Mtb* HbN is comparable to flavoHbs that are integrated with a reductase domain and known to have a high NOD activity. It is thus important to understand what structural and dynamical features contribute to the efficiency of its enhanced NO-scavenging function, and therefore ensure survival of the bacillus under nitrosative stress. X-ray crystallographic studies revealed that *Mtb* HbN hosts a protein matrix tunnel composed by two orthogonal branches [5,6]. In addition, computational simulations performed by some of the authors suggested that *Mtb* HbN has evolved a novel dual-path mechanism to drive migration of O_2 and NO to the distal heme cavity [7,8]. According to such a mechanism (Fig. 1), access of O_2 to the heme cavity primarily involves migration through the tunnel short branch (~10 Å long, shaped by residues in helices G and H). Binding to the heme then regulates opening of the tunnel long branch (~20 Å long, mainly defined by helices B and E) through a ligand-induced conformational change of PheE15 residue, which would act as a gate. It has been recently shown that the opening of PheE15 in the oxygenated protein is also affected by the N-terminal Pre-A motif [9].

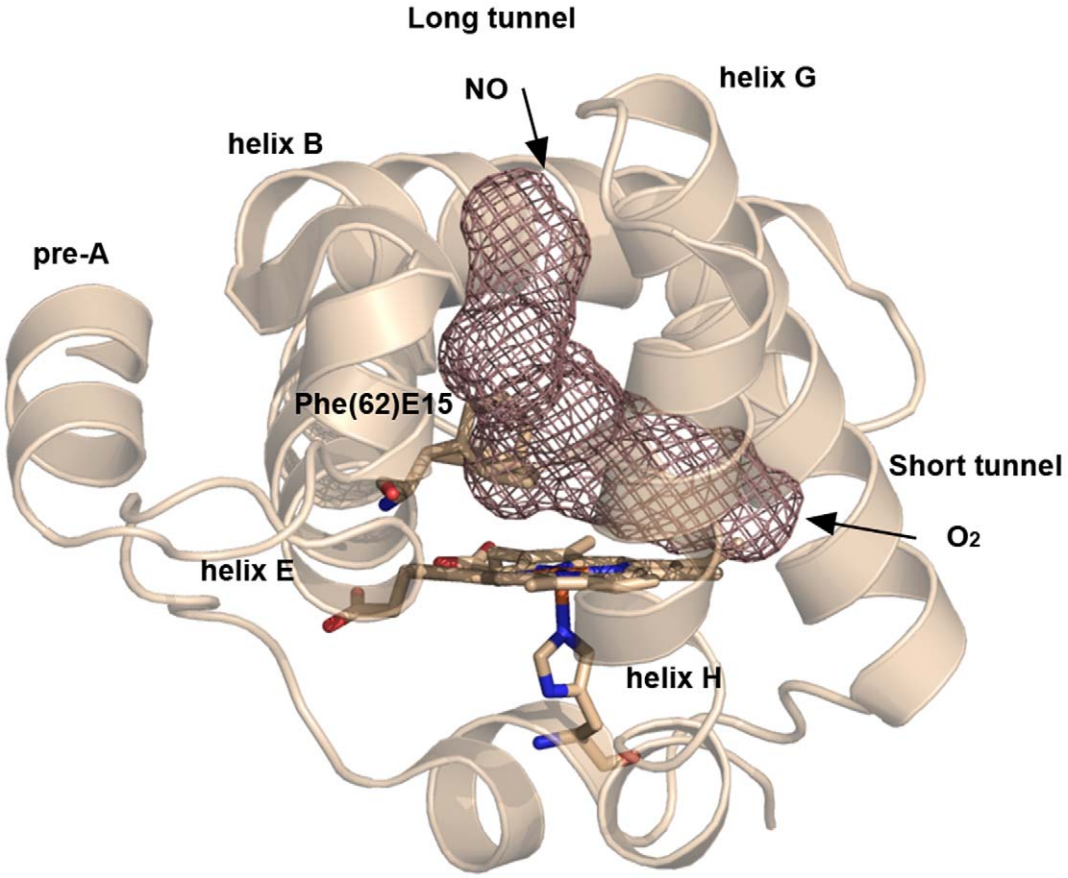

Figure 1. Representation of the long and short branches of the tunnel system. The graphical display is based on the X-ray crystallographic structure of *Mtb* HbN (PDB entry 1IDR), and the access routes of O_2 and NO in the dual-path ligand-modulated mechanism proposed for this protein are indicated. The gating residue PheE15 (residue 62) is shown in the two conformations found in the X-ray structure as sticks.
doi:10.1371/journal.pone.0049291.g001

Since the NOD function of HbN depends on the diffusion of NO to the O_2-bound heme through the long tunnel branch, the PheE15 gate emerges as a fundamental residue in determining the overall efficiency of the NO scavenging. Accordingly, the NOD function of HbN must result from a balanced tuning of the opening/closing events of the gate. Moreover, the functional implication of PheE15 in assisting the NOD activity is supported by the preservation of this residue in mycobacterial HbNs, while it is replaced by other residues in truncated hemoglobins O and P [10,11]. However, to the best of our knowledge, no experimental data have yet been reported to examine the gating role of PheE15 and its influence on the NOD activity conducted by *Mtb* HbN. In this context, this study has been undertaken to probe the role of PheE15 in protein function. To this end, several PheE15 gate mutants have been tested experimentally for their NOD function. In addition, molecular dynamics (MD) simulations have been performed to analyze the structural changes in the topology of long tunnel and the alterations in the protein dynamics, paying attention to the ligand migration properties through the tunnel. Our results confirm the critical role played by E15 in ligand migration along the long channel.

Materials and Methods

Strains, Plasmids and Culture Conditions

Escherichia coli strains, JM109 and BL21DE3 were used for the cloning and expression of recombinant genes. Bacterial cultures were grown in Luria-Bertani (LB) or Terrific Broth (containing 24 g of Yeast Extract, 12 g of Bacto-Tryptone, 12.54 g of K_2HPO_4, 2.31 g of KH_2PO_4) medium at 37°C at 180 r.p.m. When required, ampicillin and kanamycin (Sigma) were added at a concentration of 100 and 30 μg/ml, respectively. Plasmids, pBluescript (Stratagene) and pET28C (Novagen) were used for cloning and expression of recombinant genes as described earlier [3,12]. The oligonucleotides were custom synthesized by Integrated DNA Technologies Inc. NO (98.5%) was obtained from Sigma Aldrich and saturated NO was prepared as mentioned previously [13]. Heme content of the cell was measured as noted in previous studies [13].

Site-directed Mutagenesis and Construction of PheE15 Gate Mutants of HbN

Recombinant plasmid pPRN [3] was used as a source of HbN gene for the site directed mutagenesis. PheE15 mutants to Ala, Tyr, Ile or Trp were generated using a PCR approach. PCR amplified genes were cloned at NdeI-BamHI site of pET28c and expressed under T7 promoter as described previously [3]. Recombinant HbN and its mutant proteins were purified from the cell lysate of *E. coli* using metal affinity chromatography following standard procedures. Authenticity of mutants was confirmed after nucleotide sequencing.

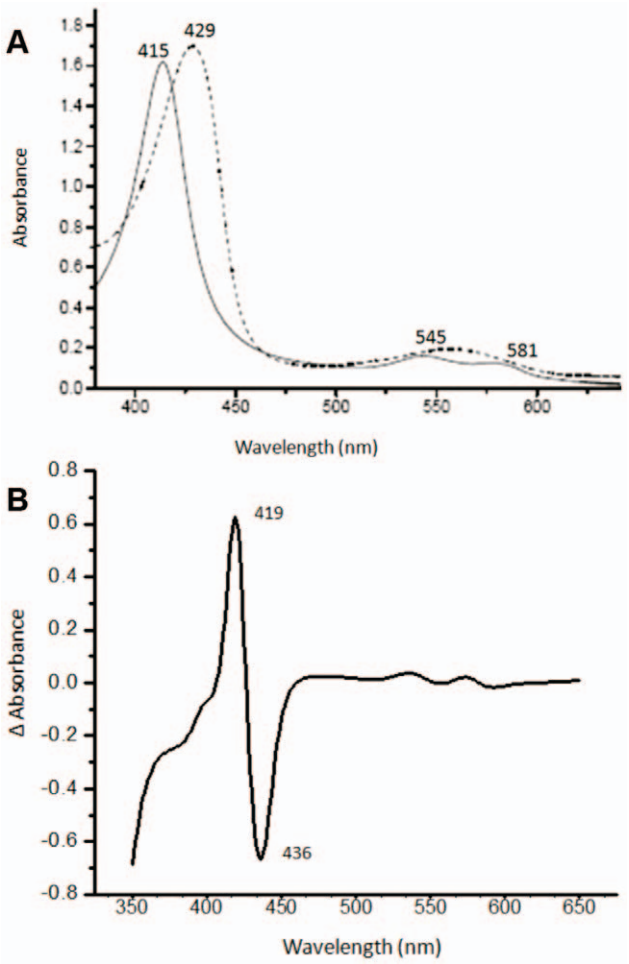

Figure 2. Spectral properties of PheE15Ala mutant of HbN. (A) Optical absorption spectra of oxygenated (solid line) and sodium dithionite reduced species of mutant HbN, recorded in 50 mM Tris.Cl (pH 7.5). (B) CO-difference spectrum of PheE15Ala mutant of HbN. Spectral profile of other PheE15 gate mutants (PheE15Tyr, PheE15Trp and PheE15Trp) appeared similar and matched with the wild type spectrum reported earlier [1].
doi:10.1371/journal.pone.0049291.g002

Measurements of Heme Content and NOD Activity

Total heme content was determined following the procedure described earlier [14]. Heme concentration was calculated from the absorption difference at 556 and 539 nm for the sodium dithionite-reduced and ferricyanide-oxidized sample. NOD activity of cells or purified protein was monitored polarographically as described previously [3,15]. NO consumption buffer assay contained 60 mM K_2HPO_4, 33 mM KH_2PO_4, 7.6 mM $(NH_4)_2SO_4$, 1.7 mM sodium citrate, 10 mM glucose and 200 μg/ml chloramphenicol. NO uptake rate of O_2-bound HbN and its mutants was measured from the slope of curving traces recorded in the presence of specified concentration of NO following established protocols [3,15].

Measurement of Ligand Binding

O_2 and CO binding was checked from the absorption spectra of O_2- and CO-bound species [9]. CO difference spectra were recorded between 350 to 600 nm after bubbling CO into the protein sample cuvette and recording the difference spectra against sodium-dithionite reduced protein. Oxygen equilibrium curves of HbN mutants were checked following the published procedure [16] to check their p^{50} value. The association rate for CO binding to HbN mutants was determined by flash photolysis. A concentrated stock solution of deoxyHbN was diluted anaerobically (~100 μM) into a cuvette (1 mm path length) containing CO (1 mM). The fully liganded sample of ferrous HbN was photodissociated by 0.3 μs excitation pulse from a dye laser. The bimolecular rebinding time courses were collected as described elsewhere [17]. A minimum of five traces were collected and averaged for each experiment.

Table 1. Oxygen binding and CO association kinetics of PheE15 gate mutants of HbN of *M. tuberculosis.*

Protein	$p^{50}(O_2)$[a]	k_{on} (CO)[b]
Wild type	0.019	2.5×10^7
PheE15Ala	0.021	3.0×10^7
PheE15Ile	0.016	2.3×10^7
PheE15Tyr	0.013	2.0×10^7
PheE15Trp	0.023	1.8×10^7

[a]In units of mm Hg.
[b]$M^{-1}s^{-1}$. Values derived from three independent measurements, each consisting of multiple shots (>50) and averaged out by the program to give the final value. The standard deviation is in the range 0.3–0.5 ($\times10^7$).
doi:10.1371/journal.pone.0049291.t001

NO-oxidation by an Oxygenated Adduct of HbN and its Mutants

Wild type and mutant proteins were fully oxygenated by exposing the deoxygenated protein samples to air and checking their absorption spectra, which gave a specific Soret peak at 415 and two peaks, α and β, at 570 and 540 nm, very similar to oxy form of hemoglobin. With a gas tight Hamilton syringe, NO (5 μM) was sequentially added to the oxygenated protein (40 μM), and absorption spectra were recorded after each addition to follow the conversion into the oxidized form. The NO-induced oxidation of mutants was compared with the profile determined for the wild type protein.

Molecular dynamics simulations

The dynamical behaviour of the oxygenated form of HbN mutants was examined by means of extended MD simulations and compared to the results reported in previous studies for the wild type protein [7,8]. The X-ray structure of wild type *Mtb* HbN (PDB entry 1IDR, chain A, solved at 1.9 Å resolution) was used as

Table 2. NO-dioxygenase activity of PheE15 gate mutants of HbN.

Protein	NOD activity[a]	% NOD activity
Wild type	27.8±1.3	100
PheE15Ala	15.9±1.4	51.1
PheE15Ile	12.6±0.6	45.3
PheE15Tyr	9.9±0.6	34.5
PheE15Trp	8.6±0.4	30.2

The NOD activity of HbN mutants were determined at fixed concentration of NO (1.8 micromole).
[a]The activity is expressed as nmole NO/heme/s^{-1}.
doi:10.1371/journal.pone.0049291.t002

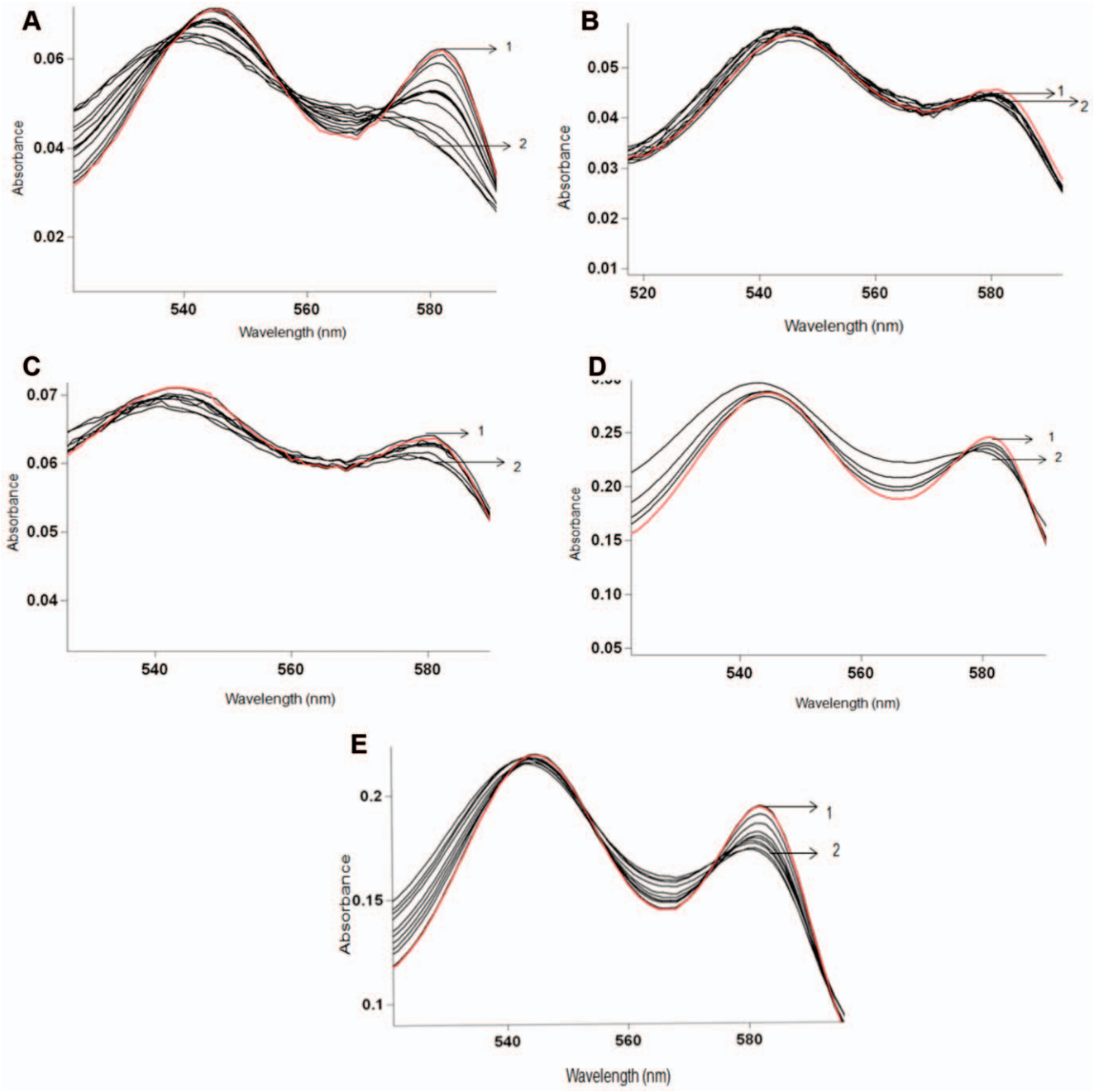

Figure 3. NO oxidation profile of PheE15 gate mutants of HbN. Titration of oxygenated HbN protein (20 μM) was done by adding 15 μM NO sequentially and recording spectra after each addition. Wild type HbN displayed fully oxidized spectra after 12 additions (A), whereas mutants PheE15Tyr (B), PheE15Ile (C), PheE15Trp (D) and PheE15Ala (E) displayed very slow oxidation of the protein and could not be fully oxidized even after 20 additions of NO. The first and last additions are labeled as 1 and 2, respectively.
doi:10.1371/journal.pone.0049291.g003

starting point for simulations. Mutants were generated by replacing PheE15 by Ala, Ile and Tyr in the X-ray structure of the wild type protein. In all cases simulations were performed using the same protocol adopted in our previous studies [7,8]. Briefly, the enzyme was immersed in a pre-equilibrated octahedral box of TIP3P [18] water molecules. The final systems contained the protein and around 8600 water molecules (*ca.* 28,270 atoms). The system was simulated in the NPT (1 atm.; 298 K) ensemble using SHAKE [19] to keep bonds involving hydrogen atoms at their equilibrium length, periodic boundary conditions, Ewald sums for treating long range electrostatic interactions [20], and a 1 fs time step for the integration of Newton's equations. All simulations were performed with the parmm99SB force field [21] and employing heme parameters developed in previous works [7,8].

MD simulations were performed with the PMEMD module of the AMBER10 program [22]. The geometry of the models was relaxed by energy minimization carried out in three steps where hydrogen atoms, water molecules and finally the whole system were minimized. Equilibration was performed in successive 50 ps

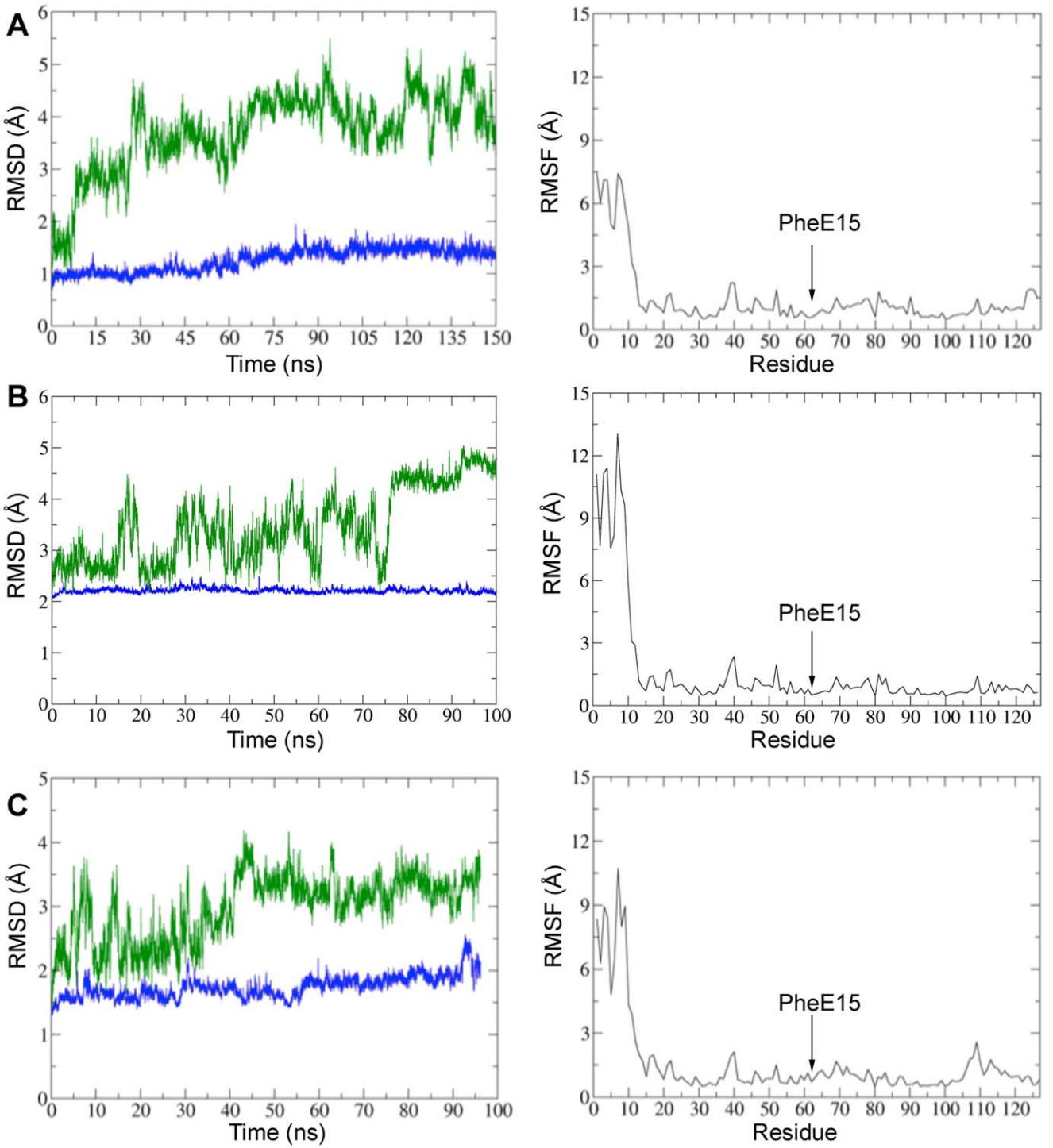

Figure 4. Representation of rmsd and rmsf profiles for PheE15 gate mutants of HbN. (Left) Rmsd (Å) of the protein backbone determined using the X-ray structure (1IDR; subunit A) as reference. The rmsd of the whole protein is shown in green, whereas the rmsd of the residues in the protein core (excluding those in the pre-A segment; residues 1–15) is shown in blue. (Right) Representation of the rmsf (Å) of residues side chains in the protein. The plots correspond to the mutants (A) PheE15Ala, (B) PheE15Ile and (C) PheE15Tyr. The location of the mutated residue Phe(62)E15 is indicated in the plots by an arrow (helix E encompass residues 51–66).
doi:10.1371/journal.pone.0049291.g004

runs where the temperature was gradually increased from 100 K to 298 K in four steps at constant volume, followed by an additional step run at constant pressure for 100 ps. Then, a series of 100–150 ns MD simulations (at 298 K and 1 atm) were run. The analysis of the trajectories was performed using frames collected every 1 ps during the production runs. Furthermore, 75 MD simulations (25 per mutant) were run to explore the pathways for ligand access (free NO in solution) to the heme cavity

Table 3. Global similarity index determined by comparison of the motions of the protein backbone in the oxygenated form of wild type HbN and the PheE15 mutants.

ξ_{AB}	Wild type	PheE15Ala	PheE15Ile	PheE15Tyr
Wild type	0.68	0.65	0.60	0.62
PheE15Ala		0.67	0.63	0.60
PheE15Ile			0.74	0.64
PheE15Tyr				0.78

The comparison is made considering the 10 most relevant essential motions, which encompass 60–75% of the structural variance along the trajectory.
doi:10.1371/journal.pone.0049291.t003

in PheE15Tyr, PheE15 Ile and PheE15Ala. To this end, five structures of the protein were taken from the last 25 ns of the trajectories run for the oxygenated mutants. These snapshots were used as starting points for unrestrained simulations run in presence of NO, which was placed at random positions around the protein (5 distinct random positions per protein snapshot). The systems were thermalized following the protocol mentioned above, and MD simulations were run up to 20 ns using the same simulation conditions.

Essential Dynamics

The dynamical behavior of HbN and its mutants was explored by means of essential dynamics [23,24]. Residues 1–15 were excluded as this region is very flexible and would mask the

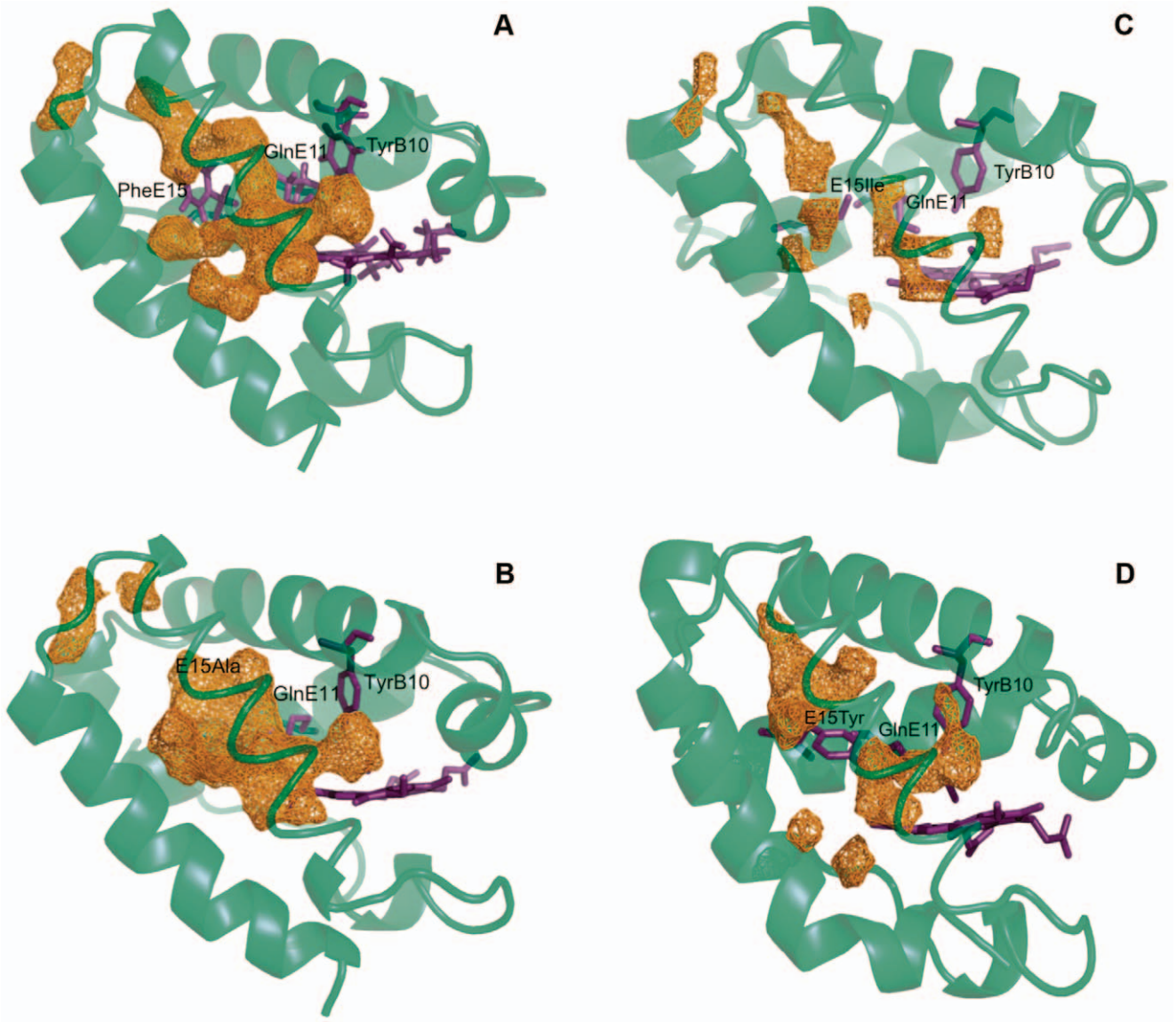

Figure 5. Representation of the accesible volume in wt HbN and its mutants. The accessible volume determined from MDpocket analysis is achieved for a density isocontour of 6.7 in the case of wt protein (A). The use of the same isocontour shows discontinuities in the accessible volume of the tunnel long branch for the different mutants. The disruption is located around the position of the gate in the case of PheE15Ile (C) and PheE15Tyr (D) mutants. For the PheE15Ala species (B) the major disruption involves the region close to the channel entry. Continuous progression of the accessible volume is achieved when the isocontour value is reduced to 5.4 for PheE15Ile and PheE15Tyr, and to 3.4 for PheE15Ala. In the plots the protein backbone corresponds to the energy-minimized structure obtained by averaging the snapshots sampled in the last 0.1 ns for each trajectory.
doi:10.1371/journal.pone.0049291.g005

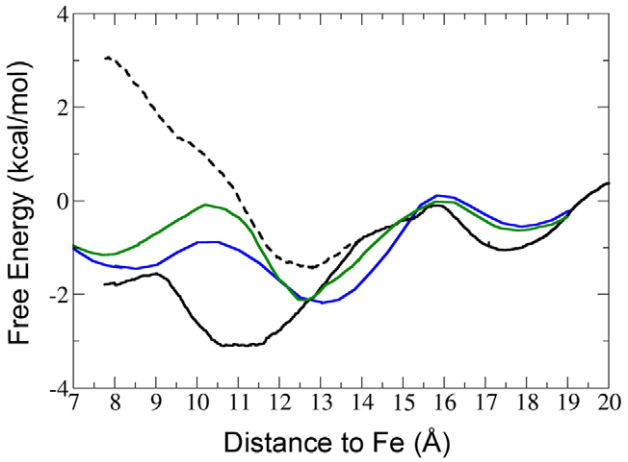

Figure 6. Free energy profile determined for NO migration along the long tunnel branch. MSMD calculations were performed to determine the energetics of ligand migration through the tunnel long branch for Phe15Ile (green) and PheE15Tyr (blue). The profiles are compared with those determined for ligand migration in both *open* (solid line) and *closed* (dashed line) states of oxygenated wt HbN. The free energy is given in kcal/mol, and the distance of the ligand from the heme iron is given in angstroms. For the sake of clarity, error bars are not displayed.
doi:10.1371/journal.pone.0049291.g006

essential motions of the protein core. The backbone atoms were used to superpose the structures sampled in order to derive the essential motions. To this end, for each trajectory the positional covariance matrix of the backbone atoms was built up and diagonalized. The eigenvectors define the type of essential motions of the backbone, and the eigenvalues determine how much of the positional variance in the trajectory is explained by each eigenvector.

Ligand Migration Profiles

The effect of PheE15 mutation on the migration of ligands was examined using two techniques. The preferred docking sites and migration pathways were identified using MDpocket [25]. Then, the migration free energy profiles were obtained using Multiple Steered Molecular Dynamics (MSMD) [26].

MDpocket is a pocket detection program that uses a fast geometrical algorithm based on a Voronoi tessellation centered on the atoms and the associated alpha spheres, which are clustered and filtered giving origin to pockets and channels [27]. These pockets are then used to identify docking sites and migration paths along the protein matrix. Analyses were performed using 10000 snapshots taken equally spread over the last 50 ns of the trajectories. The minimum and maximum alpha sphere radius was 2.8 Å and 5.5 Å, respectively. The identified cavities were superposed in time and space and a density map was generated from this superposition. Stable cavities are identified as high-density 3D isocontours, while low-density isocontours denote transient or nearly non-existent cavities in the MD simulation.

MSMD simulations were run to evaluate the free energy profiles of ligand migration through the tunnels using Jarzynski's equality [26], which estimates the free energy from an ensemble of irreversible works along the same reaction coordinate. A steering potential forces the motion of the probe with constant velocity along the reaction coordinate. The reaction coordinate was the iron-ligand distance, the force constant was 200 kcal mol^{-1} $Å^{-1}$ and the pulling velocity 0.025 Å ps^{-1}. The free energy profile of

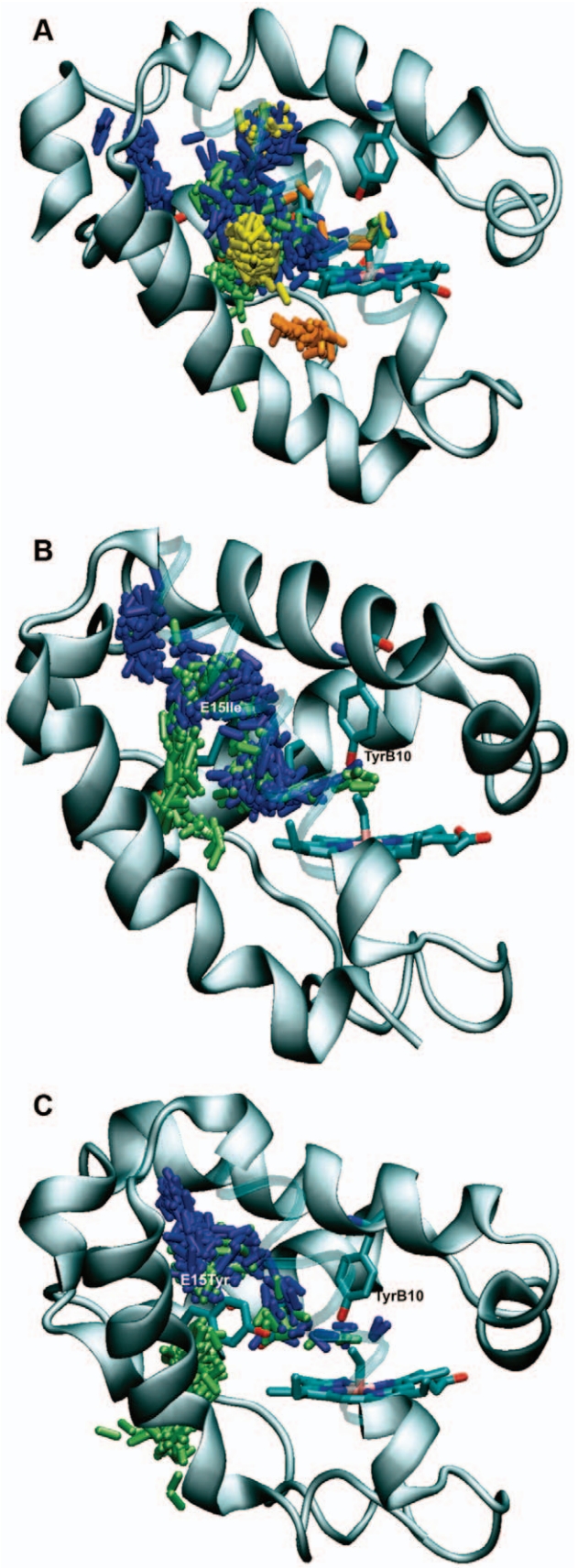

Figure 7. Representative trajectories followed by free NO ligand through the protein matrix. MD simulation of free NO located at random positions from the protein were followed to investigate the pathways leading to the heme cavity for oxygenated forms of (A) PheE15Ala, (B) PheE15Ile and (C) PheE15Tyr. The distinct pathways are indicating by showing the position of NO (represented as sticks) along the trajectory using different colors: long branch (blue), short branch (brown), EH (green), and other (yellow). Note that helix G is displayed as highly transparent cartoon for the sake of clarity.
doi:10.1371/journal.pone.0049291.g007

ligand migration along a tunnel was obtained following the computational scheme reported in previous studies [8]. At least twenty SMD simulations were run pushing the ligand through the tunnel from the solvent towards the iron. The starting snapshot for each SMD was taken from the final structure of an equilibrated MD simulation with the ligand placed at a fixed distance from the iron. Typically those distances are chosen from the preferred docking sites found in MDpocket analysis in conjunction with short MD simulations run to examine the motion of the free diatomic ligand along the tunnel.

Results and Discussion

Four gate mutants, where PheE15 in wild type (wt) HbN was replaced by Ala (PheE15Ala), Ile (PheE15Ile), Tyr (PheE15Tyr) and Trp (PheE15Trp), were created by site-directed mutagenesis. Mutations were chosen to span a wide range of sizes, varying from the small methyl group in Ala to the large indole ring in Trp, the replacement of the planar benzene by the branched chain of Ile, and the conservative mutation of PheE15 by Tyr. It was expected that the distinct chemical nature of the side chains would translate into differences in the ligand migration through the long tunnel, which in turn should lead to differences in the NOD activity measured for the mutants. Thus, in the absence of relevant structural alterations in the tunnel due to the mutations at position E15, which might be relevant for the bulky Trp, it was expected that replacement of PheE15 to Ala should open permanently the long tunnel, whereas mutation to Trp should occlude the access of ligands. Likewise, the branched side chain of Ile was expected to limit the accessibility of diatomic ligands through the tunnel. Finally, the conservative PheE15Tyr mutation was *a priori* expected to have little effect on the migration properties.

Effect of Mutations at PheE15 Gate of HbN on O_2/CO Binding

Absorption spectra of O_2 and CO bound forms of mutants were indistinguishable from that of wt HbN (Fig. 2), suggesting that all these mutants bind O_2. The ability to bind O_2 was further assessed by measuring the p^{50} values (Table 1). For the wt protein, the p^{50} value was 0.019 (mm Hg), which compares well with previous data [1]. When the PheE15 gate mutants were compared with wt HbN, no significant difference in their p^{50} profile was observed suggesting that the O_2 binding properties of mutants are not impaired. To substantiate these results, the rate of CO association was also determined to characterize the kinetics of ligand association (Table 1). The k_{on} value determined for the wt protein (2.5×10^7 M^{-1} s^{-1}) is slightly larger than the value reported by Couture *et al.* (0.657×10^7 M^{-1} s^{-1}) [1]. Nevertheless, all the mutants displayed CO association rates comparable to that of wt HbN, indicating that mutation at PheE15 residue does not affect the O_2/CO binding properties of HbN.

Table 4. Analysis of the migration pathways followed by a free NO in a simulation box containing the solvated proteins PheE15Ala, PheE15Ile and PheE15Tyr.

Mutant	Effective path[a]	Long branch[b]	Short branch[c]	EH[d]	Other
PheE15Ala	18 (72.4%)	5	3	7	3
PheE15Ile	21 (85.7%)	15	0	6	0
PheE15Tyr	17 (70.0%)	12	0	5	0

25 independent MD simulations were examined for each mutant in order to determine the migration route followed by NO to reach the heme cavity.
[a]Fraction of trajectories where the ligand was able to reach the heme cavity in the simulation time. The distinct pathways are displayed in Figure 7 using different colors: long branch (blue), short branch (brown), EH (green), and other (yellow).
[b]Defined primarily by helices B and E.
[c]Defined primarily by helices G and H.
[d]This pathway is defined by residues located in helices E and H.
doi:10.1371/journal.pone.0049291.t004

Mutations at PheE15 Gate of HbN Alter its NOD Activity

Even though mutants exhibit very similar O_2 binding properties, relevant differences were observed in their NO metabolizing activities (Table 2). The NOD activity of PheE15Ile was reduced to around 55% of the activity measured for the wt enzyme, whereas a larger reduction (around 70%) in NOD activity was observed for the PheE15Trp mutant. Unexpectedly, mutation of PheE15 to Tyr also yielded a significant reduction (around 65%) in the NOD activity, suggesting that the apparently conservative replacement of benzene by phenol has a drastic influence on the ligand migration properties of the mutant. Finally, the PheE15Ala mutant also exhibited a significant reduction (around 49%) in the NOD activity.

Oxidation of NO by Oxygen Adduct of PheE15 Gate Mutants of HbN

The NO oxidation profile of wt HbN and its mutants was determined by titrating the oxy forms of protein with NO in a time course manner (Fig. 3). The addition of NO (5 μM) resulted in the appearance of a partially oxidized spectrum of HbN and repeated addition of NO solution to this sample resulted in a fully oxidized spectrum shifting Soret peak of oxyHbN from 415 to 405 nm. In contrast, similar additions of NO to the oxygenated form of mutants PheE15Trp, PheE15Ile and PheE15Tyr did not change the spectra to the oxidized form immediately and changed slowly after 30–35 min of exposure, indicating very slow NO oxidation. Finally, NO oxidation by PheE15Ala mutant displayed a spectral profile similar to PheE15Ile and PheE15Tyr, which is intermediate between those observed for the wt protein and the PheE15Trp mutant.

MD Simulations

The preceding data indicate that the different PheE15 mutations do not affect the binding of O_2 to the heme. However, since the mutants exhibit a distinctive reduction in the NOD activity, the PheE15 residue has to play a key role in mediating the access of NO to the oxygenated protein. On the basis of these findings, MD simulations were run with a twofold purpose: to examine the structural integrity of the overall protein fold, and to identify local changes in the long branch tunnel that might affect the ligand migration. To this end, a series of 100–150 ns MD simulations were run for the heme-bound O_2 forms of PheE15Ala, PheE15Ile and PheE15Tyr mutants, and the results were

compared with those obtained for the wt protein. This simulation time has been shown suitable to describe the conformational transitions of PheE15 in our previous studies for the wt HbN [7–9]. Choice of the simulation time, however, was also dictated by consistency in the analysis of the structural and dynamical properties of the simulated systems, either related to the overall features of the protein backbone or to the ligand migration through the protein matrix. Such a convengence was achieved for all the simulated systems but for the PheE15Trp mutant (see below).

For the particular case of the PheE15Tyr mutant, two MD simulations differing in the starting orientation of TyrE15 were run. Thus, on the basis of the conformational preferences found for PheE15 in both the X-ray structure [5] and previous MD studies [7,8], the phenol ring was oriented in the closed or open conformations, which prevent or facilitate ligand migration through the tunnel, respectively. When TyrE15 was in the closed orientation, the side chain remained stable, and no transitions between open and closed states were found along the whole trajectory (Fig. S1). There was only a conformational change leading to the transient formation of a hydrogen bond between the hydroxyl group of TyrE15 and the carbonyl group of Ile115. When the MD simulation started from the open conformation, the side chain of TyrE15 suddenly changed to the closed conformation after the first 12 ns and then remained stable until the end of the trajectory (Fig. S1), even though few attempts to form transient hydrogen-bond interactions with Ile115 can be observed. Since the two simulations exhibited the same behavior, hereafter discussion of PheE15Tyr mutant will be limited to the trajectory starting from the closed conformation.

Finally, the MD simulation run for the PheE15→Trp mutant was extended up to 200 ns. However, the results will not be presented here as the analysis of the trajectory points out that the structural changes induced by the mutation both in the tunnel and in the global protein structure are still not fully converged. It seems that a proper description of the structural rearrangements triggered by this mutation would require longer simulations, making it necessary to be cautious for not overinterpreting the structural changes due to the PheE15→Trp mutation, which cannot be easily accommodated in the tunnel (see Fig. S2 for details).

Structural Analysis

For all the simulations, inspection of both the time evolution of the potential energy (Fig. S3) and the rmsd (Fig. 4; see also Fig. S4) determined for the backbone atoms of the protein core (excluding the first 15 residues) supports the integrity of the simulated proteins. Thus, the rmsd of the protein core (ranging from 1.2 to 2.1 Å for the different mutants) remains very stable after the first few nanoseconds. In contrast, a much larger rmsd profile showing notable fluctuations along the trajectory is obtained when the whole protein backbone is included in the analysis. This finding indicates that the pre-A segment is very flexible in all the mutants and can adopt a large number of conformational states, as noted in the formation of distinct structural arrangements for residues 1–15 (data not shown). Therefore, the mutation does not alter the large conformational flexibility found for the pre-A segment in the wt HbN [9,28].

The geometrical arrangement of residues TyrB10 and GlnE11 in the distal cavity is a structural feature of particular relevance, as it has been proposed that opening of the gate is modulated by the oxygen-sensing properties of the TyrB10-GlnE11 pair [8,29]. In the oxygenated wt HbN these residues form a network of hydrogen bonds, where the hydroxyl group of TyrB10 is hydrogen-bonded to the heme-bound O_2, and also accepts a hydrogen bond from the side chain of GlnE11. Due to these interactions, the GlnE11 side chain lies closer to the benzene ring of PheE15 than in the deoxygenated protein, and the enhanced steric clash favors opening of the PheE15 gate upon O_2 binding. Accordingly, it might be argued that disruption of the hydrogen bonds formed by TyrB10 and GlnE11 could explain the reduction in NOD activity of the mutants. However, the analysis of the trajectories completely rules out this possibility (Fig. S5). Thus, in all the mutants the hydroxyl group of TyrB10 is hydrogen-bonded to the heme-bound O_2 (average distances about 2.85 Å), and the side chain amide nitrogen of GlnE11 is hydrogen-bonded to the TyrB10 hydroxyl group (average distances about 3.0 Å). These interactions reproduce the hydrogen bonds found in the X-ray structure, as the corresponding distances (averaged for subunits A and B) are 3.15 and 2.95 Å. Therefore, the hydrogen-bond network found in wt HbN is not affected by the PheE15 mutations, and hence one should expect that the steric pressure exerted by GlnE11 is retained in the mutated proteins.

Dynamical Analysis of the Protein Backbone

Binding of O_2 to the heme also changes the dynamical motion of the protein backbone [7,8]. Thus, essential dynamics analysis of oxygenated HbN reveals that the major motions in the deoxygenated protein affect helices C, G and H, while the largest contribution to protein flexibility comes from helices B and E in the oxygenated protein. Since helices B and E define the walls of the tunnel long branch, the increased motion of these helices should facilitate the transition between open and closed states of the gate, thus influencing the ligand migration through the tunnel. This dynamical alteration agrees with the large scale conformational change observed experimentally upon binding of NO to the ferric form of wt HbN [30], and with the occurrence of distinct conformational relaxation processes found in the kinetics of CO recombination to the protein encapsulated in gels [31].

In order to investigate whether mutation of the PheE15 gate influences the dynamics of the protein backbone and eventually affects the migration of NO in the oxygenated protein, we determined the essential dynamics of the mutants and compared them with the wt protein. Diagonalization of the positional covariance matrix for the backbone atoms points out that few motions account for a significant fraction of the protein dynamics. Nearly 50% and 70% of the backbone conformational flexibility is accounted for by the first 4 and 10 principal components (Table S1). The two first essential motions, which mainly involves motions of helices B, E and H, loop F and the hinge region around helix C, account for 22–37% of the structural variance in the backbone of the mutants, in agreement with the value (36%) determined for wt HbN.

The similarity between the structural fluctuations of the protein backbone in wt HbN and its mutants was measured by means of the similarity index ξ_{AB} (see Text S1), which takes into account the nature of the essential motions and their contribution to the structural variance of the protein [32]. When the 10 most relevant motions are considered, the similarity index varies in the range 0.60–0.65, which is slightly lower than the self-similarities obtained for wt HbN and mutants (Table 3). These results point out that mutations preserve to at large extent the dynamical behavior of the protein. For the sake of comparison, the similarity indexes determined for the 10 most essential motions between wt HbN and the mutants TyrB10Phe and GlnE11Ala only amount to 0.47 and 0.38, respectively [27], indicating that the hydrogen-bond

network formed by the TyrB10-GlnE11 pair has a larger impact on the protein dynamics than mutation of PheE15.

Ligand Migration

Since the preceding results did not reveal significant changes neither in the hydrogen-bond network of TyrB10-GlnE11 pair nor in the dynamical behavior of the protein skeleton, the reduction in NOD activity determined for PheE15 mutants might reflect a reduced accessibility of ligands for migrating through the long tunnel. To corroborate this hypothesis, we determined the shape of internal tunnels by using MDpocket, which provides a grid that encloses the protein, where each grid point is assigned an occupancy value that denotes the accessibility of the volume associated to that point [23].

For the wt HbN the tunnel long branch appears as a continuous cavity leading from the protein surface to the heme cavity, as noted by the continuous progression of the accessible volume isocontour shown in Fig. 5. In contrast, the representation of the same isocontour for the mutants reveals a discontinuous channel, even in the case of the mutation to Ala.

For mutants PheE15Ile and PheE15Tyr, such a disruption affects the region that surrounds the mutated residue, suggesting that ligand migration through the tunnel long branch is impeded by the steric hindrance imposed by the side chains of the mutated residues (Fig. 5C,D). This is confirmed by the free energy profiles determined by MSMD calculations for these mutants, where the limiting step for ligand migration is associated to surpassing the gate (Fig. 6). In fact, the free energy profiles are intermediate between those obtained for the wt HbN with the PheE15 gate in either closed or open conformational states. Compared to the wt protein in the open state, mutation of the gate slightly destabilizes the minimum located at around 11 Å (i.e., the docking site before the gate), and increases the barrier required to pass above the side chain of the mutated residue in order to access the heme cavity. Therefore, a small diatomic ligand such as NO is expected to be trapped effectively at the highly hydrophobic entrance of the long branch, thus enhancing the local concentration, but access to the heme cavity is mainly limited by the hindrance due to the side chain of the mutated gate.

In contrast with the preceding findings, the isocontour is continuous around the mutated gate in the PheE15Ala mutant, as expected from the small side chain of Ala. However, compared to the wt protein (Fig. 5A), there is a significant occlusion at the entrance of the channel (Fig. 5B), which stems from a slight readjustment of helices B and G that reduces the width of the channel entry by 0.4–0.6 Å (as measured from distances between Cα atoms of residues located at the helical ends). Accordingly, the probability of the ligand to be trapped at the entrance of the tunnel long branch is lower compared to wt HbN. In turn, this finding raises the question about the existence of alternative pathways that can justify the remaining NOD activity (around 51% compared to wt protein) retained by PheE15Ala mutant. To this end, we examined the trajectory followed by a free NO in a water box containing the PheE15Ala mutant and determined the routes leading to the heme cavity in 25 independent MD simulations. The results (see Table 4) showed that 18 out of 25 trajectories were successful in allowing the ligand (NO) to achieve the heme cavity within the simulation time. Nevertheless, only 5 trajectories showed that NO migrates via the tunnel long branch, and in 7 simulations the entry pathway involved the EH tunnel (defined by residues in helices E and H) reported by Daigle et al. [33]. Remarkably, in 3 trajectories NO was able to reach the heme cavity through the short branch, and in other 3 trajectories NO accessed the heme cavity via a distinct channel (see Fig. 7A). Thus, even though the reduction in NOD activity can be related to the occlusion of ligand access at the beginning of the tunnel long branch, this effect is counterbalanced by the existence of three alternative entry pathways, which arise from slight structural alterations in the protein skeleton. This finding reveals the delicate structural balance imposed by the PheE15 gate, which not only regulates ligand migration, but also contributes to avoid the collapse of helices B and E, thus preserving the structural integrity and ligand accessibility along the tunnel long branch.

For the sake of completeness, this analysis was also performed for PheE15Ile and PheE15Tyr mutants. For these mutants the access routes leading to the heme cavity were significantly different. Thus, the trajectories primarily involved migration through the tunnel long branch (Table 4), which should be considered the main pathway for ligand migration in the oxygenated protein. In this pathway, the ligand remained docked in a region before the gate for significant periods of time (as noted in the high density of NO molecules located before the mutated gate residue; see Fig. 7B,C) until it was able to surpass the barrier due to the side chain of Ile/Tyr and access the heme cavity. There were some attemtps to get the heme cavity through the short tunnel, but they were unsuccessful. Finally, only in very few cases the ligand entered the protein through the tunnel EH, leading to the docking site located before the mutated gate residue. Therefore, these findings are in contrast with previous modeling studies where the short tunnel was reported to be the main route for NO diffusion [34]. Furthermore, present results indicate that the main route in PheE15Ile and PheE15Tyr is the tunnel long branch, which supports the role of the tunnel long branch in the dual-path migration mechanism [7,8] and particularly the functional relevance of the PheE15 gate.

Conclusion

The experimental data collected for the mutants indicate that the PheE15 mutation does not affect the binding of O_2 to the heme, as noted in the similar absorption spectra of O_2 and CO bound forms, as well as in the similar p^{50} and k_{on} values determined for both wt and mutated proteins. These findings suggest that the PheE15 mutation has little impact on the tunnel short branch, which is proposed to be the main pathway for migration of O_2 to the heme cavity. However, since the mutants exhibit a distinctive reduction in the NOD activity, PheE15 residue has to play a key role in mediating the access of NO to the oxygenated protein. In agreement with the dual-path migration mechanism [7,8], the main pathway for NO migration is the tunnel long branch. This finding points out the delicate structural balance imposed by the PheE15 gate, which not only regulates ligand migration, but also contributes to avoid the collapse of helices B and E, thus preserving the ligand accessibility along the tunnel long branch. Overall, the results presented herein demonstrate the pivotal role of PheE15 in modulating the NOD function of Mtb HbN, thus confirming the suggestion by Milani and coworkers [5] about the gating role of PheE15 in HbN.

Supporting Information

Figure S1 Representation of the conformational orientation of the TyrE15 side chain in the two trajectories run for the PheE15Tyr mutant. Time (ns) evolution of the dihedral angle H-Cα-Cβ-Cδ (degrees) of TyrE15 in the simulation started by placing the phenol ring in (top) open and (bottom) closed conformations, following the two main orientations found for the side chain of PheE15 gate in wild type HbN [7,8].
(TIF)

Figure S2 Representation of structural changes for the PheE15Trp mutant. (Top) Superposition of the backbone of the snapshots sampled at 40 (green) and 180 (orange) ns along the trajectory run for the PheE15Trp mutant. The plot shows the drastic change in the orientation of the Trp side chain, the displacement of the heme, and the structural rearrangement of several helices. For the sake of clarity, helix G is hown as ribbon. (Bottom) Time (ns) evolution of the dihedral angle (degrees) that determines the orientation of the indole ring of Trp.
(TIF)

Figure S3 Representation of the potential energy for simulated systems. Time (ns) evolution of the potential energy (x 10^3; kcal/mol) for the simulations of the oxygenated PheE15 mutants. Top: (left) PheE15Ala; (right) PheE15Ile. Bottom: PheE15Tyr in the simulation started by placing the Tyr side chain in (left) closed and (right) open conformations.
(TIF)

Figure S4 Representation of rmsd and rmsf profiles for PheE15Tyr gate mutant of HbN (trajectory started from open conformation). (Left) Rmsd (Å) of the protein backbone determined using the X-ray structure (1IDR; subunit A) as reference. The rmsd of the whole protein is shown in green, and the rmsd of the residues in the protein core (excluding the pre-A segment; residues 1–15) is shown in blue. (Right) Representation of the rmsf (Å) of residues in the protein. The plots correspond to the trajectory run started by placing the side chain of TyrE15 in the open conformation.
(TIF)

Figure S5 Representation of hydrogen-bond distances for the TyrB10-GlnE11. Time (ns) evolution of distances (Å) from the TyrB10 hydroxyl oxygen to the heme-bound O_2 and from the GlnE11 side chain amide nitrogen to the TyrB10 hydroxyl oxygen are shown in blue and green, respectively. Top: (left) PheE15Ala; (right) PheE15Ile. Bottom: PheE15Tyr in the simulation started by placing the Tyr side chain in (left) closed and (right) open conformations.
(TIF)

Table S1 Structural variance (%) of the protein backbone. The contribution of the first essential motions to the structural variance is gindicated for the mutated forms of HbN. The cumulative value is given in parenthesis.
(DOCX)

Text S1 Global similarity between two sets of essential eigenvectors.
(DOCX)

Acknowledgments

We would like to thank Dr. S. Kundu, University of Delhi, South Campus, Delhi, India for helping in ligand binding studies on HbN mutants.

Author Contributions

Conceived and designed the experiments: DAE KLD FJL. Performed the experiments: AO SS ABC FF LB MAM. Analyzed the data: ABC MAM DAE KLD FJL. Wrote the paper: DAE KLD FJL.

References

1. Couture M, Yeh SR, Wittenberg BA, Wittenberg JB, Ouellet Y, et al. (1999) A cooperative oxygen-binding hemoglobin from *Mycobacterium tuberculosis*. Proc Natl Acad Sci USA 96: 11223–11228.
2. Ouellet H, Ouellet Y, Richard C, Labarre M, Wittenberg BA, et al. (2002) Truncated hemoglobin HbN protects *Mycobacterium bovis* from nitric oxide. Proc Natl Acad Sci USA 99: 5902–5907.
3. Pathania R, Navani NK, Gardner AM, Gardner PR, Dikshit KL (2002) Nitric oxide scavenging and detoxification by the *Mycobacterium tuberculosis* haemoglobin, HbN in *Escherichia coli*. Mol Microbiol 45: 1303–1314.
4. Pawaria S, Lama A, Raje M, Dikshit KL (2008) Responses of *Mycobacterium tuberculosis* hemoglobin promoters to in vitro and in vivo growth conditions. Appl Environ Microbiol 74: 3512–3522.
5. Milani M, Pesce A, Ouellet Y, Ascenzi P, Guertin M, et al. (2001) *Mycobacterium tuberculosis* hemoglobin N displays a protein tunnel suited for O_2 diffusion to the heme. EMBO J 20: 3902–3909.
6. Milani M, Pesce A, Ouellet Y, Dewilde S, Friedman J, et al. (2004) Heme-ligand tunneling in Group I truncated hemoglobins. J Biol Chem 279: 21520–21525.
7. Crespo A, Marti MA, Kalko SG, Morreale A, Orozco M, et al. (2005) Theoretical study of the truncated hemoglobin HbN: Exploring the molecular basis of the NO detoxification mechanism. J Am Chem Soc 127: 4433–4444.
8. Bidon-Chanal A, Marti MA, Crespo A, Milani M, Orozco M, et al. (2006) Ligand-induced dynamical regulation of NO conversion in *Mycobacterium tuberculosis* truncated hemoglobin-N. Proteins 64: 457–464.
9. Lama A, Pawaria S, Bidon-Chanal A, Anand A, Gelpí JL, et al. (2009) Role of Pre-A motif in nitric oxide scavenging by truncated hemoglobin, HbN, of *Mycobacterium tuberculosis*. J Biol Chem 284: 14457–14468.
10. Milani M, Pesce A, Nardini M, Ouellet H, Ouellet Y, et al. (2005) Structural bases for heme binding and diatomic ligand recognition in truncated hemoglobins. J Inorg Biochem 99: 97–109.
11. Ascenzi P, Bolognesi M, Milani M, Guertin M, Visca P (2007) Mycobacterial truncated hemoglobins: From genes to functions. Gene 398: 42–51.
12. Lama A, Pawaria S, Dikshit KL (2006) Oxygen binding and NO scavenging properties of truncated hemoglobin, HbN, of *Mycobacterium smegmatis*. FEBS Lett 580: 4031–4041.
13. Kaur R, Pathania R, Sharma V, Mande SC, Dikshit KL (2002) Chimeric vitreoscilla hemoglobin (VHb) carrying a flavoreductase domain relieves nitrosative stress in *Escherichia coli*: New insight into the functional role of VHb. Appl Environ Microbiol 68: 152–160.
14. Appleby CA (1978) Purification of *Rhizobium* cytochromes P-450. Methods Enzymol 52: 157–166.
15. Gardner PR (1998) Nitric oxide dioxygenase: an enzymic function for flavoglobin. Proc Natl Acad Sci USA 95: 10378–10383.
16. Giardina B, Amiconi G (1981) Measurement of binding of gaseous and nongaseous ligands to hemoglobins by conventional spectrophotometric procedures. Methods Enzymol 76: 417–427.
17. Rohlfs RJ, Mathews AJ, Carver TE, Olson JS, Springer BA, et al. (1990) The effects of amino acid substitution at position E7 (residue 64) on the kinetics of ligand binding to sperm whale myoglobin. J Biol Chem 265: 3168–3176.
18. Jorgensen WL, Chandrasekhar J, Madura JD, Impey RW, Klein ML (1983) Comparison of simple potential functions for simulating liquid water. J Chem Phys 79: 926–935.
19. Ryckaert JP, Ciccotti G, Berendsen HJC (1977) Numerical integration of the cartesian equations of motion of a system with constraints: Molecular Dynamics of *n*-alkanes. J Comput Phys 23: 327–341.
20. Darden T, York D, Pedersen L (1993) Particle mesh Ewald: An N log(N) method for Ewald sums in large systems. J Chem Phys 98: 10089–10092.
21. Hornak V, Abel R, Okur A, Strockbine B, Roitberg A, et al. (2006) Comparison of multiple Amber force fields and development of improved protein backbone parameters. Proteins 65: 712–725.
22. Case DA, Darden TA, Cheatham TE III, Simmerling CL, Wang J, et al. AMBER, version 10, University of California, San Francisco, CA, 2008.
23. García A (1992) Large-amplitude nonlinear motions in proteins. Phys Rev Lett 68: 2696–2699.
24. Amadei A, Linssen AB, Berendsen HJC (1993) Essential dynamics of proteins. Proteins 17: 412–425.
25. Schmidtke P, Bidon-Chanal A, Luque FJ, Barril X (2011) MDpocket: open-source cavity detection and characterization on molecular dynamics trajectories. Bioinformatics 27: 3276–3285.
26. Jarzynski C (1977) Non equilibrium equality for free energy differences. Phys Rev Lett 78: 2690–2693.
27. Le Guilloux V, Schmidtke P, Tuffery P (2009) Fpocket: an open source platform for ligand pocket detection. BMC Bioinformatics 10: 168.
28. Savard PY, Daigle R, Morin S, Sebilo A, Meindre F, et al. (2011) Structure and dynamics of *Mycobacterium tuberculosis* truncated hemoglobin N: insights from NMR spectroscopy and molecular dynamics simulations. Biochemistry 50: 11121–11130.
29. Bidon-Chanal A, Martí MA, Estrin DA, Luque FJ (2007) Dynamical regulation of ligand migration by a gate-opening molecular switch in truncated hemoglobin-N from *Mycobacterium tuberculosis*. J Am Chem Soc 129: 6782–6788.
30. Mukai M, Ouellet Y, Guertin M, Yeh SR (2004) NO binding induced conformational changes in a truncated hemoglobin from *Mycobacterium tuberculosis*. Biochemistry 43: 2764–2770.
31. Dantsker D, Samuni U, Ouellet Y, Wittenberg BA, Wittenberg JB, et al. (2004) Viscosity-dependent relaxation significantly modulates the kinetics of CO

recombination in the truncated hemoglobin TrHbN from *Mycobacterium tuberculosis*. J Biol Chem 279: 38844–38853.
32. Perez A, Blas JR, Rueda M, Lopez-Bes JM, de la Cruz X, et al. (2005) Exploring the essential dynamics of B-DNA. J Chem Theory Comput 1: 790–800.
33. Daigle R, Guertin M, Lagüe P (2009) Structural characterization of the tunnels of *Mycobacterium tuberculosis* truncated hemoglobin N from molecular dynamics simulations. Proteins 75: 735–747.
34. Daigle R, Rousseau JA, Guertin M, Lagüe P (2009) Theoretical investigations of nitric oxide channeling in Mycobacterium tuberculosis truncated hemoglobin N. Biophys J 97: 2967–2977.

Supporting Information

Role of PheE15 Gate in Ligand Entry and Nitric Oxide Detoxification Function of Mycobacterium Tuberculosis Truncated Hemoglobin N

Ana Oliveira, Sandeep Singh, Ael bidon-Chanal, Flavio Forti, Marcelo A. Martí, Leonardo Boechi, Dario A. Estrin, Kanak L. Dikshit , F. Javier Luque

Figure S1.

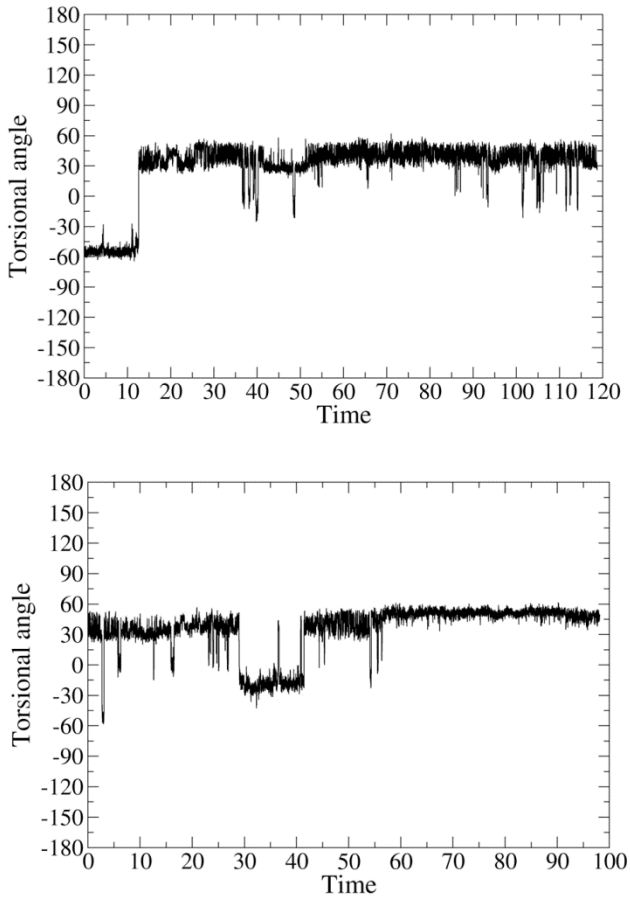

Figure S2.

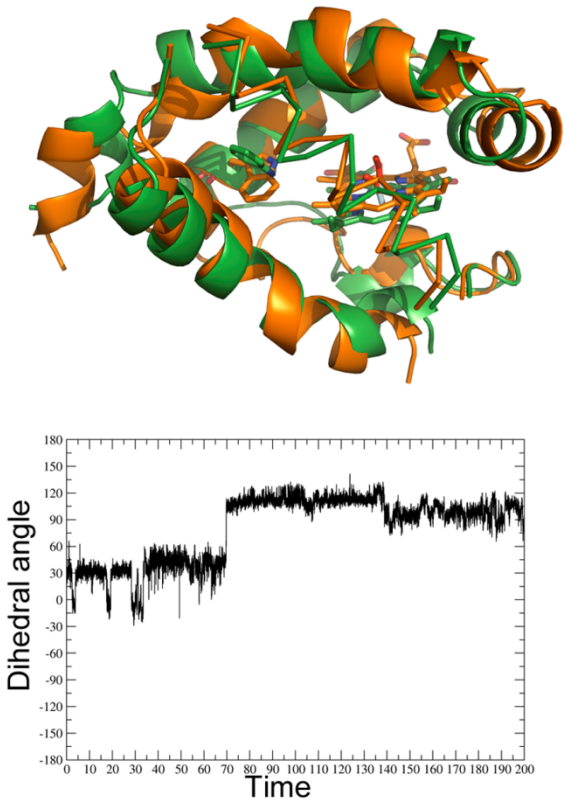

Figure S3.

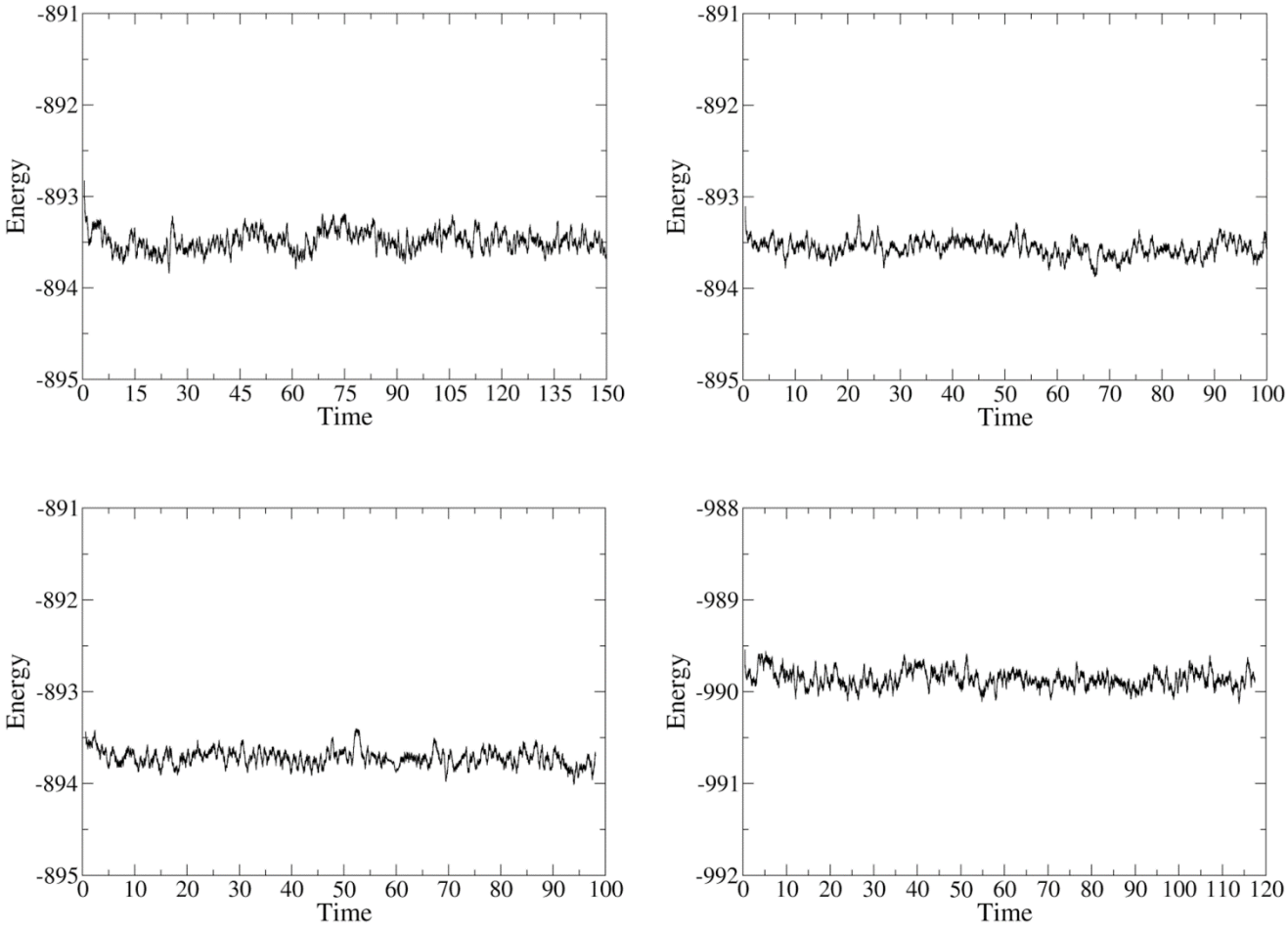
-891
-892
-893
-894
-895
Energy
0 15 30 45 60 75 90 105 120 135 150
Time
-891
-892
-893
-894
-895
Energy
0 10 20 30 40 50 60 70 80 90 100
Time
-891
-892
-893
-894
-895
Energy
0 10 20 30 40 50 60 70 80 90 100
Time
-988
-989
-990
-991
-992
Energy
0 10 20 30 40 50 60 70 80 90 100 110 120
Time

Figure S4.

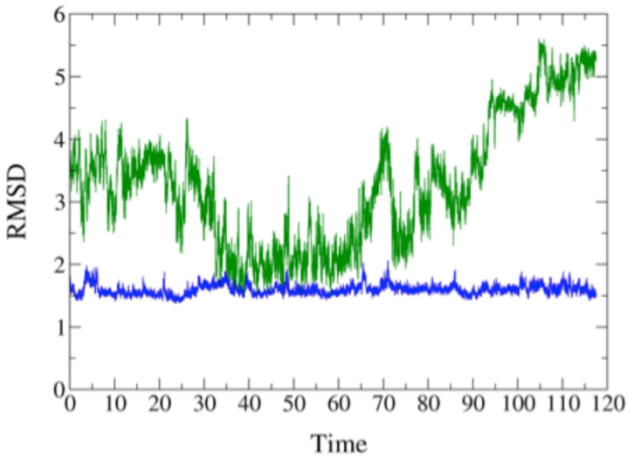

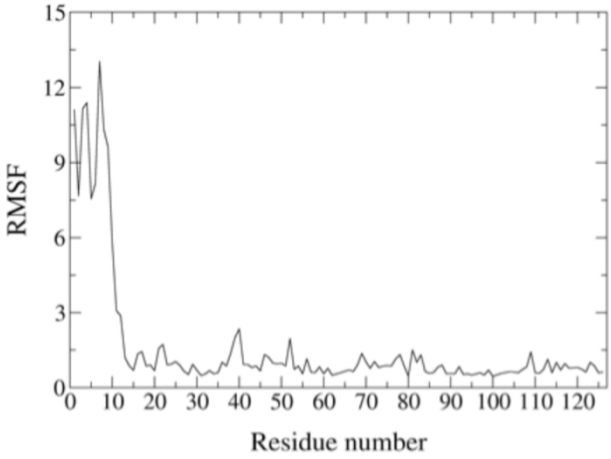

Figure S5.

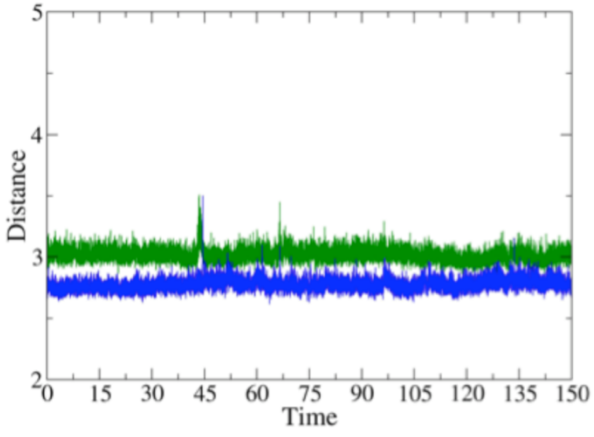

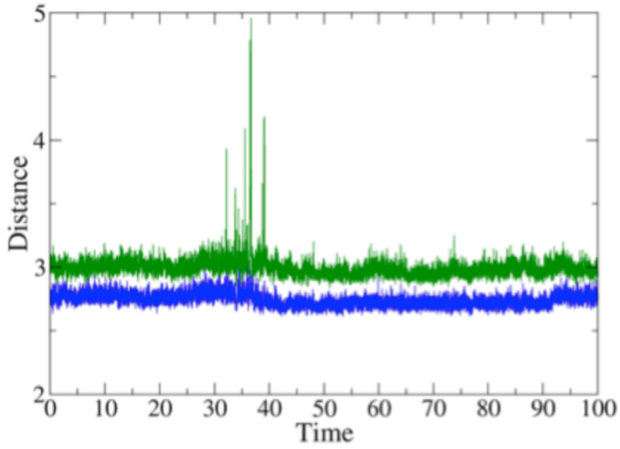

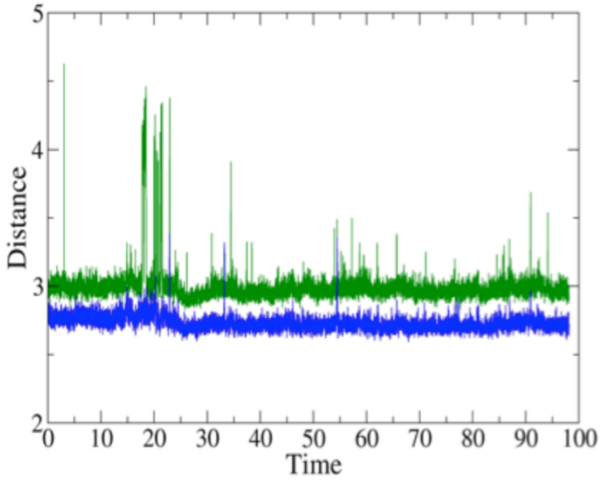

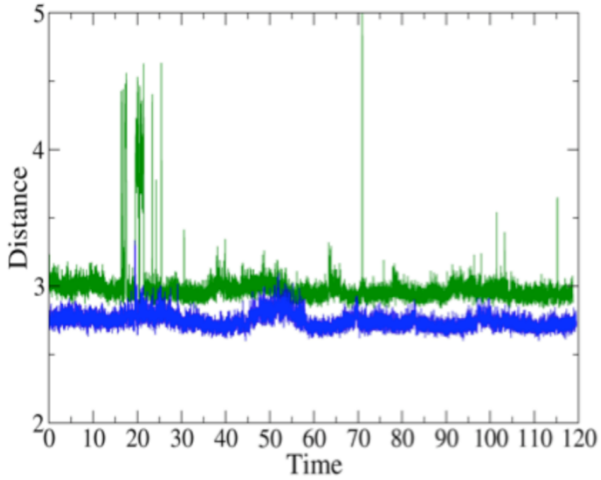

3.1.2 Mechanistic insight into the enzymatic reduction of truncated hemoglobin N of Mycobacterium tuberculosis: role of the CD loop and Pre-A motif in electron cycling

Flavohemoglobins constitute a distinct class among hemoglobin superfamily that contain two individual domains, a heme containing 3-on-3 helical globin module and a FAD binding reductase domain. It has been observed that flavoHb proteins usually function as an integral part of stress response. Their beneficial roles in nitrosative and oxidate stress prediction, and parasitic life of some pathogenic microorganisms have been show. Genomic locus of *Mycobacterium tuberculosis* encodes a putative flavoHb that displays striking differences within the regions of heme and redox domains that are functionally conserved in conventional flavoHbs. Unfortunately, the structure of this flavoHb remains unknown yet.

In order to shed light into the potential molecular determinants that mediate the interaction of flavoHb and the truncated hemoglobin N from *M. tuberculosis* (trHbN), we have examined here the interaction with a flavoHb from E.coli, which is known to conduct very efficiently the conversion of the ferric state of the protein at the end of the NO dioxygenase activity to the ferrous one. The main goals is to elaborate a 3D model of the complex between trHbN and flavoHb, to identify the key residues that mediate the interactions between proteins, and finally to estimate the rate for electron transfer from flavoHb to trHbN.

To this end, this chapter reports the molecular modeling studies carried out to build up and refine such a 3D model. The initial model of the complex was build up by using ClusPro and the refinement of the most plausible model was performed by an extended MD simulation.

The results reveal that the stability of the trHbN and Fdr complex could be due to five salt bridges interactions, Glu25-Arg362, Glu29-Lys357, Arg52-Glu226 and Arg83-FAD cofactor, together with hydrophobic contacts, between Leu36 and Met50 (HbN) with Pro339, Val 342 and Ala368 (Fdr). Finally, the residues Ser46, Thr48 and Asn49, located at the loop CD, may play a key role between the heme proprionates and the isoallaxine ring of the FAD.

MD trajectory which yielded structures of the complex in which the separation between the flavin and heme cofactors is as small as 6 Å, thus suggesting the possibility of an efficient electron transfer.

The electron transfer coupling estimated from the structures sampled in molecular dynamics simulations is 3.2×10^{-4} eV, which compares well with the value estimated for HMP of E.coli.

The present study, thus, unravels a novel mechanism by which HbN interacts with a compatible redox partner to keep itself in the functional ferrous state for the oxygen binding and NO scavenging.

Mechanistic insight into the enzymatic reduction of truncated hemoglobin N of *Mycobacterium tuberculosis*: role of the CD loop and Pre-A motif in electron cycling

Sandeep Singh,[1] Naveen Thakur,[1] Ana Oliveira,[2] Ariel Petruk,[3] Mangesh Dattu Hade,[1] Deepti Sethi,[1] Axel Bidon-Chanal,[2] Marcelo Martí,[3,4] Himani Datta,[1] Raman Prakash,[1] Dario A. Estrin,[3] F. Javier Luque[2] and Kanak L. Dikshit[1]*

[1] CSIR-Institute of Microbial Technology, Sector 39A, Chandigarh 160036, INDIA
[2] Departament de Fisicoquímica and Institut de Biomedicina (IBUB), Facultat de Farmàcia, Universitat de Barcelona, Campus de l'Alimentació Torribera, Santa Coloma de Gramenet, Spain
[3] Departamento de Química Inorgánica, Analítica, y Química Física/INQUIMAE CONICET, Facultad de Ciencias Exactas y Naturales, Universidad de Buenos Aires. Ciudad Universitaria, Pabellon 2, C1428EHA Buenos Aires, Argentina
[4] Departamento de Química Biológica, Facultad de Ciencias Exactas y Naturales, Universidad de Buenos Aires. Ciudad Universitaria, Pabellon 2, C1428EHA Buenos Aires, Argentina

Running Title: Enzymatic reduction of hemoglobin N of *Mycobacterium tuberculosis*

Key words : *Mycobacterium tuberculosis*, truncated hemoglobin, flavoreductase, electron-trasfer, molecular dynamic simulations

---

Background: The HbN of *Mycobacterium tuberculosis* carries a potent nitric oxide dioxygenase activity despite lacking a reductase domain.

Results: The NADH-ferredoxin reductase system acts as an efficient partner for the reduction of HbN.

Conclusion: The interactions of HbN with the reductase are modulated by the CD-loop and Pre-A region of HbN.

Significance: The present study provides new insights into the mechanism of electron-transfer during nitric oxide-detoxification by HbN

SUMMARY

Many pathogenic micro-organisms have evolved hemoglobin-mediated nitric oxide (NO) detoxification mechanisms, where the globin domain in conjunction with a partner reductase catalyzes the conversion of toxic NO to innocuous nitrate. The truncated hemoglobin HbN of *Mycobacterium tuberculosis* (*Mtb*) displays a potent NO dioxygenase (NOD) activity despite lacking a reductase domain. The molecular mechanism by which HbN recycles itself to carry out NO-dioxygenation and the reductase participating in this process are currently unknown. This study demonstrates that although HbN is able to interact with different flavoreductases with varying efficiency, the NADH-ferredoxin/flavodoxin reductase related protein(s) is a fairly efficient partner for the reduction of HbN. Structural docking of HbN with *E. coli* NADH-flavodoxin reductase (FdR) together with site-directed

mutagenesis revealed that the CD loop of HbN can form most suitable contacts with the reductase for the electron transfer, which is also modulated by the Pre-A motif. The electron transfer rate estimated from the structures sampled in molecular dynamics simulations is ca. $3.2x10^{-4} \pm 2.7x10^{-4}$ eV, which compares well with the value estimated for the HMP of *E. coli*. The present study, thus, unravels novel role of the CD loop and Pre-A motif in assisting the interaction of HbN with the reductase and the electron-cycling, which may be vital for its NO-scavenging function.

INTRODUCTION

Hemoglobins (Hbs) and flavohemoglobins (flavoHbs) are employed as first line of defence by many pathogenic organisms to disarm the toxicity of macrophage generated nitric oxide (NO) during intracellular infection (1-3). Truncated Hb N of *Mycobacterium tuberculosis (Mtb)* protects its host from the toxic effects of NO due to its potent O_2-dependent NO dioxygenase (NOD) activity (4, 5, 6). The HbN deficient strain of *M. bovis* displays extremely low NOD activity and lacks respiratory protection from NO as compared to the native strain (5), suggesting that the presence of HbN contributes to the survival ability of *Mtb* in the NO enriched environment of macrophages. The NOD activity of HbN converts NO into the harmless nitrate anion (6), while the heme iron is oxidised from its oxygenated active Fe^{2+} state to the inactive deoxygenated Fe^{3+} form, which is incapable of oxygen binding. Unlike many single domain Hbs, the catalytic efficiency of NO-dioxygenation by *Mtb* HbN is very high and the kinetic rate constant for NOD activity (k_{NOD} ~ 745 $\mu M^{-1}s^{-1}$) compares well with two-domain flavoHbs that are integrated with a reductase domain (1, 5). The separation of the globin and reductase domains in flavoHbs has been found to attenuate their NOD function (7). The lack of an integrated reductase diminishes the ability of many single domain Hbs and myoglobins (Mbs) to drive the NO-dioxygenation cycle (8, 9), as noted in the poor NOD activity of human Hb and sperm whale Mb (k_{NOD} ~ 89 and 43 $\mu M^{-1}s^{-1}$, respectively) (9, 10). Therefore, it is intriguing how *Mtb* HbN carries out the NOD function so efficiently, because the electron transfer event, which depends on the structural and functional compatibility with a cognate reductase partner, might limit the overall rate of NO-dioxygenation.

The molecular mechanism, by which HbN restores its reduced state at the end of the NOD cycle in the absence of an integrated reductase domain, is unknown at present. It can be anticipated that the unique structural and dynamical features of *Mtb* HbN may allow it to establish transient interactions with one or more redox partners to guarantee an effective electron cycle for NO-dioxygenation. The *Mtb* HbN carries two unusual features: a 12-residue long highly polar N-terminal Pre-A region, and a protein tunnel system composed of short and long branches (11) that have been proposed to facilitate ligand access to the distal heme site (12, 13). The functional role of the tunnel has been underlined in a dual path mechanism for ligand access to the heme cavity (14), in which binding of O_2 to the heme triggers dynamical alterations in the protein backbone that regulate the opening of the long branch via a phenylalanine gate (PheE15) (12, 14), thus facilitating the access of NO to the O_2-bound heme (15). Furthermore, it

has been shown that the backbone motion of HbN and the movement of the PheE15 gate are also modulated by the N-terminal Pre-A motif, which is highly flexible and makes transient contacts with the protein core (16). Overall, these findings point out that dynamic motion in the protein backbone might play a crucial role in modulating the NOD function of HbN.

The HbN of *Mtb* remains functionally active in *Escherichia coli*, *Salmonella enterica typhimurium* and *M. smegmatis* and allow these hosts to metabolize NO and resist nitrosative stress (4, 6, 16). These findings point out that *Mtb* HbN is able to utilize heterologous reductases as a partner to carry out NO-dioxygenation and may not be specific to its native reductase system. Indeed, it can be argued whether the crucial role played by *Mtb* HbN for the survival of the bacillus requires the expression of a specific reductase partner, which to the best of our knowledge has not been identified as yet. For efficient electron cycling, the reductase might simply require a precise coordination and structural alignment with the globin domain, so that the cofactor (heme and FAD) binding regions lie at a permissible distance for facile electron flow. Accordingly, it seems reasonable to hypothesize that HbN may establish transient interactions with one or more partners depending on their structural and functional compatibility.

In this context, it is important to identify reductases that *Mtb* HbN will prefer for its heme iron reduction during NO-detoxification and the amino acid residues or regions involved in recognition and binding to the reductase partner. It will also be important to explore if *Mtb* HbN exhibits any preferential behaviour for the partner if it comes in contact with multiple reductases of varying redox potential. To this end, we attempted to screen and study the interactions of some native and heterologous redox partners that can efficiently change the redox state of *Mtb* HbN from ferric to ferrous state. Detailed spectroscopic and structural studies presented herein unravel a novel mechanism by which HbN establishes alliance with a compatible reductase partner. The interaction involves its flexible CD loop region and is dependent on the dynamical motion of the protein backbone, which is modulated by its N-terminal Pre-A region.

EXPERIMENTAL PROCEDURES

Strains, Plasmids and Culture Conditions–E. coli strains JM109 and BL21DE3 were used routinely for the cloning and expression of recombinant genes. Bacterial cultures were grown in Luria-Bertani (LB) or Terrific Broth (containing 24 g of yeast extract, 12 g of Bacto-Tryptone, 12.54 g of K_2HPO_4, 2.31 g of KH_2PO_4) medium at 37 °C at 180 rpm. When required, ampicillin and kanamycin (Sigma) were added at a concentration of 100 and 30 mg/ml, respectively. Plasmids, pBluescript (Stratagene) and pET28c (Novagene) were used for cloning and expression of HbN encoding gene of *Mtb* and its site directed mutagenesis as described earlier (4, 16). The oligonucleotides were custom synthesized by Essence Life Sciences, India.

Cloning, Expression and Purification of CD-Loop Mutant of Mtb HbN– Mutant of *Mtb* HbN was generated by overlap PCR as described earlier (15, 16). Forward and reverse primers were designed on the basis of nucleotide sequence of the *glb*N gene as mentioned previously (4). Similarly, internal forward (5'-CCTTCT TCAGCGGTTGGATCATGAGC-3') and reverse (5'-GCTCATGATCCAACC

GCTGAA-3') primers carrying substitution of Thr48 and Asn49 with Trp and Ile, respectively, were designed and used for overlapping PCR. Incorporation of mutations was confirmed by nucleotide sequencing. The mutated gene was cloned at *Nde*I-*Bam*HI site and expressed under the T7 promoter of pET28c, The resulting *Mtb* HbN mutant was designated as $HbN^{Thr49Trp,Asn50Ile}$.

Cloning, Expression and Purification of Reductases and HbN-Reductase Chimeras–Various reductase encoding genes of *Mtb* and *E. coli* were amplified from the genomic DNA by standard PCR method using gene specific forward and reverse primers, designed on the basis of their known coding sequences. Genes for the *Mtb* reductases trxB (Rv1470), KshB (Rv3571), fdxc (Rv1177) and fprB (Rv0886), as well as the *E. coli* NADH-flavodoxin-reductase (FdR, Ec 948414) and the reductase domain of HMP were amplified by PCR, authenticated by nucleotide sequencing and expressed under the T7 promoter of pET28c. Wild type and HbN mutants were purified by Ion-Exchange Chromatography (DEAE-Sepharose, Sigma), equilibrated with 10 mM Tris · Cl (pH 8.0) and eluted using NaCl gradient, as mentioned previously (15).

HbN-reductase chimeras (HbN-KshB and HbN-FdR) were also generated. To this end, the reductase domain was attached to the C-terminal portion of *Mtb* HbN with the help of a 12-residue long linker (-GTASVLKATDTG-) carrying two glycine residues to allow sufficient flexibility for the interactions between HbN and the reductase. To generate the chimera, first the HbN and the reductase encoding genes were amplified separately by PCR. Three overlapping primers (5'-TGATGCTGTTCCGACTGGTGCCG TGGT-3'; 5'- CGCTTTCAGTACTG ATGCTGTTCC-3'; 5'-ACCGTAGAA TTCTCCCGTGTC AAT-3') encoding the linker region and carrying a XhoI restriction site at the 3'-end were incorporated at the C-terminus of the *glb*N gene by standard overlapping PCR. The linker carrying *glb*N gene was then joined with different reductase encoding genes via XhoI site and expressed under the T7 promoter of pET28c. Reductases and the HbN chimera were purified by Ni-NTA affinity chromatography using manufacturer's protocol. Expressions of recombinant proteins were visualized on a 15% SDS-PAGE. Redox states of proteins were checked spectrophotometrically by recording the Soret α and β peaks.

Assay for the HbN Reduction–The assay which was originally developed by Hayashi *et al*. (17) was used here with slight modification as described elsewhere (18). Briefly, the reaction was set up in a sealed cuvette chamber carrying a reaction mix consisting of 1μM oxidised HbN and 250μM NADH in a 0.1M phosphate buffer (pH 7.2) saturated with CO. The reaction was initiated by adding 1μM reductase with the help of a gas tight Hamilton syringe. The time course for the shift of Soret peak from 406 nm (oxidized form) to the reduced form (resulting binding of CO) was recorded at 420nm.

Measurement of Heme Content and NO-Oxidation Profile of HbN–The heme content of cells was measured by the procedure described earlier (4, 19). Briefly, heme proteins were re-suspended in 2.2M pyridine in 0.1N NaOH. Heme concentrations were determined by measuring the difference in absorption spectra at 556 and 539 nm for dithionite-reduced and ferricyanide-oxidised protein,

respectively. Titration of oxygenated *Mtb* HbN and its mutants by NO was checked essentially as described earlier (15, 16) and profiles of NO induced oxidation of the wild type HbN and its mutants were recorded after each addition of NO for the conversion of oxygenated hemoglobin into the oxidized state.

Structural Docking of Mtb HbN and FdR–The X-ray crystallographic structures of flavodoxin reductase (FdR) from *E. Coli* (PDB ID 1FDR; resolution of 1.7 Å) (20) and *Mtb* HbN (PDB ID 1IDR, chain A; resolution of 1.9 Å) (11) were used to generate the 3D models of the protein-protein complex with ClusPro2.0 in its fully automated mode (http://cluspro.bu.edu/) (21). First, a rigid body docking was performed with PIPER (22), a program that relies on the Fast Fourier Transform-based approach used with pairwise interaction potentials. The top 1000 ranked solutions obtained from PIPER were then processed with ClusPro, a clustering algorithm that groups the solutions using the root mean square deviation (RMSD) between solutions with a cut-off of 9 Å. Finally, the generated models were classified according to the weight of different coefficients as balanced, electrostatic-favored, hydrophobic-favored and van der Waals+electrostatic-favored. Choice of the final model was made on the basis of the lowest energy using the balanced ClusPro score (21, 22), the solution with the highest cluster members, and the lowest distance between the heme prosthetic group in *Mtb* HbN with respect to the flavin cofactor in FdR, and further validated by visual inspection of the contacts at the protein-protein interface.

Molecular Dynamics Simulations–The 3D structural model of the HbN/FdR complex was refined by means of extended molecular dynamics (MD) simulation (0.5 μs) performed with the PMEMD.cuda module of the AMBER12 suite (23) using the ff99SB force field (24). The heme parameters were developed and thoroughly tested by Estrin and coworkers (25, 26). Parameters for the FAD cofactor were taken from the work by Antony *et al*. (27), though the atomic charges were assigned by fitting the atomic point charges to the B3LYP/6-31G(d) quantum mechanical electrostatic potential using the RESP method (28).

To set up the systems for the MD simulations, the complex was immersed in a pre-equilibrated octahedral box of TIP3P (29) water molecules and counterions were added to maintain the neutrality of the simulated system. The final system contained the protein, 6 Na^+ cations and around 23,400 water molecules (~76,200 atoms). The equilibration protocol consisted of performing an optimization of the initial structures, followed by slow heating to the target temperature (298 K). The heating was performed in 2 ns MD at constant volume, followed by 2 ns MD at constant pressure (1 bar). Once the equilibration was completed, the system was simulated in the NPT ensemble using periodic boundary conditions, the SHAKE algorithm (30) to constrain the bonds connecting hydrogen and heavy atoms in conjunction with a 1 fs time step for the integration of Newton's equations with a Langevin collision frequency of 2 ps^{-1} (31), particle mesh Ewald for electrostatic interactions (32) and a cutoff of 10 Å for non covalent interactions. Frames were collected at 100 ps intervals for subsequent analysis of the trajectory.

The binding free energy of the complex was estimated from MM/PBSA calculations. Dielectric

constants of 4 and 80 were used for the protein interior and the aqueous environment, respectively. The dielectric boundary was taken as the solvent accessible surface defined by a 1.4 Å probe radius and the default atomic radii for the protein-protein complex in Amber12 MMPBSA.py module. A salt concentration of 150 m*M* was specified for the calculations. The solvent-accessible surface area (SASA) was estimated using the molsurf program implemented in cpptraj.

Electron Transfer Pathway Calculation–The pathway method was used to identify the most plausible pathway for electron transfer (ET) between the heme group and the FAD isoalloxazine ring, as estimated using the algorithm developed by Beratan et al. (33, 34), which was successfully used to examine the role of protein dynamics on ET rates (35). Briefly, the method looks for the path that exhibits the highest electron coupling (H_{AB}) between donor and acceptor. For a given path, H_{AB} is computed as the product of a number of steps, each with a given coupling value, that define the pathway. A step can either be through atom, when two orbitals share an atom, which are assumed to have a coupling value of 0.6, and through space steps (or jumps) connecting orbitals separated by empty space, for which the coupling is assumed to decay exponentially with the orbital to orbital distance given by a decay factor ($\beta = -1.7$). The H_{AB} value (in eV) is finally obtained by multiplying the obtained decay factor for the best ET path by 1 eV, which is the default value in the algorithm.

To obtain a proper description of the system, minor adjustments of the parameters used in the pathway algorithm were required. First, all orbitals of the heme iron were considered to be equivalent. Second, couplings between all porphyrin and FAD isoalloxazine ring located orbitals were set to one in order to reproduce their resonant character.

Peptide Synthesis–Based on the structural conformation and sequence composition of the CD-loop region of HbN, a 26-residue long peptide that includes the CD loop region (Phe45-Ser51) was synthesised using IMTECH peptide synthesis facility. The sequence of the peptide is ASMSECDPAEHCTGQSSECPADVF HK. The peptide was synthesised by automated solid phase peptide synthesis using the 9-fluorenylmethoxycarbonyl-tert-butyl (Fmoc/tBu) strategy. Peptide was purified through High Performance Liquid Chromatography (HPLC) method and its identity was confirmed by Matrix Assisted Laser Desorption Ionization (MALDI) mass spectrometry.

RESULTS

Interactions of Mtb HbN with Native and Heterologous Reductases–Since NADP-ferredoxin/flavodoxin reductase systems are known to reduce met-Hb into ferrous state (36) and similar reductase modules are found naturally fused with globins in two-domain flavoHbs, we anticipated that such reductase system may be suitable for the ET to the heme iron of *Mtb* HbN during NO-detoxification and may be utilized for its NOD function. To assess this assumption, the available expression profile and micro-array data of *Mtb* genome under various stress conditions were taken into account and some of the flavo-reductases upregulated under nitrosative/oxidative stress and hypoxia or showing sequence similarity to reductase domain of

flavoHbs were selected (see Experimental Procedures).

Six different reductases from the *Mtb*, e.g., trxA, trxB, fdx*c,* KshB, fprB and whiB1, and two reductases from *E. coli*, e. g., flavodoxin NADP reductase and the reductase domain of HMP were selected for primary screening to check their efficiency for the reduction of *Mtb* HbN to the ferrous state. Among these, fdxc expressed as inclusion bodies and fprB could not be expressed in *E.coli*. Thus, four *Mtb* redox proteins and FdR of *E. coli* were taken up further for testing their potential for the reduction of HbN. This assay exploits the ability of Hbs to form a CO-adduct in its ferrous state and giving a specific Soret peak at 420 nm after conversion of Fe^{3+} to Fe^{2+} in the presence of a compatible redox partner. Accordingly, the efficiency of *Mtb* HbN reduction was monitored spectrophotometrically by the shift and increase in the Soret peak from 406 to 420 nm due to the formation of CO adduct of HbN in the presence of different reductases.

The results showed that the efficiency of redox state change in *Mtb* HbN varied in the presence of different reductases. Among these, FdR of *E. coli* was found most effective (Fig.1), whereas trxB and KshB were able to reduce HbN with lower efficiency. Finally, whiB1 and trxA did not show any reactivity towards met-HbN.

Low Efficiency Reductase is Replaced by Efficient Reductase Partner During Reduction of HbN–Our primary screening with the reductases indicated that the FdR from *E. coli* is highly efficient for the reduction of met-HbN, whereas KshB and trxB of *Mtb* exhibited relatively lower efficiency. Within the cell, *Mtb* HbN may encounter a number of redox partners under different physiological conditions and may have different efficiency for its reduction. To mimic this scenario, *Mtb* HbN was allowed to pre-react with trxB in the presence of NADH in CO-flushed chamber to initiate the formation of Fe-CO adduct. When FdR was added in the middle of this ongoing reaction, it immediately boosted the reduction of HbN as observed by drastic increase in absorption at 420 nm due to the reduction of HbN and the formation of CO-adduct (Fig. 2), indicating replacement of pre-existing reductase with the newly added one. Similar pattern was observed when FdR was allowed to interact in midway during interactions of HbN with KshB. These results indicated that *Mt*HbN can switch its alliance from a weak to efficient redox partners to maximize the efficiency of its reduction and thus optimize the NO-dioxygenation cycle.

Integration of a Reductase Domain with HbN and Construction of HbN-Reductase Chimeras–Since efficiency of *Mtb* HbN reduction varied with different reductases, we selected flavoreductase reductase, KshB of *Mtb* and FdR of *E.coli* as representative of slow and fast acting reductases, respectively, to gain insight into the mechanism of ET during HbN reduction. The two reductases were integrated at the C-terminus of HbN to mimic the two-domain flavoHb like structure, where the reductase is naturally attached to a globin domain (Fig. 3). These chimeras were created with the notion that covalent linkage will speed up the process of forming close contact between heme and the FAD binding regions of the chimera in a proper orientation, so that the heme and the FAD moiety can come closer and facilitate the ET. The HbN-KshB and HbN-FdR chimeras were cloned, expressed and purified. The purified

proteins exhibited expected mass of 54kDa and 42kDa for *Mt*HbN-kshB and *Mt*HbN-FdR, respectively, and conferred reddish tinge to the cell when over-expressed in *E. coli*. Absorption spectra of fusion proteins resembled the oxyform spectra of *Mtb* HbN with Soret peak at 414nm and α, β peaks at 540 and 575 nm respectively, indicating the presence of functional heme domain.

We checked the efficiency of the two chimeras for the reduction of the ferric HbN by the linked reductase domain in the presence of NADH. The redox state change was monitored spectrophotometrically by *Mtb* HbN-CO adduct formation. Interestingly, instead of enhancing the efficiency of HbN reduction, integration of KshB with the HbN blocked this activity and did not show any spectral change at 406 nm and CO-adduct formation. However, the reduction of ferric HbN was restored and Soret peak shifted to 420 nm by the addition of FdR (Fig. 3D). In contrast, similarly linked FdR in the HbN-FdR chimera exhibited higher efficiency for the reduction of HbN as compared to the one observed after their interactions as individual domains (Fig. 3B).

Molecular Docking and Identification of Reactive Configuration of HbN-FdR–In the absence of any information on the redox partner of HbN for the NOD function in *Mtb*, we selected FdR as a model reductase for understanding the process of electron flow and reduction of ferric HbN. FdR was selected due to its higher efficiency in converting ferric HbN to the ferrous species, irrespective of its presence as a separate module or integrated with HbN in the form of two-domain structure. Since most inter-protein ET complexes are intrinsically low affinity and transient, docking was used to explore the interactions between HbN and FdR that can place both heme and FAD binding motifs in a permissible distance for the ET. Accordingly, attempts were made to dock the structure of the ferredoxin reductase onto HbN structure using ClusPro2.0. Out of various possible protein-protein poses (Table S1 in Supporting Information), the most probable one was selected on the basis of the largest number of members in the cluster of docked solutions (120 poses), the lowest energy as determined by using the balanced ClusPro score (-907.4; score units) and the shortest distance from the geometrical centers of heme and isoalloxazine rings (18.3 Å). In the docked pose the interaction primarily involves the CD loop of HbN, which lies close to the C-terminus of FdR. It is worth noting that the docked structure resembles the crystal structure of flavoHb (FHP) from *Alcaligenes eutrophus* (PDB entry 1CQX) with respect to the placement of two co-factor binding regions and the nature of residues at the interface (Fig. S1 at Supporting Information).

Refinement of the docked pose was accomplished by means of an extended MD simulation, which confirmed the structural integrity of both HbN and FdR in the complex. Thus, the root-mean square deviation (RMSD) of the backbone atoms along the trajectory generally ranged from 1.0 to 2.0 Å for both FdR and HbN (note that the highly flexible Pre-A and loop F regions were excluded from the analysis for HbN). Nevertheless, the relative position of the two proteins varied significantly along the MD simulation, leading to a configuration that was stable during the last 200 ns of the trajectory (Figs. S2 and S3 in Supporting Information), in which the distance between heme and flavin cofactors ranged from 6 to 9 Å, though contacts between the heme propionate

and the FAD isoalloxazine ring as short as 5 Å were transiently achieved (Fig. S2 in Supporting Information). These findings indicated the possibility of water mediated electron flow, as has been observed in other heme-reductase systems such as Mb and cytochrome b5 or two domain flavoHbs (35, 36).

In the final structure (Fig. 5), close contacts in the complex involve residues in helix B, the CD loop and beginning of helix E and F-G regions of HbN with the last 40 residues in the N-terminal segment of FdR, leading to an interface characterized by a solvent-accessible area of around 900 $Å^2$ (Fig. S2). Thus, up to five salt bridge interactions were formed along the simulation and remained stable in the last 200 ns of the trajectory (Glu25-Arg362; Glu29-Lys357; Arg52-Glu226, Asp39-Arg343, and Arg83 with the phosphate alpha of FAD). The protein-protein interface was also stabilized by hydrophobic contacts between residues Leu36 and Met50 (HbN) with Pro339, Val342 and Ala368 (FdR). Finally, a series of polar residues in the CD loop (Ser46, Thr48 and Asn49) fill the space between the heme propionates and the isoalloxazine ring of FAD. The structural integrity of the final structure of the dimer was also reflected in the progressive energetic stabilization of the complex, as a favorable binding affinity was estimated along the last 200 ns of the trajectory (Fig. S3 in Supporting Information).

The ET coupling value for all the structures was on average ca. $3.2x10^{-4}$ ± $2.7x10^{-4}$ eV, the highest value being $3.9x10^{-4}$ ± $5.4x10^{-4}$. These values compare with the ET coupling calculated for the *E. coli* flavoHb in the oxygenated ($8.0x10^{-4}$ ± $7.4x10^{-4}$ eV) structure (37). The ET pathway shows that water, Ser46 and Arg83 residues are present in 71, 40 and 32 % of all the analyzed structures, respectively (Fig. 6). The ET coupling is significantly lower ($7.2x10^{-5}$ ± $5.1x10^{-5}$ eV) in the absence of water molecules, which stresses the relevant contribution of the solvent at the protein-protein interface in assisting the ET between haem and FAD, in agreement with the critical role played by water in the ET mechanism in *E. coli* flavoHb (38).

Site-Directed Mutagenesis of MtHbN and Validation of Docked Structure of HbN and FdR Complex–To assess the reliability of the HbN-FdR complex and validate the involvement of proposed residues in ET, site–directed mutagenesis of *Mtb* HbN was performed. Since the CD-loop occupies a crucial position by maintaining a polar environment (Ser46, Thr48, Asn49) that may be important for the electron flow, we created a site-directed mutant of HbN (HbN ^{Thr49Trp,Asn50Ile}) where Thr49 and Asn50 residues were mutated to Trp and Ile, respectively, to disrupt this effect. The spectral properties of the mutant were identical to the wild type HbN, but it exhibited highly compromised reduction ability in the presence of FdR (data not shown). It is worth noting that this mutant did not display any effect on its ability to bind oxygen and oxidize NO.

Role of CD-Loop of Mtb HbN in Protein-Protein Interactions and Mediation of Electron Transfer–To further confirm the role of the CD loop in defining the interface between *Mtb* HbN and FdR, we designed a short peptide against the CD-loop region, anticipating that binding of the peptide at the interface region of FdR will obstruct the flow of electrons. To check the specificity of this peptide against CD loop, two randomly

designed peptides were also used to check their effect on reduction of ferric HbN in the presence of FdR. In the presence of CD-loop specific peptide, the Soret peak of ferric HbN at 406 nm remained unchanged in contrast to the control reaction, in which this peptide was not added. When non-specific peptides were used instead of the CD-loop specific peptide in the reaction mixture, ferric HbN was readily reduced in the presence of FdR as observed by shifting the Soret peak to 420 nm due to the formation of CO-adduct by HbN (Fig. 7), signifying the reduction of HbN.

Pre-A Motif of MtHbN is Required for the Intermolecular Electron Transfer in MtHbN-FdR Complex–Previous studies have shown that Pre-A motif modulates the dynamics of *Mtb* HbN backbone to carry out the NOD function, whereas deletion of Pre-A motif compromises the NOD function due to the hindered backbone motion (16). The main difference in the dynamics of protein structure was observed around B and E helices and the movement of CD and EF loop regions, suggesting that Pre-A deletion may affect the intermolecular interactions of HbN with FdR and the efficiency of HbN reduction. To check this possibility we compared the ability of wild type and Pre-A deleted mutant of HbN to be reduced in the presence of FdR. Interestingly, the Pre-A mutant displayed extremely slow conversion from Fe^{3+} HbN to Fe^{2+} species, as observed from the assays of CO binding to the ferrous species (Fig. 4).

To further substantiate that the Pre-A motif is modulating the reduction ability of the HbN, we also deleted the Pre-A region in the chimera of HbN-FdR and HbN-HMP reductase fusion proteins, which otherwise exhibited highly efficient ET ability. In both cases, reduction of globin domain was completely abrogated, indicating the requirement of Pre-A in regulating the CD loop of HbN for establishing the intermolecular contacts with the reductase for the catalytic cycling of electrons for carrying out NOD function (Fig . 4).

DISCUSSION

A large number of two-domain flavoHbs and Hbs in association with a suitable reductase are known to participate in NO detoxification (1, 2, 38, 39). The ability of single domain Hbs to drive NO-dioxygenation diminishes substantially in the absence of a compatible reductase partner (6, 17). *Mtb* HbN is a single domain truncated Hb that displays an efficient NO-scavenging ability by which a toxic NO molecule combines with heme-bound O_2 to form a harmless nitrate ion. The missing link in this cycle, which is integral to its uninterrupted activity, is the molecular mechanism by which HbN associates with a reductase partner to replenish itself for the next round of NOD activity. The present study demonstrates that HbN interacts efficiently with flavoreductases related to the NADH-ferredoxin reductase system and employs a novel mechanism to form a transient complex that brings redox centres of the two reacting partners in close proximity for efficient ET.

The NOD function of HbN is retained during its expression in different heterologous hosts (4, 6), indicating that it can also utilize heterologous redox partners for carrying out NO-dioxygenation and may not be restricted to a specific reductase of its native host. This can be advantageous for *Mtb* HbN to associate with various partners available under different physiological conditions to carry out

multiple functions, which can be strategically beneficial for the host. In the cellular environment, HbN may encounter plenty of electron-donors including various reductases that can have different spatial and temporal expression profiles. Therefore, it is intriguing how HbN selectively establishes transient interactions with a reductase to recycle itself efficiently. Reduction profile of HbN in the presence of various oxidoreductases suggested that flavoreductases, structurally similar to the ferredoxin-NADH reductase family, may form most compatible alliance for the enzymatic reduction of HbN and can replace the interactions of HbN with less efficient reductases. The mammalian membrane bound microsomal NADPH-cytochrome 450 reductase, which is structurally related to ferredoxin-reductase, has also been observed to participate in NOD function together with single domain Hbs displaying flavoHb like properties (40). These observations suggest that ferredoxin/flavodoxin reductases that are widely distributed in nature, can act as an efficient system for the reduction of HbN and other single domain Hbs. Other flavoreductases, e. g., KshB and trxB, were also able to transfer electrons to HbN, albeit with lower efficiency, indicating flexibility in the interactions of HbN with its reductase partner. Differential efficiency of these reductases for catalyzing the ET may be due to differences in their structural compatibility with HbN as heme and FAD domains should be in precise vicinity during transient interactions for the optimal transfer of electrons. The slow reduction of ferric HbN to a functional state in the presence of trxB or KshB was accelerated immediately when FdR was added in the midway of the reaction, indicating that HbN has remarkable ability to switch partner from low efficiency reductase to the one having high efficiency for its reduction.

When KshB was integrated at the C-terminus of HbN in an attempt to increase the interactions between heme and FAD binding domain and mimic a flavoHb like structure, the HbN-KshB chimera exhibited complete loss of the activity that was shown when HbN and KshB were free in solution. When FdR was allowed to react with HbN-KshB chimera, it immediately resumed the reduction of ferric HbN. These results suggested that association of HbN with KshB in chimera results in structural conformation that may not be placing the heme and the FAD domains in close contact, thus allowing the reduction of HbN in the HbN-KshB chimera by FdR. In contrast, chimeras of HbN with FdR or reductase domain of *E. coli* HMP exhibited rapid reduction of *Mtb* HbN by forming of Fe-CO adduct very efficiently that behaved like a flavoHb, signifying that the structural geometry of FdR and ferredoxin type reductases has appropriately evolved for intermolecular interactions and smooth transfer of electrons to the heme group.

The present study has also unveiled a novel role of Pre-A motif of HbN, which is required for its optimal NOD function by regulating the protein backbone motion and conformational state of the long tunnel gate to facilitate diffusion of NO towards the active site (16). In the absence of Pre-A motif, the FdR was unable to reduce HbN individually as well as in the HbN-FdR chimera, thereby suggesting involvement of Pre-A in intermolecular ET. The Pre-A region of HbN is highly flexible and makes transient salt-bridges and electrostatic contacts with the protein core (16). The relative movement of the protein backbone changes significantly when Pre-A is removed from HbN. In

particular, previous studies have shown that Pre-A deleted HbN displayed a clear cut restriction in the movement of B and E helices as well as the EF loop region (16), which in conjunction with the CD loop provide key residues involved in the recognition of HbN and FdR. It can, therefore, be concluded that the Pre-A segment influences the NOD function by modulating the dynamics of the protein core, which in turn influences two distinct effect; i) the relative motion between helices B and E favours the conformational changes of the PheE15 gate, thus favouring the transition between closed and open states (15, 16), and ii) the enhanced flexibility of helices B and E must facilitate the interactions between residues that modulate the appropriate recognition at the protein-protein interface. Thus, the results derived from MD simulations reveal the formation of four salt bridges supported by residues located in helix B (Glu25; Glu29) and E (Arg52) as well as loop F (Arg83), which guide the interaction between *Mtb* HbN and FdR. The restricted movement of helices in the Pre-A deleted mutant of *Mt*HbN might have affected the global dynamical motion of the protein matrix and abrogated its interactions with the reductase partner leading to failure of the electron transfer.

The 3D obtained from MD simulations also shows that the CD loop contributes to shape the protein-protein interface near the isoalloxazine ring of the FAD. The CD loop of HbN carries polar residues (Ser46, Thr48 and Asn49) that may participate in building transient contacts with the partner to facilitate ET from the FAD to the heme. At this point, it is worth noting the distance between the propionate of heme to the nearest atom in the isoalloxazine ring remains in the range of 6-9 Å along the last 100 ns of the trajectory, which compares with the distance found between those cofactors in the FlavoHb of *A. eutropus* (around 7 Å). Therefore, the CD loop might afford the intrinsic flexibility to facilitate the adjustment of HbN at the protein-protein interface. In fact, the ET calculations performed for the structures sampled at the end of the trajectory indicate that the electron coupling amounts on average to ca. $3.2x10^{-4} \pm 2.7x10^{-4}$ eV, which compares with the value calculated for the *E. coli* flavoHb ($8.0x10^{-4}$ in oxygenated form). Importantly, the ET is found to be primarily mediated by water molecules, which are present in 71% of the ET pathways, which stresses the relevant contribution of the solvent at the protein-protein interface and the relevance of the polar local environment in assisting the ET between the FAD and the heme. The crucial role of the CD loop is reinforced by the effect of the double mutations at Thr48→Trp/Asn49→Ile of the *Mtb* HbN on the efficiency of electron transfer, which is drastically reduced in the mutant. The inability of FdR to reduce the mutated form of HbN likely arises from the steric hindrance provided by the indol ring of Trp and the apolar long side chain of Ile, which should impede the proper interaction at the protein-protein interface. Inhibition of *Mtb* HbN reduction by FdR in the presence of CD loop peptide further verified that CD loop is playing a crucial role in intermolecular interactions and ET for the recycling of active HbN. At this point, it is worth stressing that the NO oxidation profile of both wild type HbN and the double mutant ($HbN^{Thr49TrpAsn40Ile}$) remained unaffected in the presence of CD loop peptide, thus signifying that CD loop may not be affecting the gating role of PheE15. It can then be concluded that the CD loop has a crucial role in

mediating the reduction step between *Mtb* HbN and FdR.

The present study, thus, unravels a novel mechanism by which HbN interacts with a compatible redox partner to keep itself in the functional ferrous state for the oxygen binding and NO scavenging. Taken together, this work presents three major findings; i) enzymatic reduction of *Mtb* HbN via native and heterologous flavoreductases occurs with varying efficiency and among these, reductases structurally similar to NADH-ferredoxin reductases are most efficient for the ET that may be vital for its oxygen binding and NO-scavenging function, ii) the CD-loop of the HbN play an important role in establishing the transient interactions of *Mtb* HbN with a partner reductase to facilitate the ET, and iii) the Pre-A motif regulates the interactions of CD loop with the partner reductase by modulating the protein dynamics and may be indispensable for the enzymatic reduction of *Mtb* HbN.

REFERENCES

1. Gardner, P. R. (2005) Nitric-oxide dioxygenase function and mechanism of flavohemoglobin, haemoglobin and myoglobin and their associated reductases *J. Inorg. Biochem*. **99**, 247-266
2. Forrester,M. T. and Foster, M. W. (2012) Protection from nitrosative stress : A central role for microbial flavohemoglobin. *Free Radic. Bio. Med*. **52**, 1620-1633
3. Gardner, P. R., Gardner, A. M, Brashear, W. T., Suzuki, T., Hvitved, A. N., Setchell, K. D. and Olson, J. S. (2006) Hemoglobins deoxygenate nitric oxide with high fidelity. *J. Inorg. Biochem.* **100**, 542-550
4. Pathania, R., Navani, N. K., Gardner, A. M., Gardner, P. R., and Dikshit, K. L. (2002) Nitric oxide scavenging and detoxification by the *Mycobacterium tuberculosis* haemoglobin, HbN in Escherichia coli. *Mol Microbiol* **45**, 1303-1314
5. Ouellet, H., Ouellet, Y., Richard, C., Labarre, M., Wittenberg, B., Wittenberg, J., and Guertin, M. (2002) Truncated hemoglobin HbN protects *Mycobacterium bovis* from nitric oxide. *Proc Natl Acad Sci U S A* **99**, 5902-5907
6. Pawaria, S., Rajamohan, G., Gambhir, V., Lama, A., Varshney, G. C., and Dikshit, K. L. (2007) Intracellular growth and survival of *Salmonella enterica serovar* Typhimurium carrying truncated hemoglobins of *Mycobacterium tuberculosis*. *Microb Pathog* **42**, 119-128
7. Hernandez-Urzua, E., Mills, C. E., White, G. P., Contreras-Zentella, M. L., Escamilla, E., Vasudevan, S. G., Membrillo-Hernandez, J. and Poole, R. K. (2003) Flavohemoglobin Hmp, but not its individual domains, confers protection from respiratory inhibition by nitric oxide in *Escherichia coli*. *J Biol Chem*. **278**, 34975-34982
8. Fago, A., Mathews, A. J., Moens, L., Dewilde, S. And Brittain, T. (2006) The reaction of neuroglobin with potential redox protein partners of cytochrome b5 and cytochrome c. *FEBS Letts*. 580, 4884-4888.
9. Eich, R. F., Li, T., Lemon, D. D., Doherty, D. H., Curry, S. R., Aitken, J. F., Mathews, A. J., Johnson, K. A., Smith, R. D., Phillips, G. N., Jr., and Olson, J. S.

(1996) Mechanism of NO-induced oxidation of myoglobin and hemoglobin. *Biochemistry* **35**, 6976-6983
10. Doyle, M. P., and Hoekstra, J. W. (1981) Oxidation of nitrogen oxides by bound dioxygen in hemoproteins. *J Inorg Biochem* **14**, 351-358
11. Milani, M., Pesce, A., Ouellet, Y., Ascenzi, P., Guertin, M., and Bolognesi, M. (2001) *Mycobacterium tuberculosis* hemoglobin N displays a protein tunnel suited for O2 diffusion to the heme. *EMBO J.* **20**, 3902-3909
12. Crespo, A., Marti, M. A., Kalko, S. G., Morreale, A., Orozco, M., Gelpi, J. L., Luque, F. J. and Estrin, D. A. (2005) Theoretical study of the truncated hemoglobin HbN: exploring the molecular basis of NO detoxification mechaism. *J. Am. Chem. Soc.* **127**, 4433-4444.
13. Bidon-Chanal, A., Marti, M. A., Crespo, A., Milani, M., Orozco, M., Bolognesi, M., Luque, F. J. and Estrin, D. A. (2006) Ligand-induced dynamical regulation of NO conversion in *Mycobacterium tuberculosis* truncated hemoglobin-N. *Proteins: Structure, Function, and Bioinformatics* **64**, 457-464
14. Bidon-Chanal, A., Marti, Estrin, D. A. and Luque, F. J. (2007) Dynamical regulation of ligand migration by a gate-opening molecular switch in truncated hemoglobin N from *Mycobacterium tuberculosis*. *J. Am. Chem. Soc.* **129**, 6782-6788.
15. Oliveira, A, Singh, S., Bidon-Chanal, A., Forti, F., Marti, M. A., Boechi, L. Estrin, D. A. Dikshit, K. L. and Luque, F. J. (2012) Role of PheE15 gate in ligand entry and nitric oxide detoxification function of *Mycobacterium tuberculosis* truncated hemoglobin N. *PLoS One*. **7,** e49291
16. Lama, A., Pawaria, S., Bidon-Chanal, A., Anand, A., Gelpi, J. L., Arya, S., Marti, M., Estrin, D. A., Luque, F. J., and Dikshit, K. L. (2009) Role of Pre-A motif in nitric oxide scavenging by truncated hemoglobin, HbN, of *Mycobacterium tuberculosis*. *J Biol Chem* **284**, 14457-14468
17. Hayashi, A., Suzuki, T., and Shin, M. (1973) An enzymic reduction system for metmyoglobin and methemoglobin and its application to functional studies of oxygen carriers. *Biochim. Biophys. Acta* **310**, 300-316.
18. Smagghe, B. J., Trent, J. T.3rd, and Hargroove, M. S. (2008) NO dioxygenase activity in hemoglobins is ubiquitous in vitro, but limited by reduction in vivo. *PLoS One*, **3**., e2039.
19. Appelby, C. A. (1978) Purification of Rhizobium cytochromes P-450. *Methods Enzymol.* **52**, 157-166.
20. Ingelman, M., Bianchi, V., Eklund, H. (1997) The three-dimensional structure of flavodoxin reductase from *Escherichia coli* at 1.7 å resolution. *J. Mol. Biol.* **268**, 147-157
21. Kozakov, D., Hall, D. R., Beglov, D., Brenke, R., Comeau, S. R., Shen, Y., Li, K., Zheng, J., Vakili, P., Paschalidis, I. C. and Vajda, S. (2010) Achieving reliability and high accuracy in automated protein docking: Cluspro, PIPER, SDU, and stability analysis in CAPRI rounds 13–19. *Proteins: Structure, Function, and Bioinformatics*, **78**: 3124–3130
22. Kozakov, D., Brenke, R., Comeau, S. R., Vajda, S. (2006) PIPER: An FFT-based protein docking program with pairwise potentials. *Proteins: Structure, Function, and Bioinformatics*. **65**: 392-406
23. Case, D. A., Darden, T. A., Cheatham III, T. E., Simmerling, C. L., Wang, J., Duke, R. E.., Luo, R., Walker, R. C., Zhang, W., Merz, K. M., Robert, B., Havik, S., Roitberg, A., Seabra, G., Swalis, J., Goetz, A. W., Kolossváry, I., Wong, K. F., Paesani, F., Vanicek, J., Wolf, R. M., . Liu, J., Wu, X., Brozell, S.

R., Steinbrecher, T., Gohlke, H., Cai, Q., X. Ye, X., Wang, J., Hsieh, M. J., Cui, G., D.R. Roe, D. R., Mathews, D. H., Seetin, M. G., Salomon-Ferrer, R., Sagui,, C., V. Babin, V., Luchko, T., Gusarov, S., Kovalenko, A. and P.A. Kollman, P. A. (2012), *AMBER 12*, University of California, San Francisco.

24. Hornak, V., Abel, R., Okur, A., Strockbine, B., Roitberg, A., Simmerling, C., (2006) Comparison of multiple Amber force fields and development of improved protein backbone parameters. *Proteins: Structure, Function, and Bioinformatics*, **65**, 712-725.
25. Capece, L., Boechi, L., Perissinotti, L. L., Arroyo-Mañez, P., Bikiel, D. E., Smulevich, G., Marti, M. A. and Estrin, D. A. (2013) Small ligand-globin interactions: Reviewing lessons derived from computer simulation. *Biochim. Biophys. Acta*. **1834,** 1722-1738.
26. Marti, M. A., Capece, L., Bidon-Chanal, A., Crespo, A., Guallar, V., Luque, F. J. And Estrin, D. A. (2008) NO reactivity with globins as investigated through computer simulation. *Globins and Other Nitric Oxide-Reactive Proteins, Part B* R. K. Poole (Ed.), *Methods Enzymol.* **437***, 477-98*
27. Antony, J.; Medveded, D. M.; Stuchebrukhov, A. A. (2000) Theoretical study of electron transfer between the photolyase catalytic cofactor $FADH^-$ and DNA thymine dimer. *J. Am. Chem. Soc*. **122**, 1057-1065.
28. Bayly, C. I., Cieplak, P., Cornell, W. D. and Kollman, P. A. (1993) A well-behaved electrostatic potential based method using charge restraints for determining atom-centered charges: The RESP model. *J. Phys. Chem.* **97**, 10269-10280.
29. Jorgensen, W. L., Chandrasekhar, J., Madura, J. D., Impey, R. W. and Klein, M. L. (1983) Comparison of simple potential functions for simulating liquid water. *J. Chem. Phys*. **79**, 926-935
30. Ryckaert, J.-P.; Ciccotti, G.; Berendsen, H. J. C. (1977) Numerical integration of the cartesian equations of motion of a system with constraints: Molecular dynamics of n-alkanes. *J. Comput. Phys*. **23**, 327–341
31. Wu, X.; Brooks, B. R. (2003) Self-guided Langevin dynamics simulation method. *Chem. Phys. Lett*. **381**, 512–518.
32. Darden, T., York, D., Pedersen, L. (1993) Particle mesh Ewald: An N.log(N) method for Ewald sums in large systems. *J. Chem. Phys*. **98**, 10089-10092.
33. Beratan, D. N., Onuchic, J. N., Winkler, J. R., Gray, H. B. (1992), Electron-tunneling pathways in proteins. *Science* **258**, 1740–1741.
34. Beratan, D. N., Betts, J. N. Onuchic, J. N. (1991) Protein electron transfer rates are predicted to be set by the bridging secondary and tertiary structure. *Science* **252**, 1285-1288.
35. Alvarez-Paggi, D., Martín, D. F., DeBiase, P. M., Hildebrandt, P., Martí, M. A. and Murgida, D. H. (2010) Molecular basis of coupled protein and electron tranfer dynamics of Cytocrome c in biomimetic complexes. *J. Am. Chem. Soc.* **132**, 5769–5778.
36. Nagai, M., Tomoda, A. And Yoneyama, Y. (1981) Reduction of methemoglobin by ferredoxin and ferredoxin-NADP reductase system. *J. Biol. Chem*. **256,** 9195-9197.
37. Ferreiro, D. N., Boechi, L., Estrín, D. A. and Martí, M. A. (2013) The key role of water in the dioxygenase function of *Escherichia coli* flavohemoglobin. *J. Inorg. Chem*. **119**, 75-84.

38. Brunori, M., Giuffre, A., Nienhaus, K., Nienhaus, G. U., Scandurra, F. M. and Vallone, B. (2005) Neuroglobin, nitric oxide and oxygen functional pathways and conformational changes. *Proc. Natl. Acad. Sci, USA* **102**, 8483-8488.
39. Frey, A. D. and Kallio, P. T (2005) Nitric oxide detoxification- a new era for bacterial globins in biotechnology. *Trends Biotechnol.* **23**, 69-73.
40. Hallstrom, C. K., Gardner, A. M. and Gardner, P. R. (2004) Nitric oxide metabolism in mammalian cells : substrate and inhibitor profiles of a NADPH-cytochrome P450 oxido reductase coupled microsomal nitric oxide dioxygenase. *Free Rad.Biol*. *Med*. **37**, 216-228.

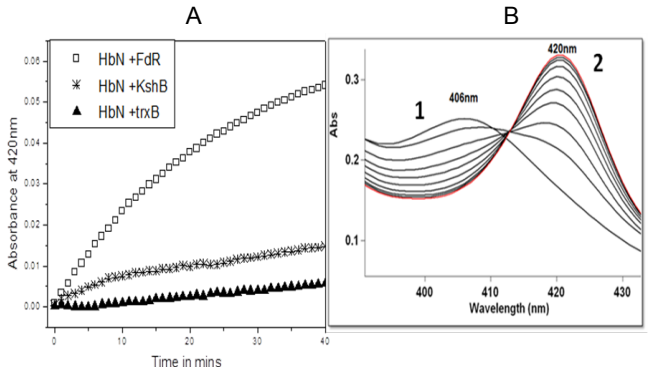

Figure 1: Reduction of oxidised HbN by various reductases. (A) The non linear curves represent the change in the absorbance of soret peak at 420 nm, resulted by the enzymatic reduction of oxidised HbN (8µM) by 1µM of reductases, such as, FdR (open square), Rv3571 (star) and trxB (solid triangle), in the presence of 250µM NADH and CO, with respect to time. (B) This graph represents the shift in absorption maxima of Soret peak of oxidised HbN (8µM) from 406nm (1) to 420nm (2) due to reduction by FdR (1µM) in the presence of 250µM NADH and CO.

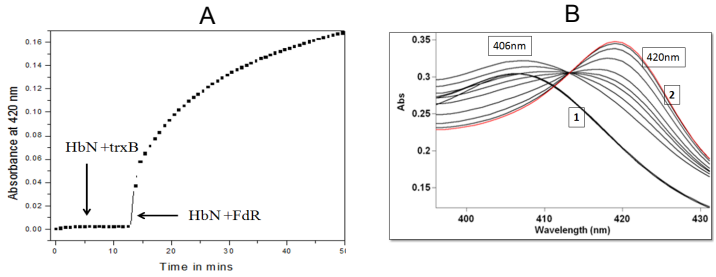

Figure 2:Replacement of low efficient reductase with high efficient one. (A) This graph represents the relative rate of change of Soret peak of oxidized HbN (8µM) at 420nm, with respect to time, due to the reduction by reductases trxB and FdR, where trxB was added at the start of the reaction and FdR was added after the initial 12 mins, in the presence of 250µM NADH and CO. (B)This graph compares the shift in absorption maxima of Soret peak of oxidised HbN (8µM) from 406nm to 420nm due to reduction by 1µM of KshB (1) for initial 12 mins and then by 1µM FdR (2) in the presence of 250µM NADH and CO.

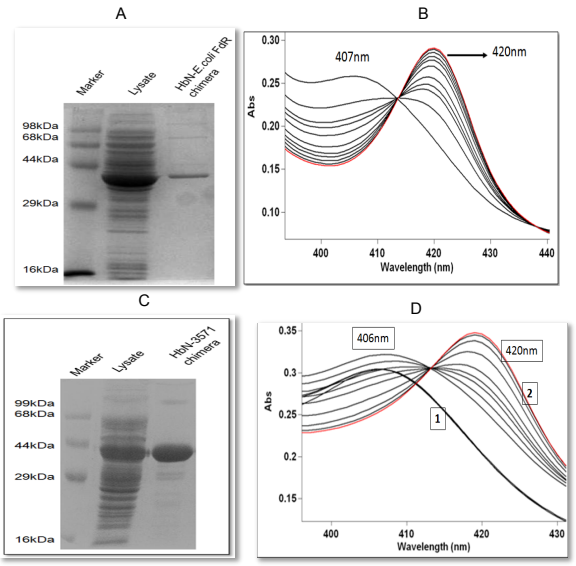

Figure 3: Reduction of HbN-reductase chimera. (A) SDS-PAGE (12.5 0%) profile of the expression and purification of HbN-FdR from *E. coli*. (B) Absorption spectra associated with the auto-reduction of HbN-FdR chimera. (C) SDS-PAGE (12.5 0%) profile of the expression and purification of HbN-KshB chimera from *E. coli*. (D) **1** represents the absorption spectra of the reduction of HbN-KshB chimera only, whereas **2** is obtained after addition of FdR, 10 mins after the start of reaction.

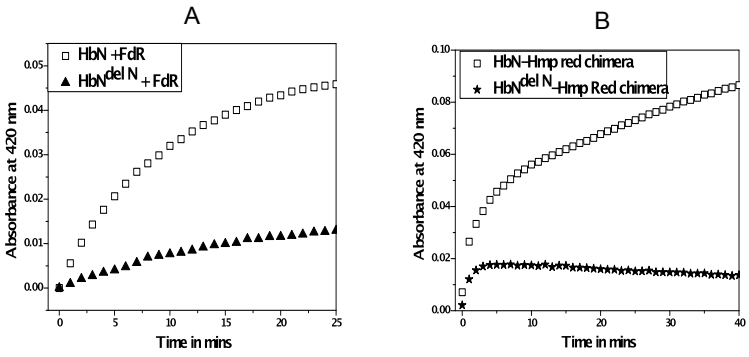

Figure 4: Reduction profile of Pre-A mutant of HbN (A) and HbN chimera (B) by FdR. The graph depicts the efficiency of wild type and mutant HbN reduction as recorded by the increase in the absorbance at 420 nm (Soret peak) due to the formation of CO-adduct after conversion of oxidized HbN into the reduced state of (A) *Mtb* HbN and PreA-deleted HbN, (B) HbN-FdR chimera and pre-A deleted HbN-FdR chimera.

Fig. 5A

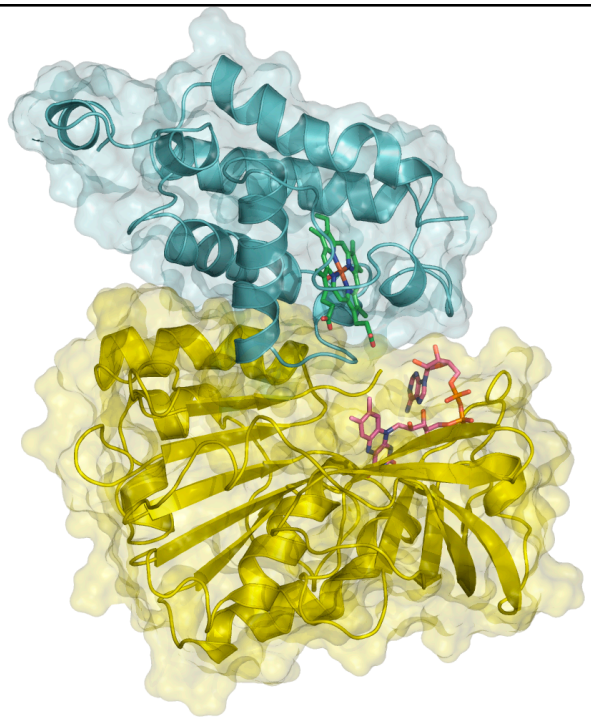

Fig. 5B

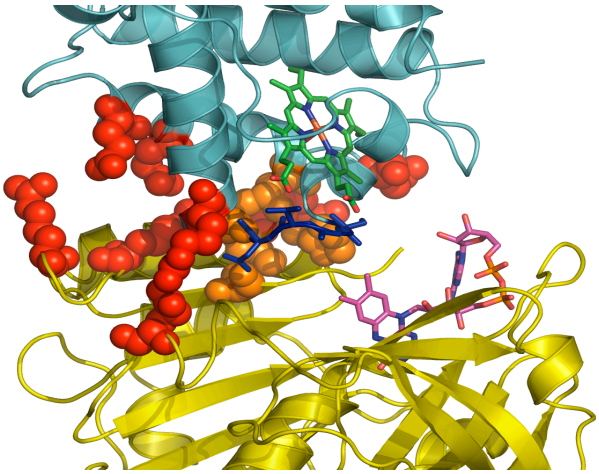

Figure 5: Representative snapshot of the binding interface between MtHbN and FdR. (A) View of the whole complex at the end of the MD trajectory. The backbone of Mtb HbN abd FdR is shown as cyan and yellow cartoon, respectively, and the heme and FAD units are shown as green and magenta sticks**. *(B)*** Detailed view of the interface between HbN and FdR. Residues that participate in salt bridge and hydrophobic contacts between the proteins are shown as red and orange spheres, respectively. The part of the CD loop that partially fills the region between heme and FAD is shown in blue.

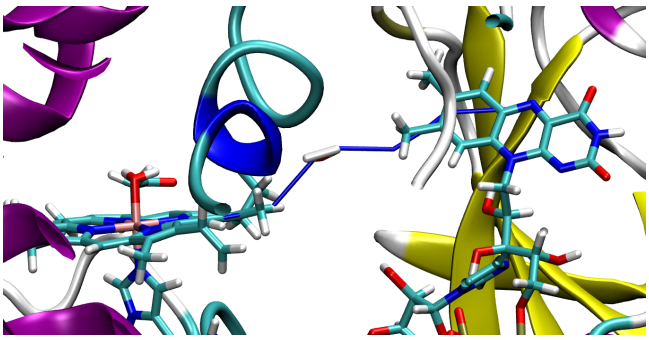

Figure 6: Representation of the most favored electron transfer pathways. The graph shows a representative ET pathway from the isoalloxazine ring of FdR (backbone shown in yellow) to the heme of HbN (backbone shown in magenta) in the process of HbN reduction.

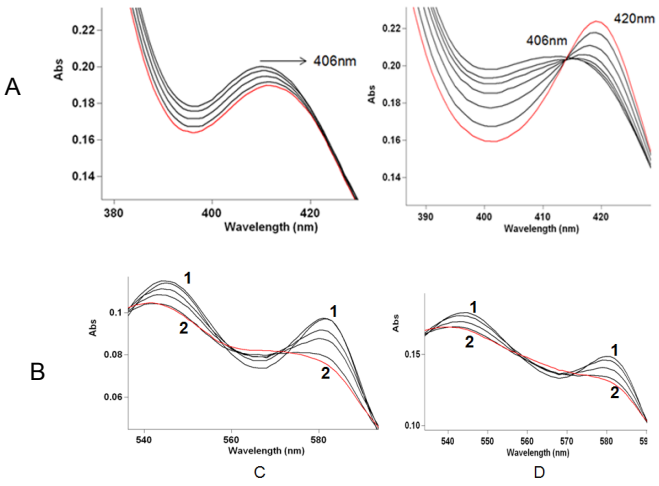

Figure 7: Reduction of oxidised *Mt*HbN by FdR and NO-oxidation in the presence of CD-loop peptide. (A) Reduction of *Mt*HbN in the presence of specific peptide (left panel) and non-specific peptide (right panel) by FdR. (B) NO oxidation profile of *Mt*HbN in the absence (left panel) and presence (right panel) of specific peptide. **1** represents the α and β peaks before the addition of NO and 2 represents α and β peaks after the sequential addition of NO.

Supporting Information

Mechanistic insight into the enzymatic reduction of truncated hemoglobin N of *Mycobacterium tuberculosis*: role of the CD loop and Pre-A motif in electron cycling

Sandeep Singh,[1] Naveen Thakur,[1] Ana Oliveira,[2] Ariel Petruk,[3] Mangesh Dattu Hade,[1] Deepti Sethi,[1] Axel Bidon-Chanal,[2] Marcelo Martí,[3,4] Himani Datta,[1] Raman Prakash,[1] Dario A. Estrin,[3] F. Javier Luque[2] and Kanak L. Dikshit[1]*

[1] CSIR-Institute of Microbial Technology, Sector 39A, Chandigarh 160036, INDIA
[2] Departament de Fisicoquímica and Institut de Biomedicina (IBUB), Facultat de Farmàcia, Universitat de Barcelona, Campus de l'Alimentació Torribera, Santa Coloma de Gramenet, Spain
[3] Departamento de Química Inorgánica, Analítica, y Química Física/INQUIMAE CONICET, Facultad de Ciencias Exactas y Naturales, Universidad de Buenos Aires. Ciudad Universitaria, Pabellon 2, C1428EHA Buenos Aires, Argentina
[4] Departamento de Química Biológica, Facultad de Ciencias Exactas y Naturales, Universidad de Buenos Aires. Ciudad Universitaria, Pabellon 2, C1428EHA Buenos Aires, Argentina

Table S1. Details for the docking results obtained using the balanced ClusPro score (equation: $E = 0.40E_{rep} - 0.40E_{att} + 600E_{elec} + 1.00E_{DARS}$) for the 10 most populated protein-protein complex clusters indicating for each of them the distance between de centers of geometry of the heme group in trHbN and the flavin group in FDR.

Cluster	Members	Representative	Weighted Score	Distance [Å]
0	120	Center	-608.0	18.3
		Lowest Energy	-907.4	
1	117	Center	-606.5	29.6
		Lowest Energy	-761.6	
2	113	Center	-627.5	21.7
		Lowest Energy	-827.5	
3	79	Center	-686.6	34.5
		Lowest Energy	-744.5	
4	71	Center	-584.6	20.5
		Lowest Energy	-703.9	
5	55	Center	-588.3	28.2
		Lowest Energy	-728.5	
6	52	Center	-605	24.2
		Lowest Energy	-640.6	
7	49	Center	-586.5	19.5
		Lowest Energy	-675.8	
8	43	Center	-701.8	41.5
		Lowest Energy	-701.8	
9	34	Center	-607.8	19.4
		Lowest Energy	-668.5	

Figure S1. Representation of the best docked pose obtained for the MtHbN/FdR complex. The backbone of the protein, which is shown as orange cartoon, is superposed to the X-ray structure of flavoHb of *Alcaligenes eutropha* (PDB entry 1CQX), which is shown as yellow cartoon. The heme and flavin cofactors are shown as blue and magenta sticks, respectively.

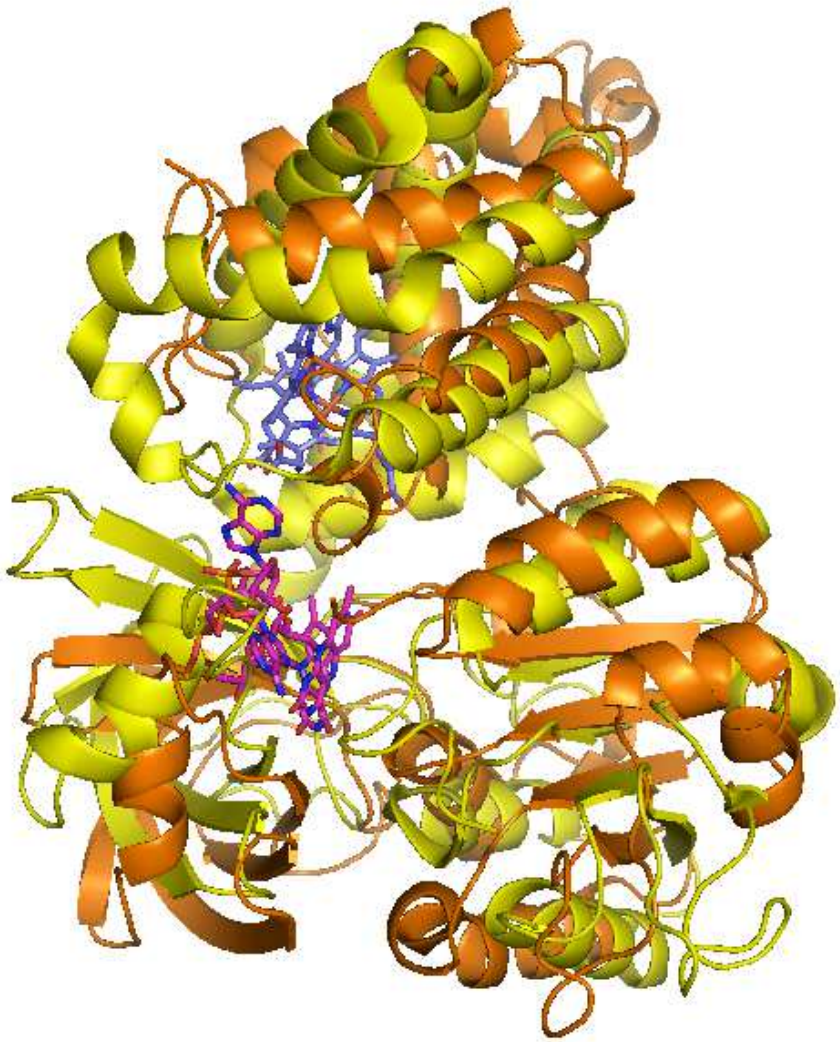

Figure S2. (Top) Time evolution (ns) of the root-mean square deviation (RMSD; Å) determined for the backbone atoms of the HbN-FdR complex. (Middle) Representation of the distance (Å) between the isoalloxazine ring (methyl group at position C8) and one of the heme propionate groups. (C) Time evolution (ns) of the change in the solvent accessible area (SAS; Å^2) for the HbN-FdR complex.

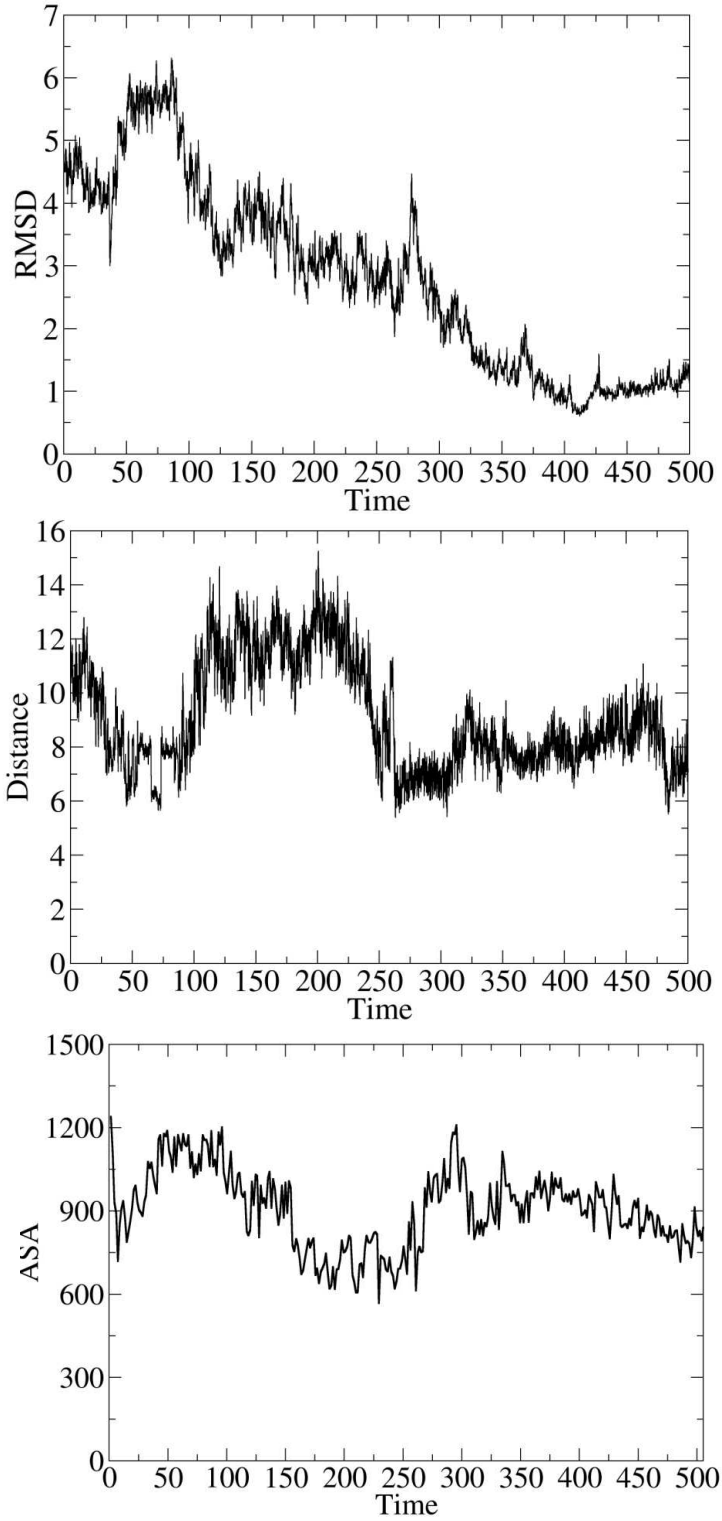

Figure S3. Representation of the MtHbN/FdR complex obtained from the superposition of FdR in the docked solution and at the end of the trajectory. FdR is shown as blue cartoon and the FAD unit as yellow sticks. MtHbN is the docked pose and at the end of the trajectory is shown as white and green cartoon, and the heme is shown as magenta sticks.

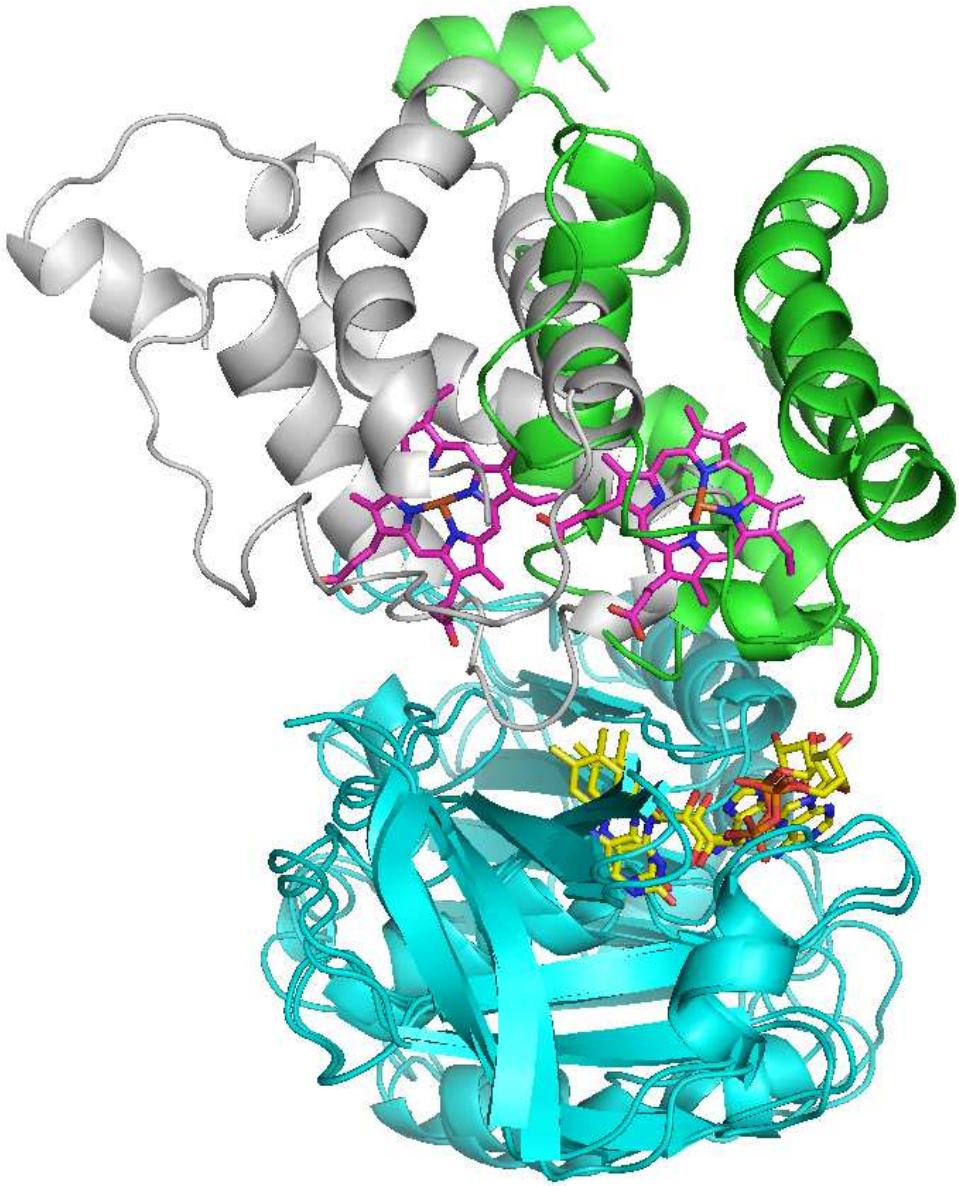

3.1.3 Kinetics and computational studies of ligand migration in nitrophorin 7 and its Δ(1-3) mutant

Nitrophorins (NP) comprise a class of ferriheme proteins that appear in the saliva of the bloodsucking insect *Rhodnius proxilus*. Five isoproteins (NP1-4 and 7) have been identified up to now. The main goal of NPs is to deliver NO into the blood plasma of a host species. This process promotes vasodilatation and anticoagulation, both of which are important for the animal to obtain a sufficient blood meal.

Among the various NPs, we are particularly studying the novel isoform of NP7 because of its unique properties, which include the ability to attach to phospholipid surfaces. NP7 also displays a unique N-terminal, composed of three extra residues with the motif (Gly^1-Pro^2-Leu^3).

Four systems were prepared for the molecular simulations: wild type and a mutated protein generated by deleting the first three residues, treating them in the open and closed conformation that might be devised to represent the situation at high pH and low pH. They are believed to depend on the protonation state of the Asp32 residue, located at the AB loop. In all the performed simulations CO is bound to the ferrous heme porphyrine in order to simulate the system used in experimental flash photolysis experiments.

The aim of this study was not only to understand the influence of the extra three N-terminal residues on the protein dynamical motions but also to compare the overall dynamical behavior of the protein, paying particular attention to the migration pathways. To this end, simulations were performed with two different force fields: parmm99SB as implemented in Amber, and charmm22 with NAMD program.

The results reveal that the dynamical behavior displayed by the protein is not affected by the force field in the same simulation conditions, since the topological protein characteristics are well conserved along the trajectories. On the other hand, no relevant structural differences were observed between the wild type and the Δ(1-3) mutant, suggesting that the two species should have similar behavior regarding the binding/unbinding of ligands.

Simulations detected relevant differences in the loops that connect elements of the global structure of β-barrel due to the protonation of the Asp32 residue. In the open conformation a dramatic deviation between loops AB and GH is found, while in the closed conformation a stable hydrogen bond between the residues Asp32 and Ile132 is established, keeping the two loops together.

The analysis of the internal transient cavities was performed with MdPocket. The results reveal a novel hydrophobic inner tunnel perfectly well defined in the closed

conformation, which connects the distal cavity with the solvent, the last area being shaped by the residues Phe20, Phe21, Val54, Leu77 and Val111. The same tunnel was detected to the open conformation although it emerges with a smaller frequency, when compared to the closed conformation.

In order to check whether NO could diffuse using this pathway, we performed multiple MD simulations with free NO starting on different locations of the tunnel: a) closed to the heme cavity and b) putting the particle on the opposite extreme of the inner tunnel. The results showed three favorable docking sites in the protein matrix: site 1 (located just behind the distal pocket) is the one that lodges more NO molecules and for longer time, followed by site 3 (next to the residue Gly81), whereas the lower occupancy was found for site 2 (located between site 1 and 2).

For the wild type closed conformation, it was found that the ligand may enter and escape from the protein matrix using the same pathway. Similar results were found on the mutated closed protein. The diffusion of the ligand is however more difficult in the open form, which agrees with the lower fluctuations of the residues that delineate the tunnel compared to the closed protein, which experience a higher flexibility.

Of particular interest is the docking site 3 in NP7 at the back of the protein, i.e., opposite the heme hosting cavity, as the back surface of NP7 is characterized by a massive clustering of Lys residues. This leads to the attachment of NP7 to negatively charged cell surfaces, a property that NP1-4 do not have. The current data allow us to speculate that the processes of docking to cell surfaces and NO release may be interconnected, thereby supporting the release of NO into a target cell via site 3. The possibility of NO delivery through protein-membrane interaction resembles an interesting mechanism for NO signaling.

Biochimica et Biophysica Acta 1834 (2013) 1711–1721

Contents lists available at SciVerse ScienceDirect

Biochimica et Biophysica Acta

journal homepage: www.elsevier.com/locate/bbapap

Kinetics and computational studies of ligand migration in nitrophorin 7 and its Δ1–3 mutant☆

Ana Oliveira [a,1], Alessandro Allegri [b,1], Axel Bidon-Chanal [a], Markus Knipp [c], Adrian E. Roitberg [d], Stefania Abbruzzetti [b], Cristiano Viappiani [b,*], F. Javier Luque [a,**]

[a] Departament de Fisicoquímica and Institut de Biomedicina (IBUB), Facultat de Farmàcia, Universitat de Barcelona, Campus de l'Alimentació Torribera, Santa Coloma de Gramenet, Spain
[b] Dipartimento di Fisica e Scienze della Terra, Università degli Studi di Parma, viale G. P. Usberti 7/A, 43124 Parma, Italy
[c] Max Planck Institute for Chemical Energy Conversion, Stiftstrasse 34-36, D-45470 Mülheim an der Ruhr, Germany
[d] Quantum Theory Project and Department of Chemistry, University of Florida, Gainesville, FL 32611-7200 USA

ARTICLE INFO

Article history:
Received 25 January 2013
Received in revised form 25 March 2013
Accepted 11 April 2013
Available online 26 April 2013

Keywords:
Nitrophorin 7
Nitric oxide
Reaction kinetics
Molecular dynamics
Ligand migration

ABSTRACT

Nitrophorins (NPs) are nitric oxide (NO)-carrying heme proteins found in the saliva of the blood-sucking insect *Rhodnius prolixus*. Though NP7 exhibits a large sequence resemblance with other NPs, two major differential features are the ability to interact with negatively charged cell surfaces and the presence of a specific N-terminus composed of three extra residues (Leu1-Pro2-Gly3). The aim of this study is to examine the influence of the N-terminus on the ligand binding, and the topological features of inner cavities in closed and open states of NP7, which can be associated to the protein structure at low and high pH, respectively. Laser flash photolysis measurements of the CO rebinding kinetics to NP7 and its variant NP7(Δ1–3), which lacks the three extra residues at the N-terminus, exhibit a similar pattern and support the existence of a common kinetic mechanism for ligand migration and binding. This is supported by the existence of a common topology of inner cavities, which consists of two docking sites in the heme pocket and a secondary site at the back of the protein. The ligand exchange between these cavities is facilitated by an additional site, which can be transiently occupied by the ligand in NP7, although it is absent in NP4. These features provide a basis to explain the enhanced internal gas hosting capacity found experimentally in NP7 and the absence of ligand rebinding from secondary sites in NP4. The current data allow us to speculate that the processes of docking to cell surfaces and NO release may be interconnected in NP7, thereby efficiently releasing NO into a target cell. This article is part of a Special Issue entitled: Oxygen Binding and Sensing Proteins.

1. Introduction

Nitrophorins (NPs) are nitric oxide (NO)-carrying heme proteins found in the saliva of the blood-sucking insect *Rhodnius prolixus* [1]. At least four NPs (denoted NP1–4) are expressed in the adult animals and were isolated from the salivary glands [2–4]. Another NP (termed NP7) has been recently discovered from a cDNA library and was then recombinantly expressed [5,6]. The major biological function of these proteins is to improve feeding by releasing NO into the host tissue, causing vasodilation and inhibiting blood coagulation [2,7] through a pH-sensitive mechanism. Thus, NPs bind NO in the insect's salivary gland, keeping it stable for long periods of time in the acidic saliva (pH 5–6) by binding to the axial position of the ferriheme center. Upon injection into the tissue of the insect's victim, the protein experiences a significant pH change (to ~7.4 in the blood plasma), which decreases the affinity for NO, leading to NO dissociation and diffusion to nearby capillaries to cause vasodilation. In addition, NPs can efficiently bind histamine, which is released from mast cells at the site of the bite, facilitating the immune response suppression by sequestering histamine during feeding [8,9].

NPs exhibit a lipocalin-type of fold, which consists of an eight-stranded antiparallel β-barrel containing a central cavity that hosts the heme cofactor [10–13]. The heme iron is tethered to the protein via coordination by the His60. The sixth position is free to bind small ligands such as NO, CN^-, NH_3 and histamine [10,14]. It is crucial for the function of the NPs to maintain the heme iron in the oxidation state +3 to keep the NO affinity small enough in order to allow for sufficient release under physiological conditions. This is achieved by electrostatic stabilization and by deformation of the heme cofactor [15,16]. The pH-dependent release of NO is associated with a conformational change that mainly involves loops AB and GH, which shape the heme cavity at the open end of the β-barrel. Such conformational

Abbreviations: NP, nitrophorin; MD, molecular dynamics; RMSD, root-mean square deviation; PS, L-α-phosphatidyl-L-serine

☆ This article is part of a Special Issue entitled: Oxygen Binding and Sensing Proteins.

* Corresponding author.
** Corresponding author. Tel.: +34 934024557.
E-mail addresses: cristiano.viappiani@fis.unipr.it (C. Viappiani), fjluque@ub.edu (F.J. Luque).

[1] These authors have contributed equally to this work.

1570-9639/$ – see front matter © 2013 Elsevier B.V. All rights reserved.
http://dx.doi.org/10.1016/j.bbapap.2013.04.009

change depends on the protonation state of an aspartate residue (Asp30 in NP4; Asp32 in NP7), whose ionization triggers the conformational change between "closed" and "open" states [17–19], which can be associated to the protein structure at low and high pH, respectively [17,20,21]. In the closed conformation of NP4 Asp30 forms a hydrogen bond with the backbone carbonyl group of Leu130 (replaced by Ile132 in NP7), keeping loops AB (Glu32-Trp40 in NP4) and GH (Lys125-Gly131 in NP4) close together. Deprotonation at high pH breaks the hydrogen bond and Asp30 becomes solvent-exposed due to the conformational change of the loops in the open state. The net effect is that NO escape, which is prevented by a significant barrier at low pH, is facilitated upon transition to the open state [19,22]. This pH-dependent mechanism is supported by the structural and kinetic data of the Asp30 → Asn/Ala NP4 mutants solved at low pH, which reveals an open conformation, while kinetic assays show no significant effect of pH on NO association and dissociation for the mutants, in contrast to the wild type (wt) protein [23].

Sequence alignment points out that NP7 exhibits a large resemblance with other NPs, as noted in sequence identities of 62% and 42% with NP2 and NP4 from *R. prolixus* (77% and 60% of positive residues, respectively; see Fig. S1 in the Supporting information). However, NP7 is especially interesting since it encompasses two major differential features compared to other NPs. First, whereas NP1–4 remain in solution and can diffuse away from the feeding site while releasing NO over a larger area, NP7 binds to L-α-phosphatidyl-L-serine (PS) containing phospholipid membranes [5,6]. Thus, NP7 may recognize PS-bearing membranes and might therefore target the surfaces of activated platelets and degranulating mast cells, where accumulation of PS in the outer surface is an indicator of hemostatic activity [24,25]. In line with these properties, the isoelectric point (*pI*) of the mature NP7 (i.e., without the signaling segment that regulates export to the salivary gland lumen) is estimated to be around 3 units higher than the *pI* values of NP1–4 (varying from 6.1 to 6.5) [26].

Another major distinctive feature is that NP7 contains three extra residues (Leu1-Pro2-Gly3) at the N-terminus [27]. While this additional stretch might a priori seem to have a negligible role, the biochemical data reveal an unexpected effect on the thermodynamic and kinetic parameters of NO binding to NP7. Deletion of the extra residues increases the equilibrium constant (K_{eq}) for NO binding to NP7 by ~2 orders of magnitude at high pH (7.5), while a 10-fold reduction in K_{eq} is observed at low pH (5.5) [26]. In addition, while the NO dissociation rate constant (k_{off}) of wt NP7 and NP7(Δ1–3) are very similar, at pH 7.5 the NO association rate constant (k_{on}) for NP7(Δ1–3) is approximately 250-fold larger than for wt NP7. Compared to wt NP7, the structural arrangement at the N-terminus of NP7(Δ1–3) is expected to be more similar to the experimentally and computationally extensively studied NP4. However, k_{on}(NO) of NP4 at pH 7.5 is comparable to that of wt NP7 [26]. Thus, clarification about the role of the NP7 N-terminus is needed. Also, the iron reduction potential (Fe(II/III)) increases significantly upon excision of the N-terminal tripeptide, i.e., from $E^{\circ} = -268$ mV (wt NP7) to -109 mV (NP7(Δ1–3)) vs. standard hydrogen electrode at pH 5.5, making the protein susceptible to reduction by excess NO. These findings suggest that the unique N-terminal sequence may be important for modulating the biological function of NP7.

Although the main biological role of NPs is the transport and delivery of NO, the differential trends of NP7 and their impact on the structure–function relationships remain to be completely understood. Thus, recent studies have highlighted significant differences in the kinetics of CO association and dissociation to NP4 and NP7 [28]. In particular, the results suggest the existence of a larger number of docking sites in NP7, so that the photodissociated CO appears to sample the protein interior for longer times. Unfortunately, for NP7 an experimental structure is still missing, which makes it difficult to provide a structural interpretation to the kinetic data. The aim of this study is twofold. First, we want to examine the influence of the extra residues at the N-terminus of the protein on the ligand association/dissociation properties. Second, we want to study the structural and dynamical properties of the "closed" and "open" states of wt NP7, which can be viewed as representative states at both low and high pH, respectively, and to calibrate their impact on the ligand migration through the protein interior. To this end, we report here kinetic measurements of the CO rebinding kinetics to NP7(Δ1–3) mutant, which lacks the three extra residues at the N-terminus, at low and high pH. The results will be compared with the data reported previously for the wt protein [28]. In addition, we report extensive molecular dynamics (MD) simulations of NP7 with the aim of providing structural models that might useful to interpret the ligand migration properties and to shed light into the structure–function relationships of this protein.

2. Materials and methods

2.1. Protein samples for kinetic studies

In order to determine the effect of the extra residues at the N-terminus on the kinetics of ligand (CO) association/dissociation, two protein variants were examined. The first corresponds to a mutant of the mature NP7 protein where residues Leu1-Pro2-Gly3 are eliminated (denoted NP7(Δ1–3); see above). The second is a variant that also lacks the first three extra residues at the N-terminus, but retains the start-Met residue that initiates the transcription of the cDNA during recombinant expression. This latter variant will hereafter be designated Met-NP7(Δ1–3).

Met-NP7(Δ1–3) was recombinantly expressed in *Escherichia coli* strain BL21 (DE3) (Novagen) and reconstituted as was previously described [6,11]. The production of NP7(Δ1–3) was performed by a method where the protein is recombinantly expressed as a fusion with the *E. coli* leader sequence pelB similarly to the method described for NP2 [29]. However, because the protein was found strongly attached to negatively charged cell components in the *E. coli* homogenate, particularly DNA, the purification method had to be revised. To detach the protein from the homogenate pellet, the protein was unfolded and then refolded similar to the expression of Met-NP7(Δ1–3) [6,11].[2] The purity and integrity of the protein preparations were routinely controlled by SDS-PAGE, MALDI Q-TOF MS, and UV/vis absorbance spectroscopy.

2.2. Nanosecond laser-flash photolysis experiments

Laser-flash photolysis assays were performed for the ferroheme–CO complex of wt and mutated proteins. This choice is justified by the fact that the ferroheme–CO complex of NP7 has been used as an isoelectronic model for the ferriheme–NO complex, as explained in detail in Ref. [28]. Thus, both complexes exhibit similar ligand-heme geometries, *i.e.*, ∠(Fe–X–O) ~ 180° (X = C, N). Furthermore, in both cases a neutral diatomic gas molecule is released from the cofactor upon laser-flash photolysis. The advantage of CO as a ligand is that the binding kinetics is slower than for NO and thus kinetic investigations are facilitated. Let us note that the focus of this study is on the interaction of the gas ligand with the protein matrix rather than the formation/breakage of the Fe–XO bond, which must be different due to the distinct electronic configurations of both metal and ligand in Fe(III)/NO and Fe(II)/CO. Nevertheless, the close resemblance in size (bond length of 115 and 113 pm for NO and CO, respectively) and polarity (dipole moment of 0.159 and 0.110 D for NO and CO, respectively) of the two gaseous molecules suggests similar interactions with the protein matrix. Therefore, CO can serve as a good model for NO in its interaction with the protein and with respect to the geometry of the metal complex, which are the two important parameters in this study.

[2] Details of the procedure will be published elsewhere. (J.J. Taing, M. Knipp, private communication).

The experimental setup was described in detail elsewhere [30]. Photolysis of CO complexes was obtained using the second harmonic (532 nm) of a Q-switched Nd:YAG laser (Surelite, II-10, Continuum, Santa Clara, CA). The cw output of a 75 W Xe arc lamp was used as probe beam, a 5 stage photomultiplier (Applied Photophysics) for detection and a digital oscilloscope (LeCroy LT374, 500 MHz, 4 GS s^{-1}) for digitizing the voltage signal. A spectrograph (MS257 Lot-Oriel) was used to select the monitoring wavelength (436 nm) and to remove the residual stray light from the pump laser. The temperature of the sample holder was accurately controlled with a Peltier element, allowing a temperature stability of better than 0.1 °C. Experiments were performed at 20 °C.

Time-resolved difference absorbance spectra were measured using a gated intensified CCD (Andor Technology, iStar, 1024 × 1024 pixels used in full vertical binning mode), coupled to the spectrograph. Time-resolved spectra consist of photoproduct minus NP − CO difference spectra at 80 logarithmically spaced time delays following photodissociation, from 10 ns after the laser flash to 10 ms. Spectra are obtained by averaging 100 single shot signals at each delay. The overall time resolution of the setup is limited by the laser pulse width (~10 ns).

Samples were prepared by equilibrating the solutions in a sealed 1 cm-quartz cuvette connected to a tonometer with 0.1 or 1 atm CO. Stock solutions of $Na_2S_2O_4$ were prepared freshly before use. $Na_2S_2O_4$ was then titrated anaerobically into the solution while formation of the CO adduct was monitored by absorption spectroscopy. Inclusion of 1 mM of L-cysteine in the solution significantly improved the sample stability during experiments. The solubility of CO in water is such that its concentration is 1.05 mM at 10 °C when the solution is equilibrated with 1 atm CO. The temperature dependence of CO solubility [31] was taken into account in the analysis. The numerical analysis of the rebinding kinetics was described in detail previously [32]. The coupled differential equations associated with reaction Scheme 1 were solved numerically and the rate constants were optimized to obtain a best fit to the experimental data. Numerical solutions were determined by using the function ODE15s within Matlab 7.0 (The MathWorks, Inc.). Fitting of the numerical solution to the experimental data (and optimization of microscopic rate constants) was obtained with a Matlab version of the optimization package Minuit (CERN).

2.3. Set-up of the model systems for molecular dynamics simulations

The initial structures of the wt NP7 and its NP7(Δ1–3) mutant were built up by homology modeling using SwissModel [33] with the X-ray crystallographic structures of NO bound NP4 at pH 5.6 (PDB ID: 1X8O; resolution of 1.0 Å) and at pH 7.4 (PDB ID: 1X8N; resolution of 1.1 Å) [17] as templates. These structures were chosen because the conformations of the AB and GH loops are characteristic of the closed and open states, respectively. Due to the larger sequence identity with NP2, an alternative model for NP7 was also built up using the X-ray structure of NP2 at pH 7.5 (PDB ID: 1T68; resolution of 1.5 Å) [12,34] as template, but no relevant difference was found compared to the NP4-based model.

Standard ionization states were assigned to all the residues with the only exception of Asp32, which was protonated at low pH and ionized at high pH on the basis of previous studies [20–23]. Because all four Cys in the native NPs form disulfide bridges [35] in the computational model the two native disulfide bridges were also imposed between residues Cys5 and Cys124 and between Cys42 and Cys173. Finally, the heme was modeled in the so called **A** orientation (see Fig. S2 in the Supporting information), where the pyrrole ring II is placed above the protein backbone atoms of His60, which was demonstrated to be the thermodynamically favored orientation for both NP7 and Met-NP7(Δ1–3) by NMR spectroscopy [26,36]. Note that this orientation has been modeled in the NP4 structures PDB ID: 1X8O and PDB ID: 1X8N, although NMR spectroscopy reveals that the heme orientation appears in a ~1:1 equilibrium. In contrast, the **B** isomer is favored in NP2 [12,37].

2.4. Molecular dynamics simulations

The structural and dynamical properties of NP7 and NP7(Δ1–3) were studied using extended molecular dynamics (MD) simulations. Simulations have been performed for the CO-liganded protein in correspondence with the photolysis assays. This obeys the fact that, immediately after photolysis, the ligand experiences an unrelaxed protein structure, which is better approximated by the liganded structure, and only after some time the relevant structure becomes the ligand-free one. Thus, the nanosecond rebinding phase is expected to sense a structure similar to the liganded one.

Due to the lack of a crystallographic structure for NP7, the refinement of the models and the consistency of the structural and flexibility properties were examined by running several independent simulations and force fields. First, the wt NP7 in both open and closed states was simulated in duplicate, each simulation covering between 130 and 150 ns, using the parmm99SB force field [38] and the Amber-11 package [39]. In the following these simulations will be denoted Open_1, Open_2, Closed_1 and Closed_2. Then, the snapshot taken at 50 ns in the first simulation (Open_1 and Closed_1) was used to start an independent simulation for the open and closed states using the charmm22 [40] force field and the NAMD program [41]. In addition, they were used as starting models to build up the NP7(Δ1–3) systems. In all cases the protein was simulated with CO bound to the ferrous heme (see above). The heme-bound CO parameters used in Amber simulations were developed in previous works [42].

The protein was immersed in a preequilibrated cubic box (~70 Å per side) of TIP3P [43] water molecules. The SHAKE algorithm [44] was used to keep bonds involving hydrogen atoms at their equilibrium length, in conjunction with a 1 fs time step for the integration of the Newton's equations. Trajectories were collected in the NPT (1 atm, 300 K) ensemble using periodic boundary conditions and Ewald sums (grid spacing of 1 Å) for long-range electrostatic interactions [45]. The systems were minimized using a multistep protocol, involving first the adjustment of hydrogens, then the refinement of water molecules, and finally the minimization of the whole system. The equilibration was performed by heating from 100 to 298 K in four 200-ps steps at constant volume, followed by 200 ps of MD at

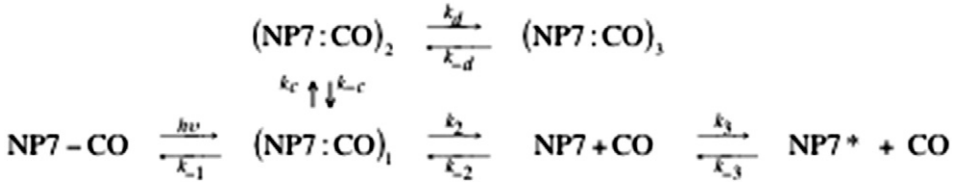

Scheme 1. Minimal reaction scheme for the observed CO rebinding kinetics to NP7 solutions. $(NP7:CO)_1$ indicates the primary docking site with CO inside the distal pocket, while $(NP7:CO)_2$ and $(NP7:CO)_3$ represent reaction intermediates with CO in temporary docking sites, sequentially accessible from the distal site. Relaxation of the structure to an unliganded state NP7* is added to account for the presence of a long lived (unreactive, or very slowly reacting) reaction intermediate.

constant pressure and temperature. Once the system was equilibrated, the different production MD runs were performed. Frames were collected at 1 ps intervals, which were subsequently used to analyze the trajectories.

2.5. Ligand migration pathways

The preferred docking sites and migration pathways were identified using MDpocket [46], which uses a fast geometrical algorithm based on a Voronoi tessellation centered on the atoms and the associated alpha spheres to characterize pockets and channels [47]. A grid that encloses all the superposed snapshots is generated and for every snapshot each alpha sphere is assigned to the closest grid point. The number of counted alpha spheres assigned to each grid point is then normalized by the total number of snapshots. This generates a frequency map ( ) that allows the visualization of pockets during the MD trajectory, indicating whether a given point is permanently accessible (= 1), hindered (= 0) or transiently accessible (0 < < 1). Analyses were performed using 5000 snapshots taken equally spread over the last 50 ns of the trajectories. The minimum and maximum alpha sphere radii were 2.8 Å and 5.5 Å, respectively. The identified cavities were superposed in time and space and a density map was generated from this superposition. Stable cavities are identified as high-density 3D isocontours, while low-density isocontours denote transient or nearly non-existent cavities in the MD simulation.

To complement the structural information derived from MDPocket analysis, implicit ligand sampling (ILS) calculations [48] were performed to determine the energetics of ligand migration through the protein matrix, as this technique has been valuable to identify gas migration pathways inside proteins [49–53]. To this end, a set of 5000 snapshots was taken from every trajectory and enclosed in a grid (0.5 Å spacing) used to place a probe NO molecule. The size of the grid was chosen to fully enclose the protein core and the space corresponding to the layer of surrounding solvent molecules. The parameters for the NO molecule were adapted from Cohen et al. [49]. 20 orientations of the NO molecule were considered to determine the free energy at each grid point. For each trajectory ILS calculations were performed for the time periods 60–80 ns and 80–100 ns, and the analysis reported the same energetics for the two time windows, thus supporting the structural equilibration of the cavities in the interior of the protein.

3. Results

3.1. Kinetics of CO rebinding

Although the NO association/dissociation process is biologically relevant, the slower CO association reaction facilitates the observation of the rebinding kinetics. The kinetics of CO rebinding after nanosecond laser flash photolysis for wt NP7 was reported in an earlier study [28]. The results showed a very fast nanosecond geminate recombination phase, a large fraction of which fell within the instrumental dead time. The associated lifetime distributions displayed a prominent geminate rebinding at ~10 ns. A heterogeneous bimolecular phase was observed and the broadening was more pronounced at neutral pH. The binding rate of the bimolecular phase was found to increase at low pH. On the microsecond time scale, several bands were found, some of which were being dependent on CO concentration. Remarkably, bands that peaked at ~100 ns and ~10 μs in the lifetime distributions were indicative of CO rebinding from temporary sites inside the protein matrix. Finally, a long-lived reaction intermediate was found at 1 ms, which might indicate the formation of a slow rebinding species upon relaxation of NP7 to less reactive states.

For the experimental investigation of the influence of the unique N-terminus of NP7 on the CO rebinding kinetics, the previously reported mutant NP7(Δ1–3) should be considered [26]. However, the polypeptide expressed according to standard methods has an initial Met0 residue, i.e., Met-NP7(Δ1–3), as a consequence of the ATG start codon required for gene transcription, which may influence the CO binding/rebinding properties. Therefore, a strategy was developed to prepare a form without Met0, i.e., NP7(Δ1–3). MALDI Q-TOF MS was used to confirm the correct amino acid sequence of the recombinant protein. Upon reconstitution with the heme cofactor, the absorbance spectrum was found identical to that of Met-NP7(Δ1–3).

The CO rebinding kinetics measured in this work for the protein variants NP7(Δ1–3) and Met-NP7(Δ1–3) are essentially identical (Fig. 1; see also Fig. S3 in the Supporting information), especially keeping in mind that some tiny differences in the bimolecular phase (i.e., slower in NP7(Δ1–3) at pH 7.5 and in Met-NP7(Δ1–3) at pH 5.5) may simply arise from unavoidable uncertainties in the CO concentration. On the other hand, most of the trends reported for the CO rebinding kinetics of wt NP7 are retained in both NP7(Δ1–3) and Met-NP7(Δ1–3) (Fig. 2). Only two subtle differences can be found. First, the effect of deleting the first three residues on the rebinding kinetics seems to be pH-dependent. At pH 7.5 the nanosecond geminate phase is very similar in wt NP7 and its mutants, whereas the bimolecular rebinding phase is slower in NP7(Δ1–3) and Met-NP7(Δ1–3). At pH 5.5 the geminate phase is smaller in wt NP7, but the bimolecular rebinding phase is more similar to the one observed in the mutants. Second, even though the bimolecular phase is biphasic, the Singular Value Decomposition (SVD) analysis of time-resolved spectra, measured following photodissociation of the CO-bound protein, showed that there is only one significant component for both NP7(Δ1–3) and Met-NP7(Δ1–3). In contrast, a small, yet appreciable second spectral component was found in wt NP7, suggesting relaxation of NP7 to a structure with a distinct spectrum on the microsecond time scale, which then follows back relaxation to the liganded structure as CO is rebound. A negligible second component could mean that the conformational relaxation is not so relevant as in wt NP7, or that the conformational relaxation is present but it is not associated to a spectral change.

The rebinding kinetics to wt NP7 has been interpreted utilizing the reaction mechanism shown in Scheme 1. This model can describe the rebinding kinetics to NP7(Δ1–3) and Met-NP7(Δ1–3) under all tested experimental conditions (see Fig. S4 in the Supporting information). The resulting microscopic rates are summarized in Table 1. The rate constants for NP7(Δ1–3) and Met-NP7(Δ1–3) are very similar to

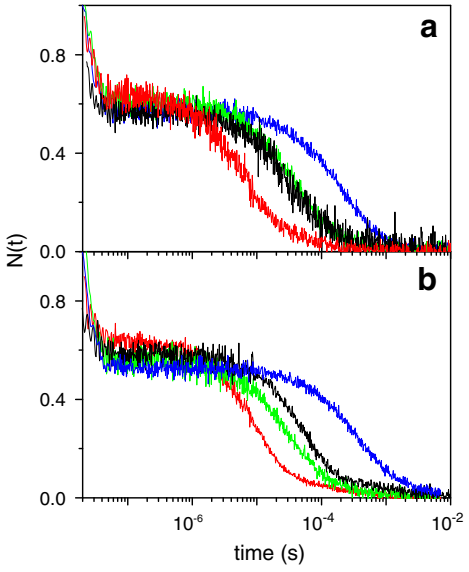

Fig. 1. CO rebinding kinetics (recorded at 436 nm) to (a) NP7(Δ1–3) and (b) Met-NP7(Δ1–3) at T = 20 °C. Data taken at pH = 7.5 (blue, 0.1 atm CO; green, 1 atm CO) and at pH = 5.5 (black, 0.1 atm CO; red, 1 atm CO).

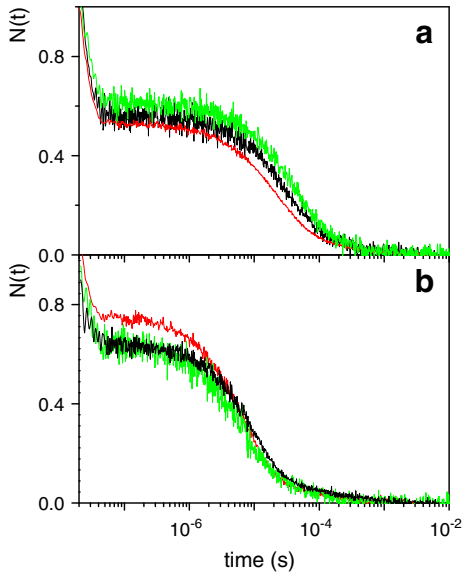

Fig. 2. Comparison between CO rebinding kinetics (recorded at 436 nm) to wild type NP7 (red), NP7(Δ1–3) (black) and Met-NP7(Δ1–3) (green) at 20 °C, 1 atm CO at (a) pH 7.5 and (b) pH 5.5.

the values determined for wt NP7, generally differing by a factor less than 2. Keeping in mind the uncertainties due to the very fast geminate rebinding and CO concentration (see above), these results suggest that the inner cavities are not drastically affected by deletion of the extra residues at the N-terminus. On the other hand, there is a slight decrease in k_{-2} at neutral pH and an increase of k_2 at acidic pH. These changes explain the slowing down in the bimolecular binding rate constant to the mutants at neutral pH, as the k_{on}(CO) values at pH 5.5 are 1.6×10^8, 1.3×10^8 and 0.91×10^8 M^{-1} s^{-1} for wt NP7, NP7(Δ1–3) and Met-NP7(Δ1–3), respectively, whereas the corresponding values at pH 7.5 are 5×10^7, 2.5×10^7 and 2.7×10^7 M^{-1} s^1. The small (3-to-5-fold) increase in k_{on}(CO) upon lowering the pH from 7.5 to 5.5 contributes to the increase of the equilibrium binding constant of CO, and remains within the expected response of the ligand affinity to the pH. Nevertheless, since NP7 rebinds photodissociated ligands very quickly, and in fact a substantial fraction of the ligands has already reacted with the heme at the end of the nanosecond laser pulse, caution is required to not overemphasize the significance of these subtle differences, as the rates k_{-1} and k_2 are affected by systematic errors due to the lack of time resolution of the nanosecond photolysis experiments.

The experimental results obtained in this study suggest that the influence of the NP7 specific N-terminus for the CO association process is negligible. This is, however, contradicting the previous report where k_{on}(NO) for binding to ferric NP7 was estimated to increase ~250-fold upon deletion of the Leu1-Pro2-Gly3 peptide [26]. However, in the previous study k_{on}(NO) was calculated as K_{eq}(NO) × k_{off}(NO). Because the values of k_{off}(NO) are very similar (0.606 and 0.50 s^{-1} for wt NP7 and Met-NP7(Δ1–3), respectively), it is clear that the difference in k_{on}(NO) is due to the difference in K_{eq}(NO). k_{off}(NO) was determined by the replacement of NO with excess imidazole. In an extensive investigation of the NO association and dissociation kinetic parameters of NP1–4, it was already noticed that the dissociation rates obtained with laser-flash photolysis and through a ligand displacement process can differ by a factor of as much as ~10^3 (NP2 at pH 5.0), which suggests that in the displacement event additional interactions between protein and ligand and/or structural relaxation processes may play a role at longer time range [22]. Though this is currently not understood, it suggests that k_{off}(NO) values determined for NP7 may not reflect the simple bimolecular NO dissociation reaction. Moreover, different behavior of NO compared to CO association cannot be excluded, which might, at least in part, reflect a contribution from the binding of water to the unliganded ferric NP7.

3.2. Structural analysis of NP7

The structural comparison between the energy-minimized average structures of wt NP7 is shown in Table 2, which displays the positional root-mean square deviation (RMSD) between the backbone atoms. The RMSD between the closed structures varies from 1.26 to 1.84 Å, which indicates the existence of only moderate differences in the overall conformation of the protein backbone irrespective of the force field (parm99SB versus charmm22). In contrast, larger RMSDs are obtained for the open state, as the RMSD ranges from 1.76 to 2.66 Å. The structural differences between the open forms primarily stem from the extra residues Leu1-Pro2-Gly3 and loops AB and GH, whose conformation is drastically altered along the trajectories (see Fig. 3a). Exclusion of these residues leads to a significant reduction in the RMSD, which ranges from 1.14 to 1.53 Å. In contrast, only a slight decrease in the RMSD is found upon exclusion of the same set of residues for the closed structures (the RMSD varies from 1.05 to 1.45 Å).

These results point out that the overall conformation of the β-barrel is well preserved along the trajectories run for either open or closed states. In fact, the impact of the force field on the β-barrel is lower than the effect associated with the transition between open and closed states, as the cross RMSD varies from 1.43 to 2.11 Å after exclusion of the most flexible regions (see Table 2). This reflects the stability afforded by the hydrogen bond between Asp32 and Ile132 at low pH (the average distance between the carbonyl oxygen of Ile132 and the protonated oxygen of Asp32 is in the range 2.8–3.0 Å), which restricts the conformational flexibility of NP7, as

Table 1
Rate constants for CO rebinding kinetics to wild type NP7 and its NP7(Δ1–3) and Met-NP7(Δ1–3) at 20 °C. Numerical error bars are typically between 10 and 20%.

	NP7[a]		NP7(Δ1–3)		Met-NP7(Δ1–3)	
	pH 7.5	pH 5.5	pH 7.5	pH 5.5	pH 7.5	pH 5.5
k_{-1} (10^7 s^{-1})	6.9	6	3.7	6	6.9	6.1
k_2 (10^7 s^{-1})	6.5	10	5.2	13	8.0	16
k_{-2} (10^7 $M^{-1}s^{-1}$)	9.7	42.8	6	42	5.9	33
k_3 (10^3 s^{-1})	2.6	0.9	2.6	1.7	2.7	0.97
k_{-3} (10^3 s^{-1})	3	2.3	0.5	0.5	1.6	0.1
k_c (10^6 s^{-1})	8.4	6.2	8.4	8.2	7.1	6.2
k_{-c} (10^6 s^{-1})	3	3.1	3	3.1	2.9	3.1
k_d (10^6 s^{-1})	0.88	0.85	0.88	1.6	0.96	6.5
k_{-d} (10^3 s^{-1})	7.5	9.3	7.5	4.6	4.7	8.0

[a] Data from Ref. [28].

Table 2
RMSD (Å) between the backbone atoms of the energy-minimized average structures extracted from the trajectories. The average structure was derived from the snapshots sampled in the last 10 ns of the MD simulations. In addition, the RMSD values were computed by excluding the first three residues of the protein, as well the loops AB and GH (in italics).

	Open_2 (Amber)	Open (Charmm)	Closed_1 (Amber)	Closed_2 (Amber)	Closed (Charmm)
Open_1 (Amber)	2.40	1.76	2.63	2.72	2.88
	1.44	*1.14*	*1.98*	*1.43*	*2.11*
Open_2 (Amber)		2.66	2.16	2.28	2.55
		1.53	*1.53*	*1.43*	*1.66*
Open (Charmm)			2.81	2.99	2.81
			1.83	*1.85*	*1.83*
Closed_1 (Amber)				1.26	1.44
				1.05	*1.19*
Closed_2 (Amber)					1.81
					1.45

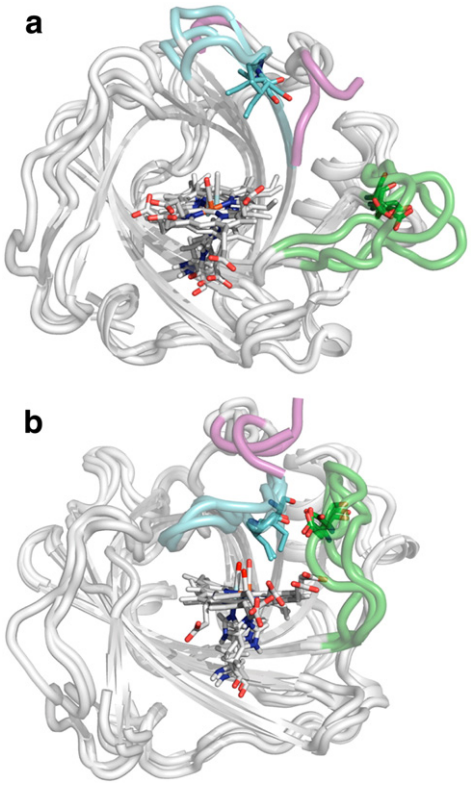

Fig. 3. Superposition of the energy-minimized average structures derived from Amber and Charmm simulations of wild type NP7 in (a) open and (b) closed states. The regions corresponding to the first three residues at the N-terminus, loop AB and loop GH are shown as magenta, green and blue, respectively. The CO-bound ferriheme, the proximal histidine (His60) and the residues involved in hydrogen bonding in the closed state, Asp32 and Ile132, are shown as colored sticks.

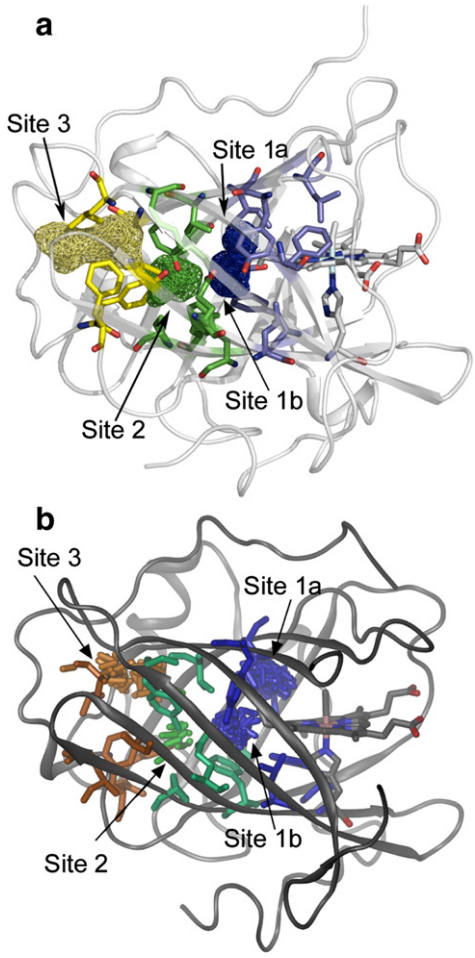

Fig. 4. (a) Representation of the three cavities identified by MDpocket analysis for the closed state of wild type NP7. The regions enclosed by the isocontour value of 0.5 in the frequency map are utilized to represent the inner cavities. The residues that shape the different docking sites are represented as colored sticks. (b) Distribution of the positions sampled by NO in the simulations run with free ligand through the interior of the protein.

noted in the resemblance of the protein backbone, including loops AB and GH, in the superposed structures shown in Fig. 3b.

3.3. Inner cavities in NP7

Recent kinetic studies have shown that in NP7 the photodissociated CO appears to sample the protein interior for longer times than in NP4 [28]. In order to gain insight into the structural interpretation of the kinetic data, MDpocket was used to identify the topology of inner cavities in wt NP7.

Three areas can be found in the interior of the protein for both open and closed states of NP7 (denoted 1–3 in Fig. 4a). The cavities are primarily shaped by hydrophobic residues. The first area, which includes two separate docking sites (1a and 1b), is defined by the inner edge of the heme and by residues Phe43, Leu58, Phe88, Tyr105, Tyr107, Ile123, Leu125 and Ser137. The middle area contains a smaller cavity (site 2) and is shaped by residues Phe20, Phe45, Pro47, Glu56, Tyr84, Val109, Ile121 and Leu139. Note that the polar nature of residue Glu56 is counterbalanced by the formation of strong hydrogen bonds with the hydroxyl groups of Tyr84 and Tyr107 (average distances of 2.6 Å). These interactions should therefore annihilate the polarity of these residues, as reported for other complexes [48]. Finally, the innermost area (site 3) is delineated by residues Phe20, Phe21, Val54, Leu77 and Val111.

The topology of the inner cavities is not affected by the force field used in simulations. This is reflected in Table 3, which reports the similarity between the frequency maps measured using Tanimoto's index as a distance metric [54] (identical trends were found using Carbo's similarity index [55]; data not shown). For the open state the similarity index lies in the range 0.71–0.81, whereas a slightly larger similarity is obtained for closed species (the similarity index varies from 0.71 to 0.90). This agrees with the structural resemblance of the β-barrel found in the simulations run for either open or closed states (see above). The cross similarity between the frequency maps for open and closed structures is lower, ranging from 0.49 to 0.59 (Table 3). The lower resemblance in the shape of inner cavities is mainly due to the structural rearrangements induced in sites 1a and 1b by the displacement of the heme after opening of the loop AB at high pH (see Fig. S5 in the Supporting information).

3.4. Ligand migration in NP7

The inner cavities define a pathway leading from the heme to the back of the protein. The continuous linkage between cavities, however,

Table 3
Similarity indexes between the inner cavities found in trajectories run for open and closed states of wild type NP7 with Amber and Charmm force fields. The similarity was determined using Tanimoto's distance.

	Open_2 (Amber)	Open (Charmm)	Closed_1 (Amber)	Closed_2 (Amber)	Closed (Charmm)
Open_1 (Amber)	0.77	0.81	0.53	0.53	0.55
Open_2 (Amber)		0.71	0.51	0.49	0.49
Open (Charmm)			0.52	0.53	0.59
Closed_1 (Amber)				0.90	0.76
Closed_2 (Amber)					0.81

is achieved only when the isocontour of the frequency map ( ) is reduced to ~0.35. For the sake of comparison, let us note that the tunnels found in the ligand-bound forms of *M. tuberculosis* HbN [56,57] and *A. thaliana* nonsymbiotic AHb1 [58] are clearly delineated at much higher isocontours (~ 0.7). This suggests that the docking sites found in wt NP7 better reflect a set of individual cavities rather than a well-shaped channel.

To investigate the feasibility of ligand migration between cavities, ILS calculations were performed for 20 ns time windows using the snapshots sampled in the trajectories that were run for open and closed states. Similar results were obtained between the energetic profiles derived for time windows of 60–80 and 80–100 ns, thus giving support to the structural stability of the inner cavities. For the closed protein, a continuous linkage between sites 1 and 3 is achieved for an energy isocontour of 3.0 kcal/mol, as shown in Fig. 5, which suggests that a gaseous diatomic ligand should easily exchange between the two sites. In contrast, Fig. 5 also shows that at the same isocontour value there is no connection between sites 1 and 3 in the open state of wt NP7. In fact, a much higher energy (around 15 kcal/mol) is required in order to link the two inner cavities (data not shown). Therefore, a free gaseous molecule should be mainly confined in site 1 or alternatively released to the solvent at high pH.

In order to further explore the preceding findings, a series of MD simulations were run to explore the diffusion of unrestrained NO in the open and closed states of the protein. Simulations were started from the last snapshot of the trajectories run for open and closed states of the CO-bound NP7. Four distinct initial positions were chosen for NO (see Fig. S6 in the Supporting information): A) in the interior of site 3, near residues Leu15 and Gly81, B) the interface between sites 1 and 2, close to the heme and residues Ile121, Ile123, Leu135 and Leu139, C) in the solvent exposed area of site 1, close to residues Tyr30 and Ile132, and D) finally in a solvent-exposed region close to the N-terminus, around residues Leu1, Asp34 and Gln36. For each starting position, the systems were thermalized following the protocol mentioned above (see Materials and methods), and 10 (Amber) and 5 (Charmm) MD simulations were run up to 20 ns using both parm99SB and charmm22 force fields and the same simulation conditions.

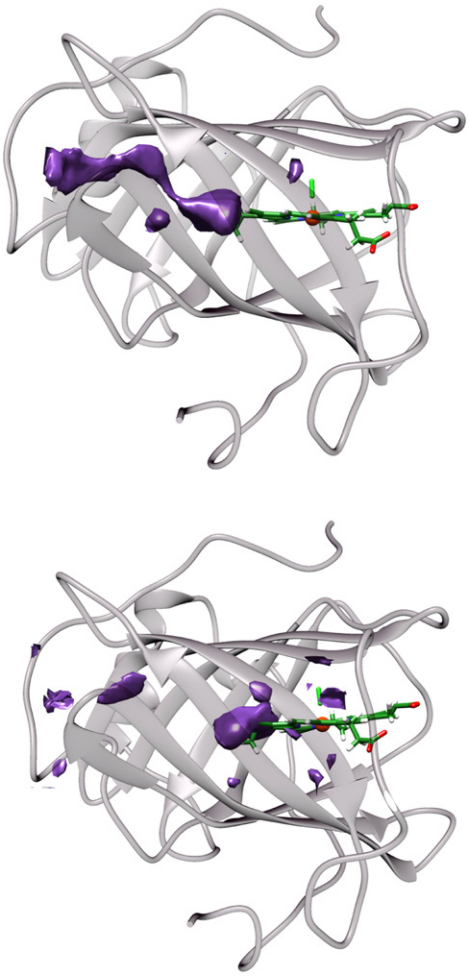

Fig. 5. ILS energetic profile linking inner cavities in (top) closed and (botom) open forms of wild type NP7. The isocontour derived from the analysis of the 80–100 ns time window corresponds to an energy value of 3.0 kcal/mol.

For the closed state of wt NP7, the analysis of the positions sampled by NO in the interior of the protein (see below) reflects the topological features of the cavities identified from MDpocket analysis, as noted in the comparison of Fig. 4a and b. Thus, NO molecules primarily populate sites 1a, 1b and 3, whereas a lower occupancy is found for site 2, suggesting a lower effective volume for accommodating the ligand in this latter cavity. The trajectories that started from position D led to ligand egression in all cases. For position C, the ligand was either released to the solvent during equilibration or migrated through the docking sites, and in few cases it was released to the solvent from site 3 through the back of the protein (near residues Leu15 and Gly81). Finally, the trajectories started from positions A and B led to either retention of NO in the interior of the protein (70% of cases) or to egression through the back of the protein (30% of cases).

The distribution of NO between sites 1 and 3 is well reflected in the distribution plots shown in Fig. 6a. Thus, the trajectories started from position A (site 3) sample regions to position B (site 1) and vice versa. The migration of the ligand between sites 1 and 3 suggests the existence of small energy barriers for diffusion through the interior of the β-barrel, in agreement with the linkage between sites 1 and 3 found from ILS calculations (see Fig. 5). Finally, the lack of the peak corresponding to site 2 suggests that it is only transiently populated in the exchange pathway between sites 1 and 3. Accordingly, site 2 should not be treated as a stable docking site, but rather as a temporary site that bridges cavities 1 and 3.

For the open structures, all the trajectories started from positions B, C and D released NO to the solvent through the front side (distal cavity) of the protein, in agreement with the physiological function of releasing NO at the plasma pH. Only in one case NO migrated through the cavities and exited through the back of the protein (site 3), When the simulations started from position A (site 3), however, the ligand was released to the solvent only through the back of the protein. In contrast to the closed structures, the ligand is mainly localized in site 3 (see Fig. 6b), indicating the existence of enhanced barriers for ligand diffusion to site 1, in agreement with the larger isoenergy contour required to link sites 1 and 3 from ILS calculations (see above). This is supported by the larger thermal fluctuations of the residues that define the distinct cavities in the β-barrel, as noted in Fig. 7, which compares the root-mean square fluctuations (RMSF) in both open and closed states. Thus, the lower flexibility of the β-barrel residues in the open state likely contributes to the larger barrier for ligand exchange between docking sites.

3.5. Ligand migration in NP7(Δ1–3)

The preceding data point out that sites 1a, 1b and 3 are effective in trapping a fraction of the photolyzed ligand, though this effect is more relevant for the closed form of wt NP7, as suggested by the lower free energy of the reaction intermediates corresponding to the internal docking sites [28]. To assess the influence of the open and closed states on the ligand migration within the NP7(Δ1–3) mutant, MD simulations on this protein were performed using the charmm22 force field.

The overall structure of NP7(Δ1–3) shows a large resemblance with the wt protein, as noted in RMSD values for the backbone

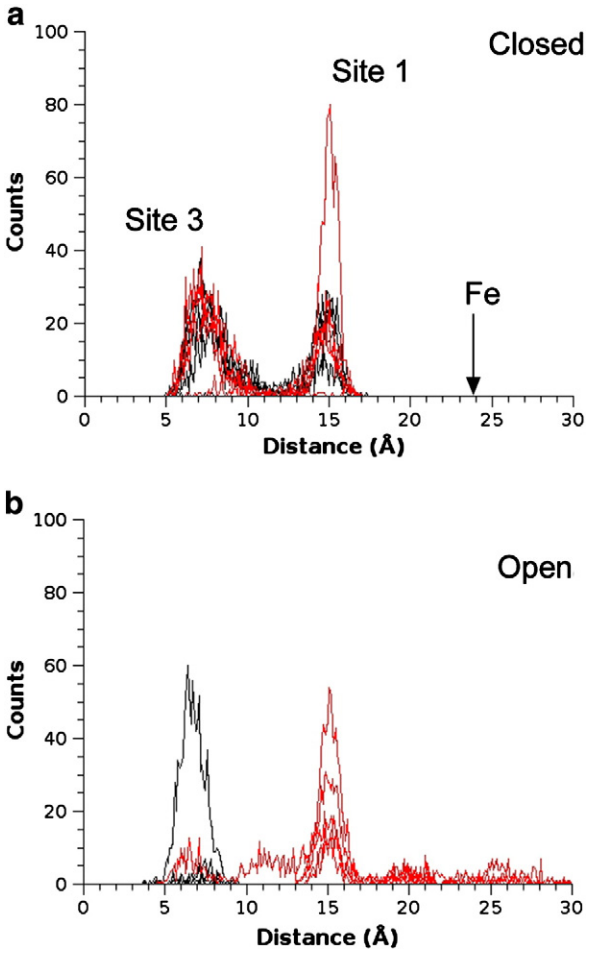

Fig. 6. NO distribution profile in MD (Charmm) simulations for unrestrained NO leading to migration through the protein interior of wild type NP7 in (a) closed and (b) open states. The position of the ligand is indicated relative to the distance (Å) of the nitrogen atom of NO to the Cα atom of Gly81 at the back of the protein, which was chosen as reference due to the structural preservation of the β-barrel structure in MD simulations of both closed and open NP7, in contrast to the largest geometrical changes observed for the heme in the simulations at high pH. Trajectories starting from positions A and B are shown as black and red lines.

atoms of 1.52 and 1.42 Å for the open and closed species, respectively (see also Fig. S7 in Supporting information). The MDpocket analysis also supports the topological resemblance between the inner cavities in both wt NP7 and its NP7(Δ1–3) variant. Thus, the Tanimoto's distances between wt and mutated proteins were 0.65 (open) and 0.74 (closed), whereas the cross (open versus closed) similarity index was 0.54, thus mimicking the trends found for wt NP7 (see above and Table 3). Finally, we have also run MD simulations to examine the motion of unrestrained NO through the protein using the same set of starting positions and simulation protocol. The analysis of the trajectories confirms the results reported for wt NP7. In particular, the NO distribution profiles confirmed the enhanced diffusion of the ligand between sites 1 and 3 for the closed NP7(Δ1–3) compared to the open species, where ligand migration between inner cavities seems to be more impeded (see Fig. 8).

Overall, these results allow us to suggest that deletion of the first three residues at the N-terminus does not introduce drastic structural alterations in NP7. This supports the existence of a common pattern for ligand migration in both wt NP7 and NP7(Δ1–3), in agreement with the similarity in the kinetic rate constants reported in Table 1.

3.6. Comparison with NP4

Previous kinetic studies have suggested the existence of a larger number of NO/CO docking sites in NP7 compared to NP4. In order to explore the structural basis of this difference, MDpocket calculations were performed over the snapshots taken from the trajectories collected for NP4 in previous studies [18,21] (since a similar topological pattern is found for both open and closed forms of NP4, we limit the discussion to the comparison of the cavities in the closed state).

A series of similarities and differences are apparent in the comparison of the topological features of inner cavities in NP4 (Fig. 9) and NP7 (Fig. 4a). There are two separate docking sites near the inner edge of the heme. Let us note that site 1b′ contains the Xe atom of the heme, with an occupancy of 1, as found in the X-ray structure of NP4 crystallized at pH 7.5 under Xe pressure (PDB ID: 1U0X; [59]). However, there is no overlap between site 1a′ and the second Xe atom, which has a much lower occupancy likely due to the partial opening of the loops in the crystallographic structure. In fact, the cavity filled with the Xe atom is formed by the side chains of Leu123, Leu 130, Lys125 and Lys128, and it is assisted by the salt bridges formed by the amino groups of the two Lys residues with the heme propionates. In solution, however, hydration of charged groups and thermal fluctuations of the loop that encompass these residues explain the

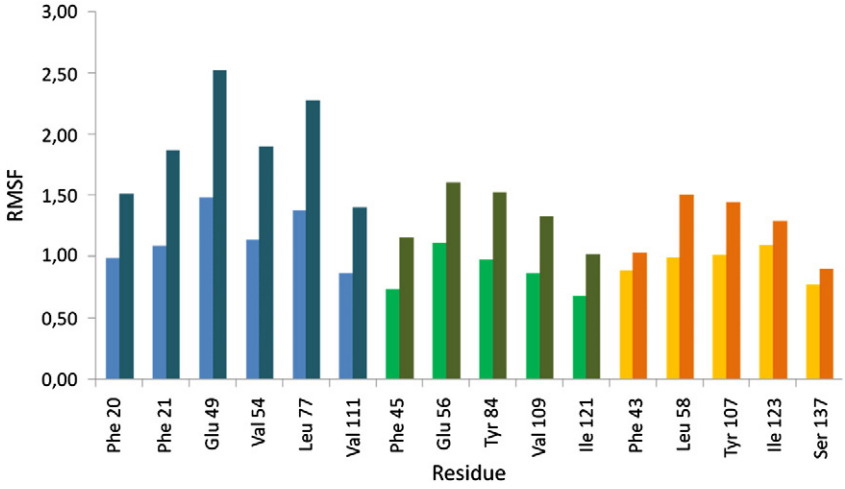

Fig. 7. Representation of the root-mean square fluctuations (RMSF; Å) for the set of residues that shape the cavities in wild type NP7. The RMSFs determined for sites 1, 2 and 3 are shown as blue, green and yellow bars, following the color code in Fig. 4. Dark and light colors denote the values for closed and open structures.

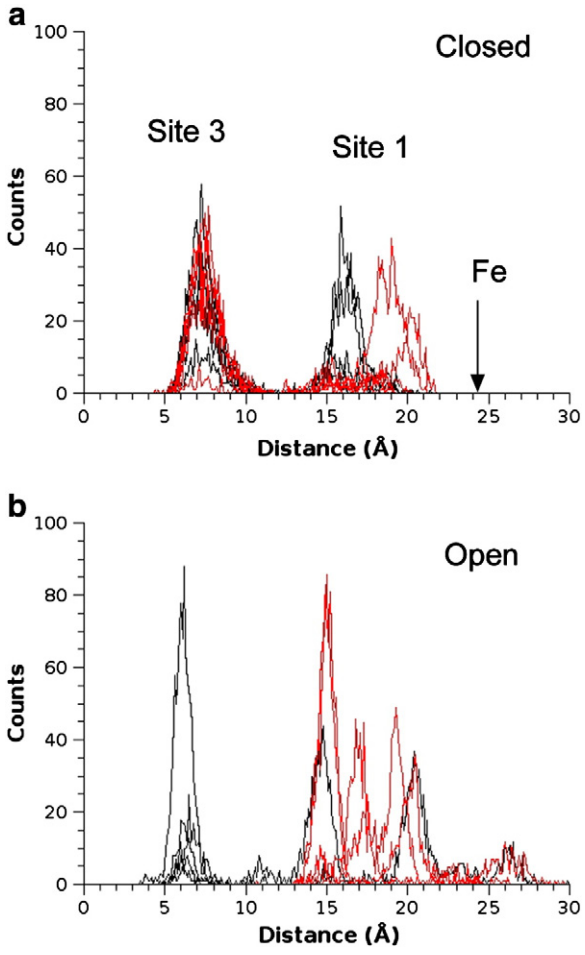

Fig. 8. NO distribution profile in MD (Charmm) simulations for unrestrained NO leading to migration through the protein interior of NP7(Δ1–3) in (a) closed and (b) open states. The position of the ligand is indicated relative to the distance (Å) of the nitrogen atom of NO to the Cα atom of Gly81 at the back of the protein. Trajectories starting from positions A and B are shown as black and red lines.

disappearance of the low occupancy Xe site in MD simulations. Site 1a′ in NP4 roughly agrees with site 1a in NP7, though the shape is slightly altered due to the changes Ile123(NP7) ↔ Thr121(NP4) and Ser137(NP7) ↔ Ala135(NP4), which enlarge the cavity volume in NP4 (see Fig. 10). However, sites 1b′ in NP4 and 1b in NP7 are found in distinct regions, this alteration being mainly due to the variations Phe43(NP7) ↔ Ala42(NP4) and Val109(NP7) ↔ Phe107(NP4), which would displace the location of this site in the two proteins.

Site 3′ is found at the back of NP4, though its size is smaller compared to NP7 and is divided in two areas, likely due to the variant Leu15(NP7) ↔ Phe12(NP4). However, the most relevant difference between the two proteins is that the site 2 in NP7 is absent in NP4. This may be interpreted by the combined effect of the variants Phe20(NP7) ↔ Tyr17(NP4), Val109(NP7) ↔ Phe107(NP4) and Gly75(NP7) ↔ Leu74(NP4). While the two former variations reduce the free space in the middle of the β-barrel, the latter displaces the position of Glu55 in NP4 (Glu56 in NP7) towards the interior and modifies the positions of Tyr82 and Tyr105 in NP4 (Tyr84 and Tyr107 in NP7), facilitating the opening of a small cavity between these residues in NP4 (but absent in NP7).

For our purposes here, let us stress that the lack of site 2 in NP4 should hinder the ligand exchange between sites 1′ and 3′ in NP4 compared to NP7. This agrees with the findings from previous MD simulations of NP4 where NO did not migrate to the interior of the protein [21,60], even though simulations were extended for more than 100 ns [60]. Furthermore, temperature derivative spectroscopy

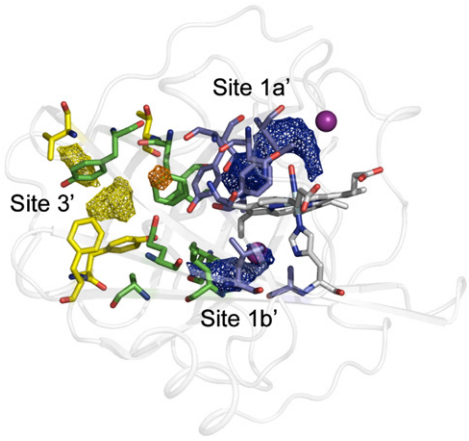

Fig. 9. Representation of the cavities identified by MDpocket analysis for the closed state of NP4. The cavities represent the regions enclosed by the isocontour value of 0.5 in the frequency map (ϕ). For the sake of comparison with Fig. 4a, sites 1′ and 3′ are represented using the same colors utilized for sites 1 and 3 in NP7, and the residues in NP4 that would shape the different docking sites in NP7 are represented as colored sticks. The small cavity shown as orange is absent in NP7. The Xe atoms in the X-ray structure PDB ID: 1U0X are shown as magenta spheres.

at cryogenic temperatures has shown that NO and CO rebinding to the heme occurs exclusively from the distal pocket [59]. Finally, the existence of the two docking sites 1a′ and 1b′ may explain the existence of the two phases seen in the kinetic trace of NO rebinding kinetics to ferrous NP4 [61]. While the first phase can be assigned to the rebinding directly from the distal pocket site 1a′, the second phase (geminate amplitude <5%), which is insensitive to the variation of the pH, may be ascribed to migration of photolyzed ligands to site 1b′.

3.7. Functional implications

The model of a pH-dependent closed and open structures as a consequence of protonation/deprotonation of Asp32, in conjunction with the hydrogen bond formation with Ile132, is based on the model derived for NP4, which is the functionally best understood isoprotein among the NPs. Recent kinetic studies have shown, nevertheless, distinctive trends between the two proteins, particularly regarding the larger capacity of NP7 to host internally a small gaseous ligand [28], leading to the hypothesis of a kinetic mechanism with an additional docking site in NP7 compared to NP4. This hypothesis is in agreement with the identification of three main cavities (sites 1a, 1b and 3) and the feasibility of ligand exchange between these docking sites in NP7. The different kinetic behaviors in NP4, however, should not be

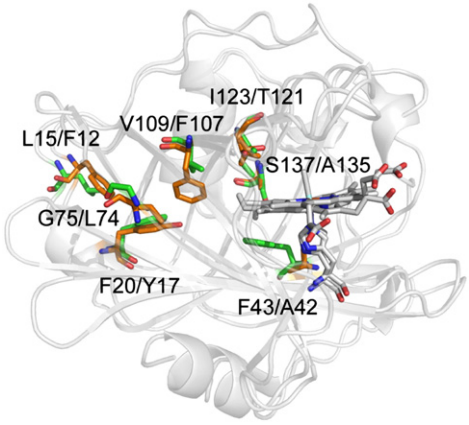

Fig. 10. Representation of selected differences in sequence between NP7 (green) and NP4 (orange) that alter the topologial features of inner cavities in the lipocalin β-barrel.

interpreted in terms of a drastically different topology for the inner cavities, as noted by the similar distributions of docking sites between NP4 and NP7, but as a consequence of the enhanced difficulty in exchanging the ligand between sites 1 and 3, as noted in previous experimental and theoretical studies [21,59–61]. Thus, experimental results benchmark the picture provided by the MD simulations.

Whereas the structure of NP4 does not facilitate the access to docking site 3′ in the interior of the protein, the exchange of ligands between sites 1 and 3 and the eventual egression to the solvent in NP7 suggest that this protein might be functionally linked to the existence of two pathways for ligand migration. One corresponds to the release through the distal cavity, which is greatly enhanced upon transition from closed to open states due to the breaking of the hydrogen bond between Asp32 and Ile132, and the concomitant opening of loops AB and GH. We propose that the second pathway would involve the access through site 3 at the back of the protein, near residues Leu15 and Gly81.

The question has been often raised why *R. prolixus* provides a bundle of NPs in its saliva instead of providing just one NP. The various isoproteins seem to address different targets in the host tissue, but in addition we also start to learn that the proteins have different mechanisms to provide their load to the specific target. Keeping in mind that most of the positively charged residues are located on the back of NP7, i.e., opposite the heme cavity, and that this protein exhibits the unusual property of targeting negatively charged phospholipid membranes [5,6,26], it can be speculated that the interaction with the membrane may alter the local structure at the back of the protein and thus facilitate the exchange of ligands between membrane and protein through internal diffusion from the heme to site 3.

With regard to the functional role of the NP7-specific N-terminus, the results do not allow us to provide a consistent conclusion. The computational structural data and also the kinetic data derived from CO rebinding studies do not disclose fundamental distinct trends between NP7 and NP7(Δ1–3). However, the NO distribution profiles show significant differences and, thus, suggest a non negligible influence of the Leu-Pro-Gly tail, as noted in the significant differences found in thermodynamic parameters K_{eq} and $E°$ obtained for both forms [26]. Hopefully, the availability of experimental structural information of NP7 might shed light into the functional implications of the N-terminus. While this study was conducted, diffracting crystals of NP7 were obtained [62], even though further improvement is still required to elucidate the ambiguous behavior of the electron density, which is currently on the way.[3]

4. Conclusions

The structural analysis of NP7 and NP7 (Δ1–3) points out the existence of three main cavities in the interior of the β-barrel, which as expected are composed by hydrophobic residues. Remarkably, the results support the feasibility of ligand exchange between the cavities in NP7 and NP7(Δ1–3) due to the presence of the passage defined by site 2. This is in contrast with the topology of inner cavities in NP4, providing a structural basis to the enhanced internal gas hosting capacity in NP7 and to the absence of ligand rebinding from secondary sites in NP4. Of particular interest is the docking site 3 in NP7 at the back of the protein, i.e., opposite the heme hosting cavity, as the back surface of NP7 is characterized by a massive clustering of Lys residues. This leads to the attachment of NP7 to negatively charged cell surfaces, a property that NP1–4 do not have. On the basis of these findings, one might be tempted to speculate that the processes of docking to cell surfaces and NO release might be interconnected, thereby supporting the release of NO into a target cell via site 3. Future studies will be conducted to examine the reliability of this hypothetical mechanism. The possibility of NO delivery through protein–membrane interaction resembles an interesting mechanism for NO signaling. Our results will provide an important basis for the future experimental and computational work to enlighten this process, including the generation and studies of site-specific mutant forms of NP7.

[3] H. Ogata, M. Knipp, work in progress.

Acknowledgements

The authors want to thank Carmen Risse and Johanna J. Taing for their assistance in the protein preparation. This work was supported by the Spanish Ministerio de Innovación y Ciencia (SAF2011-27642), the Generalitat de Catalunya (2009-SGR00298 and XRQTC), and the Italian Ministero dell'Istruzione, dell'Università e della Ricerca (PRIN 2008, 2008BFJ34R). AR acknowledges the Spanish Ministerio de Educación for financial support (SAB2010-0121). The work was supported in part by the Max Planck Society (to M.K.) CV acknowledges Italian Ministero dell'Istruzione, dell'Università e della Ricerca (Azioni Integrate Italia Spagna 2009, IT10L1M59M), and Ministero degli Affari Esteri, Direzione generale per la promozione del sistema Paese (Progetti di Grande Rilevanza, Italia-Argentina 2011–2013). This work was financially supported by the Vigoni Program, Project E65E06000080001 (to C.V.), and the Deutscher Akademischer Austausch Dienst (DAAD), Project 50728589 (to M.K.). The Barcelona Supercomputer Center (BSC) and the Centre de Serveis Científics i Acadèmics de Catalunya (CESCA) are acknowledged for providing the computational resources.

Appendix A. Supplementary data

Supplementary data to this article can be found online at http://dx.doi.org/10.1016/j.bbapap.2013.04.009.

References

[1] W.R. Montfort, A. Weischsel, J.F. Andersen, Nitrophorins and related antihemostatic lipocalins from *Rhodnius prolixus* and other blood-sucking arthropods, Biochim. Biophys. Acta 1482 (2000) 110–118.
[2] J.M.C. Ribeiro, J.M. Hazzard, R.H. Nussenzveig, D.E. Champagne, F.A. Walker, Reversible binding of nitric oxide by a salivary heme protein from a bloodsucking insect, Science 260 (1993) 97–105.
[3] D.E. Champagne, R.H. Nussenzveig, J.M.C. Ribeiro, Purification, partial characterization, and cloning of nitric oxide-carrying heme proteins (nitrophorins) from salivary glands of the blood-sucking insect *Rhodnius prolixus*, J. Biol. Chem. 270 (1995) 8691–8695.
[4] J.F. Andersen, D.E. Champagne, A. Weichsel, J.M.C. Ribeiro, C.A. Balfour, V. Dress, W.R. Montfort, Nitric oxide binding and crystallization of recombinant nitrophorin I, a nitric oxide transport protein from the blood-sucking bug *Rhodnius prolixus*, Biochemistry 36 (1997) 4423–4428.
[5] J.F. Andersen, N.P. Gudderra, I.M.B. Francischetti, J.G. Valenzuela, J.M.C. Ribeiro, Recognition of anionic phospholipid membranes by an antihemostatic protein from a blood-feeding insect, Biochemistry 43 (2004) 6897–6994.
[6] M. Knipp, H. Zhang, R.E. Berry, F.A. Walker, Overexpression in *Escherichia coli* and functional reconstitution of the liposome binding ferriheme protein nitrophorin 7 (NP7) from the blood sucking bug *Rhodnius prolixus*, Protein Expr. Purif. 54 (2007) 183–191.
[7] P. Ascenzi, M. Nardini, M. Bolognesi, W.R. Montfort, Nitrophorins: lipocalin-based heme proteins transporting nitric oxide, Biochem. Mol. Biol. Educ. 30 (2002) 68–71.
[8] M.J. Lehane, The Biology of Blood Sucking in Insects, 2nd ed. Cambridge University Press, Cambridge, United Kingdom, 2005.
[9] J.M.C. Ribeiro, F.A. Walker, High affinity histamine-binding and antihistaminic activity of the salivary nitric oxide-carrying heme protein (nitrophorin) of *Rhodnius prolixus*, J. Exp. Med. 180 (1994) 2251–2257.
[10] A. Weichsel, J.F. Andersen, D.E. Champagne, F.A. Walker, W.R. Montfort, Crystal structures of a nitric oxide transport protein from a blood-sucking insect, Nat. Struct. Biol. 5 (1998) 304–309.
[11] J.F. Andersen, A. Weichsel, C.A. Balfour, D.E. Champagne, W.R. Montfort, The crystal structure of nitrophorin 4 at 1.5 Å resolution: transport of nitric oxide by a lipocalin-based heme protein, Structure 6 (1998) 1315–1327.
[12] J.F. Andersen, W.R. Montfort, The crystal structure of nitrophorin 2. A trifunctional antihemostatic protein from the saliva of *Rhodnius prolixus*, J. Biol. Chem. 275 (2000) 30496–30503.
[13] C. He, H. Ogata, M. Knipp, Formation of the complex of nitrite with the ferriheme *b* β-barrel proteins nitrophorin 4 and nitrophorin 7, Biochemistry 49 (2010) 5841–5851.

[14] S.A. Roberts, A. Weichsel, Y. Qiu, J.A. Shelnutt, F.A. Walker, W.R. Montfort, Ligand-induced heme ruffling and bent NO geometry in ultra high-resolution structures of nitrophorin 4, Biochemistry 40 (2001) 11327–11337.
[15] R.E. Berry, M.N. Shokhirev, A.Y.W. Ho, F. Yang, T.K. Shokhireva, H. Zhang, A. Weichsel, W.R. Montfort, F.A. Walker, Effect of mutation of carboxyl side-chain amino acids near the heme on the midpoint potentials and ligand binding constants of nitrophorin 2 and its NO, histamine, and imidazole complexes, J. Am. Chem. Soc. 131 (2009) 2313–2327.
[16] T.K. Shokhireva, R.E. Berry, E. Uno, C.A. Balfour, H. Zhang, F.A. Walker, Electrochemical and NMR spectroscopic studies of distal pocket mutants of Nitrophorin 2: stability, structure, and dynamics of axial ligand complexes, Proc. Natl. Acad. Sci. U. S. A. 100 (2003) 3778–3783.
[17] D.A. Kondrashov, S.A. Roberts, A. Weichsel, W.R. Montfort, Protein functional cycle viewed at atomic resolution: conformational change and mobility in nitrophorin 4 as a function of pH and NO binding, Biochemistry 43 (2004) 13637–13647.
[18] J.M. Swails, Y. Meng, F.A. Walker, M.A. Martí, D.A. Estrín, A.E. Roitberg, pH-dependent mechanism of nitric oxide release in nitrophorins 2 and 4, J. Phys. Chem. B 113 (2009) 1192–1201.
[19] N.V. di Russo, D.A. Estrín, M.A. Martí, A.E. Roitberg, pH-Dependent conformational changes in proteins and their effect on experimental pKas: the case of nitrophorin 4, PLoS Comput. Biol. 8 (2012) e1002761.
[20] D.K. Menyhárd, G.M. Keserü, Protonation state of Asp30 exerts crucial influence over surface loop rearrangements responsible for NO release in nitrophorin 4, FEBS Lett. 579 (2005) 5392–5398.
[21] M.A. Martí, M.C. González-Lebrero, A.E. Roitberg, D.A. Estrín, Bond or cage effect: how nitrophorins transport and release nitric oxide, J. Am. Chem. Soc. 130 (2008) 1611–1618.
[22] J.F. Andersen, X.D. Ding, C.A. Balfour, T.K. Shokhireva, D.E. Champagne, F.A. Walker, W.R. Montfort, Kinetics and equilibria in ligand binding by nitrophorins 1–4: evidence for stabilization of a nitric oxide-ferriheme complex through a ligand-induced conformational trap, Biochemistry 39 (2000) 10118–10131.
[23] E.M. Maes, A. Weichsel, J.F. Andersen, D. Shepley, W.R. Montfort, Role of binding site loops in controlling nitric oxide release: structure and kinetics of mutant forms of nitrophorin 4, Biochemistry 43 (2004) 6679–6690.
[24] M.K. Callhan, P. Williamson, R.A. Schlegel, Surface expression of phosphatidylserine on macrophages is required for phagocytosis of apoptotic thymocytes, Cell Death Differ. 7 (2000) 645–653.
[25] U.A. Hirt, M. Leist, Rapid, noninflammatory and PS-dependent phagocytic clearance of necrotic cells, Cell Death Differ. 10 (2003) 1156–1164.
[26] M. Knipp, F. Yang, R.E. Berry, H. Zhang, M.N. Shokhirev, F.A. Walker, Spectroscopic and functional characterization of nitrophorin 7 from the blood-feeding insect *Rhodnius prolixus* reveals an important role of its isoform-specific N-terminus for proper protein function, Biochemistry 46 (2007) 13254–13268.
[27] M. Knipp, R.P. Soares, M.H. Pereira, Identification of the native N-terminus of the membrane attaching ferriheme protein nitrophorin 7 from *Rhodnius prolixus*, Anal. Biochem. 424 (2012) 79–81.
[28] S. Abbruzzetti, C. He, H. Ogata, S. Bruno, C. Viappiani, M. Knipp, Heterogeneous kinetics of the carbon monoxide association and dissociation reaction to nitrophorin 4 and 7 coincide with structural heterogeneity of the gate-loop, J. Am. Chem. Soc. 134 (2012) 9986–9998.
[29] R.E. Berry, D. Muthu, T.K. Shokhireva, S.A. Garrett, H. Zhang, F.A. Walker, Native N-terminus nitrophorin 2 from the kissing bug: similarities to and differences from NP2(D1A), Chem. Biodivers. 9 (2012) 1739–1755.
[30] S. Abbruzzetti, S. Bruno, S. Faggiano, E. Grandi, A. Mozzarelli, C. Viappiani, Time-resolved methods in Biophysics. 2. Monitoring haem proteins at work with nanosecond laser flash photolysis, Photochem. Photobiol. Sci. 5 (2006) 1109–1120.
[31] S. Sottini, C. Viappiani, L. Ronda, S. Bettati, A. Mozzarelli, CO rebinding kinetics to myoglobin- and R-state-hemoglobin-doped silica gels in the presence of glycerol, J. Phys. Chem. B 108 (2004) 8475–8484.
[32] S. Abbruzzetti, S. Faggiano, S. Bruno, F. Spyrakis, A. Mozzarelli, S. Delwilde, L. Moens, C. Viappiani, Ligand migration through the internal hydrophobic cavities in human neuroglobin, Proc. Natl. Acad. Sci. U. S. A. 106 (2009) 18984–18989.
[33] K. Arnold, L. Bordoli, J. Kopp, T. Schwede, The SWISS-MODEL workspace: a web-based environment for protein structure homology modeling, Bioinformatics 22 (2006) 195–201.
[34] A. Weichsel, W.R. Montfort, Unpublished data, Coordinates available from PDB, http://dx.doi.org/10.2210/pdb1t68/pdb.
[35] M. Knipp, J.J. Taing, C. He, Reduction of the lipocalin type heme containing protein nitrophorin — sensitivity of the fold-stabilizing cysteine disulfides toward routine heme-iron reduction, J. Inorg. Biochem. 105 (2011) 1405–1412.
[36] F. Yang, H. Zhang, M. Knipp, A one-residue switch reverses the orientation of a heme *b* cofactor. Investigations of the ferriheme NO transporters nitrophorin 2 and 7 from the blood-feeding insect *Rhodnius prolixus*, Biochemistry 48 (2009) 235–241.
[37] T.K. Shokhireva, A. Weichsel, K.M. Smith, R.E. Berry, N.V. Shokhirev, C.A. Balfour, H. Zhang, W.R. Montfort, F.A. Walker, Assignment of the ferriheme resonances of the low-spin complexes of nitrophorins 1 and 4 by ^{1}H and ^{13}C NMR spectroscopy: comparison to structural data obtained from X-ray crystallography, Inorg. Chem. 46 (2007) 2041–2056.
[38] V. Hornak, R. Abel, A. Okur, B. Strockbine, A. Roitberg, C. Simmerling, Comparison of multiple Amber force fields and development of improved protein backbone parameters, Proteins 65 (2006) 712–725.
[39] D.A. Case, T.A. Darden, T.E. Cheatham III, C.L. Simmerling, J. Wang, R.E. Duke, R. Luo, R.C. Walker, W. Zhang, K.M. Merz, B. Roberts, B. Wang, S. Hayik, A. Roitberg, G. Seabra, I. Kolossváry, K.F. Wong, F. Paesani, J. Vanicek, J. Liu, X. Wu, S.R. Brozell, T. Steinbrecher, H. Gohlke, Q. Cai, X. Ye, J. Wang, M.-J. Hsieh, G. Cui, D.R. Roe, D.H. Mathews, M.G. Seetin, C. Sagui, V. Babin, T. Luchko, S. Gusarov, A. Kovalenko, P.A. Kollman, AMBER 11, University of California, San Francisco, 2010.
[40] A.D. MacKerell Jr., D. Bashford, M. Bellott, R.L. Dunbrack Jr., J.D. Evanseck, M.J. Field, S. Fischer, J. Gao, H. Guo, S. Ha, D. Joseph-McCarthy, L. Kuchnir, K. Kuczera, F.T.K. Lau, C. Mattos, S. Michnick, T. Ngo, D.T. Nguyen, B. Prodhom, W.E. Reiher III, B. Roux, M. Schlenkrich, J.C. Smith, R. Stote, J. Straub, M. Watanabe, J. Wiorkiewicz-Kuczera, D. Yin, M. Karplus, All-atom empirical potential for molecular modeling and dynamics studies of proteins, J. Phys. Chem. B 102 (1998) 3586–3616.
[41] J.C. Phillips, R. Braun, W. Wang, J. Gumbart, E. Tajkhorshid, E. Villa, C. Chipot, R.D. Skeel, L. Kale, K. Schulten, Scalable molecular dynamics with NAMD, J. Comput. Chem. 26 (2005) 1781–1802.
[42] L. Boechi, P.A. Mañez, F.J. Luque, M.A. Martí, D.A. Estrín, Unraveling the molecular basis for ligand binding in truncated hemoglobins: the trHbO *Bacillus subtilis* case, Proteins 78 (2010) 962–970.
[43] W.L. Jorgensen, J. Chandrasekhar, J.D. Madura, R.W. Impey, M.L. Klein, Comparison of simple potential functions for simulating liquid water, J. Chem. Phys. 79 (1983) 926–935.
[44] J.P. Ryckaert, G. Ciccotti, H.J.C. Berendsen, Numerical integration of the Cartesian equations of motion of a system with constraints: molecular dynamics of n-alkanes, J. Comput. Phys. 23 (1977) 327–341.
[45] D.M. York, T.A. Darden, L.G. Pedersen, The effect of long-range electrostatic interactions in simulations of macromolecular crystals: a comparison of the Ewald and truncated list methods, J. Chem. Phys. 99 (1993) 8345–8348.
[46] P. Schmidtke, A. Bidon-Chanal, F.J. Luque, X. Barril, MDpocket: open-source cavity detection and characterization on molecular dynamics trajectories, Bioinformatics 27 (2011) 3276–3285.
[47] V. Le Guilloux, P. Schmidtke, P. Tuffery, Fpocket: an open source platform for ligand pocket detection, BMC Bioinformatics 10 (2009) 168.
[48] J. Muñoz-Muriedas, X. Barril, J.M. López, M. Orozco, F.J. Luque, A hydrophobic similarity analysis of solvation effects on nucleic acid bases, J. Mol. Model. 13 (2007) 357–365.
[49] J. Cohen, A. Arkhipov, R. Braun, K. Schulten, Imaging the migration pathways of O_2, CO, NO, and Xe inside myoglobin, Biophys. J. 91 (2006) 1844–1857.
[50] J. Cohen, K. Schulten, O_2 migration pathways are not conserved across proteins of a similar fold, Biophys. J. 93 (2007) 3591–3600.
[51] J. Cohen, K.W. Olsen, K. Schulten, Use of the conjugate peak refinement algorithm for identification of ligand-binding pathways in globins, Methods Enzymol. 437 (2008) 417–437.
[52] F. Forti, L. Boechi, D.A. Estrin, M.A. Marti, Comparing and combining implicit ligand sampling with multiple steered molecular dynamics to study ligand migration processs in heme proteins, J. Comput. Chem. 32 (2011) 2219–2231.
[53] F. Forti, L. Boechi, D. Bikiel, M.A. Marti, M. Nardini, M. Bolognesi, C. Viappiani, D. Estrin, F.J. Luque, Ligand migration in *Methanosarcina acetivorans* protoglobin: effects of ligand binding and dimeric assembly, J. Phys. Chem. B 115 (2011) 13771–13780.
[54] A. Bender, R.C. Glen, Molecular similarity: a key technique in molecular informatics, Org. Biomol. Chem. 2 (2004) 3204–3218.
[55] R. Carbó, L. Leyda, M. Arnau, How similar is a molecule to another? An electron density measure of similarity between two molecular structures, Int. J. Quantum Chem. 17 (1980) 1185–1189.
[56] M. Milani, A. Pesce, Y. Ouellet, P. Ascenzi, M. Guertin, M. Bolognesi, *Mycobacterium tuberculosis* hemoglobin N displays a protein tunnel suited for O_2 diffusion to the heme, EMBO J. 20 (2001) 3902–3909.
[57] A. Bidon-Chanal, M.A. Martí, A. Crespo, M. Milani, M. Orozco, M. Bolognesi, F.J. Luque, D.A. Estrin, Ligand-induced dynamical regulation of NO conversion in *Mycobacterium tuberculosis* truncated-hemoglobin-N, Proteins 64 (2006) 457–464.
[58] S. Faggiano, S. Abbruzzetti, F. Spyrakis, C. Viappiani, S. Bruno, A. Mozzarelli, P. Cozzini, A. Astego, P. Dominici, S. Brogioni, A. Feis, G. Smulevich, O. Carrillo, P. Schmidtke, A. Bidon-Chanal, F.J. Luque, Structural plasticity and functional implications of internal cavities in distal mutants of type 1 non-symbiotic hemoglobin AHb1 from *Arabidopsis thaliana*, J. Phys. Chem. B 113 (2009) 16028–16038.
[59] K. Nienhaus, E.M. Maes, A. Weichsel, W.R. Montfort, G.U. Nienhaus, Structural dynamics controls nitric oxide affinity in nitrophorin 4, J. Biol. Chem. 279 (2004) 39401–39407.
[60] D.A. Kondrashov, W.R. Montfort, Nonequilibrium dynamics simulations of nitric oxide release: comparative study of nitrophorin and myoglobin, J. Phys. Chem. B 111 (2007) 9244–9252.
[61] A. Benabbas, X. Ye, M. Kubo, Z. Zhang, E.M. Maes, W.R. Montfort, P.M. Champion, Ultrafast dynamics of diatomic ligand binding to nitrophorin 4, J. Am. Chem. Soc. 132 (2010) 2811.
[62] H. Ogata, M. Knipp, Crystallization and preliminary X-ray crystallographic analysis of the membrane-binding haemprotein nitrophorin 7 from *Rhodnius prolixus*, Acta Crystallogr. F68 (2012) 37–40.

Supporting Information

Kinetics and computational studies of ligand migration in nitrophorin 7 and its Δ1-3 mutant

Ana Oliveira[1,&] Alessando Allegri,[2,&] Axel Bidon-Chanal,[1] Markus Knipp,[3] Adrian E. Roitberg,[4] Stefania Abbruzzetti,[2] Cristiano Viappiani,[2,*] and F. Javier Luque[1,*]

[1] Departament de Fisicoquímica and Institut de Biomedicina (IBUB), Facultat de Farmàcia, Universitat de Barcelona, Campus de l'Alimentació Torribera, Santa Coloma de Gramenet, Spain

[2] Dipartimento di Fisica e Scienze della Terra, Università degli Studi di Parma, Parma, Italy

[3] Max Planck Institute for Chemical Energy Conversion, Stiftstrasse 34-36, D-45470 Mülheim an der Ruhr, Germany

[4] Quantum Theory Project and Department of Chemistry, University of Florida, Gainesville, Florida 32611-7200 USA

[&] These authors have contributed equally to this work.

[*] Corresponding authors: fjluque@ub.edu (FJL), cristiano.viappiani@fis.unipr.it (CV)

Figure S1. Sequence alignment (performed with BLAST)[a] of NP7 *versus* NP2 and NP4 from *R. prolixus*. The signal peptide that is cleaved during export into the salivary gland lumen is shown in yellow. The extra residues at the N-terminus of NP7 are colored as magenta. Loops AB and GH are colored as green and blue. The residues that form the hydrogen bond (Asp32, Ile132) in the closed state are marked in red.

Nitrophorin 7 vs. Nitrophorin 2

Score	Expect	Method	Identities	Positives	Gaps
265 bits(677)	3e-94	Compositional matrix adjust.	124/201(62%)	156/201(77%)	0/201(0%)

```
NP7       MELYTALLAVTILSPSSIVGLPGECSVNVIPKKNLDKAKFFSGTWYETHYLDMDPQATEK (40)
NP2       MELYTALLAVTILCLTSTMGVSGDCSTNISPKQGLDKAKYFSGKWYVTHFLDKDPQVTDQ (37)

NP7       FCFSFAPRESGGTVKEALYHFNVDSKVSFYNTGTGPLESNGAKYTAKFNTVDKKGKEIKP (100)
NP2       YCSSFTPRESDGTVKEALYHYNANKKTSFYNIGEGKLESSGLQYTAKYKTVDKKKAVLKE (97)

NP7       ADEKYSYTVTVIEAAKQSALIHICLQEDGKDIGDLYSVLNRNKNALPNKKIKKALNKVSL (160)
NP2       ADEKNSYTLTVLEADDSSALVHICLREGSKDLGDLYTVLTHQKDAEPSAKVKSAVTQAGL (157)

NP7       VLTKFVVTKDLDCKYDDKFLSSWQK (185)
NP2       QLSQFVGTKDLGCQYDDQFTSL (179)
```

Nitrophorin 7 vs. Nitrophorin 4

Score	Expect	Method	Identities	Positives	Gaps
152 bits(383)	4e-50	Compositional matrix adjust.	86/204(42%)	123/204(60%)	5/204(2%)

```
NP7       MELYTALLAVTILSPSSIVGLPGECSVNVIPKKNLDKAKFFSG-TWYETHYLDMDPQ-ATEK (40)
NP4       MKSYTSLLAVAILCL--FGGVNGACTKNAIAQTGFNKDKYFNGDVWYVTDYLDLEPDDVPKR (39)

NP7       FCFSFAPRESGGTVKEALYHFNVDSKVSFYNTGTGPLESNGAKYTAKFNTVDKKGKEIKP (100)
NP4       YCAALAAGTASGKLKEALYHYDPKTQDTFYDVSELQVESLG-KYTANFKKVDKNGNVKVA (98)

NP7       ADEKYSYTVTVIEAAKQSALIHICLQEDGKDIGDLYSVLNRNKNALPNKKIKKALNKVSL (160)
NP4       VTAGNYYTFTVMYADDSSALIHTCLHKGNKDLGDLYAVLNRNKDAAAGDKVKSAVSAATL (158)

NP7       VLTKFVVTKDLDCKYD-DKFLSSWQK (185)
NP4       EFSKFISTKENNCAYDNDSLKSLLTK (184)
```

[a] S.F. Altschul, J.C. Wootton, E.M. Gertz, R. Agarwala, A. Morgulis, A.A. Schäffer, Y.-K. Yu, Protein database searches using compositionally adjusted substitution matrices, FEBS J. 272 (2005) 5101-5109.

Figure S2. Representation of the orientations of the heme in nitrophorins.

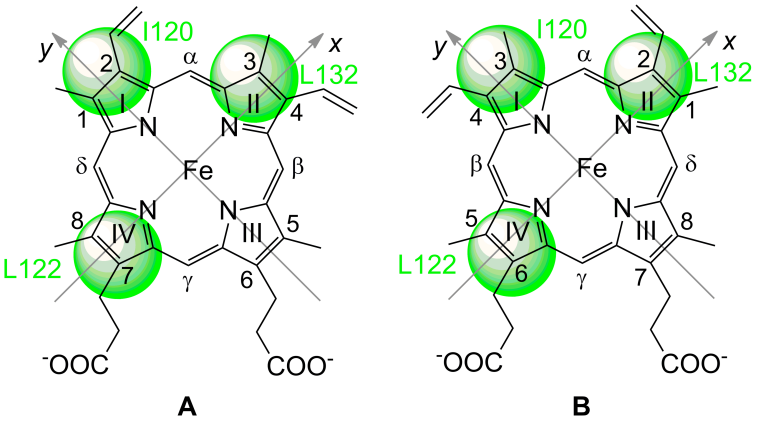

Figure S3. CO rebinding kinetics (recorded at 436 nm) to NP7(Δ1-3) (red, pH 7.5; green, pH=5.5) and NP7(Δ1-3)Met (blue, pH 7.5; black, pH=5.5) at T=20°C, 1 atm CO as a function of pH.

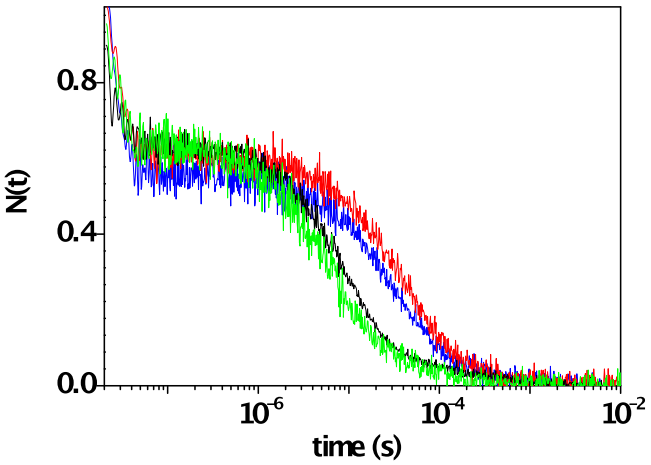

Figure S4. Representative fittings (black solid lines) of CO rebinding kinetics of (top) NP7(Δ1-3) and (bottom) NP7(Δ1-3)Met using Scheme 1. Blue, pH = 5.5, 0.1 atm CO; green, pH = 5.5, 1 atm CO; red, pH = 7.5, 0.1 atm CO; black, pH = 7.5, 1 atm CO. T=20°C.

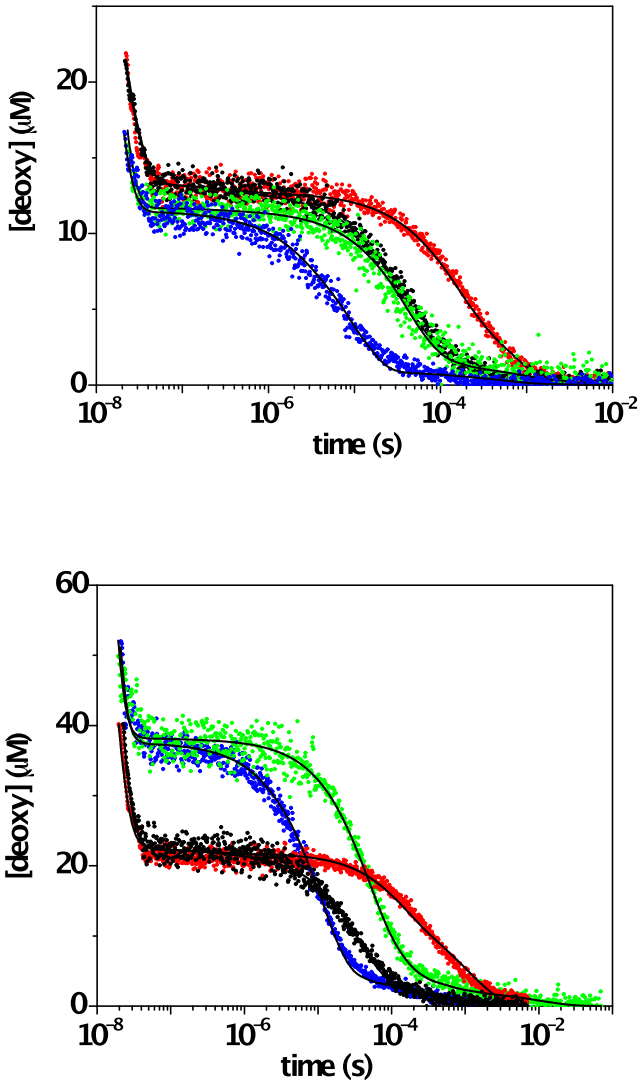

Figure S5. Superposition of the closed (grey) and open (green) structures of wild type NP7 derived from Charmm simulations. Breaking of the hydrogen bond between Asp32 and Ile132 present in the closed state introduces a drastic change in the conformation of loops AB and GH, which in turn alter the orientation of the heme in the protein.

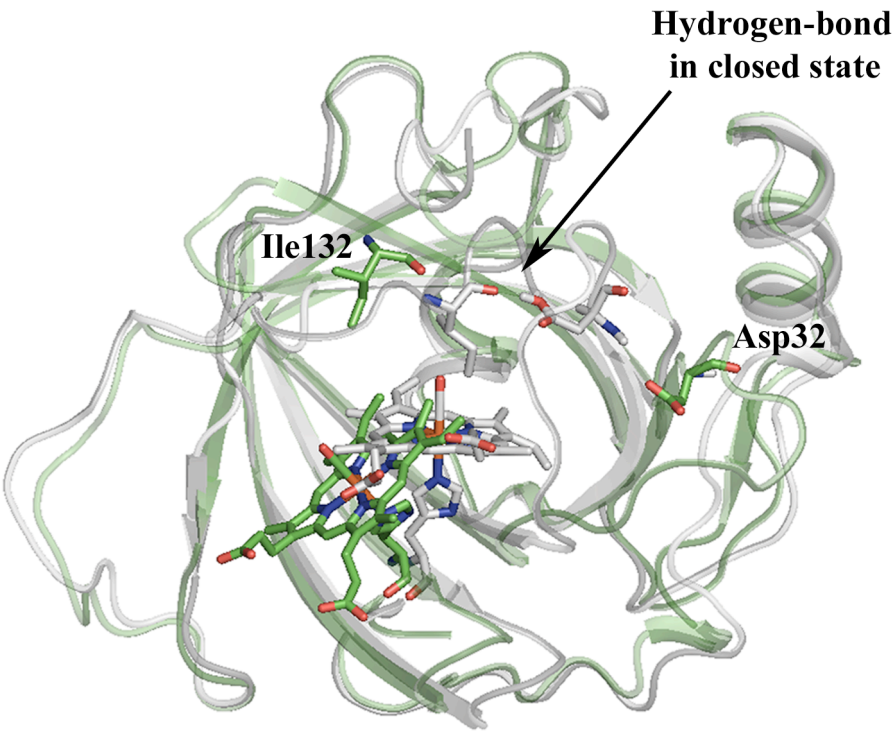

Figure S6. Representation of the starting positions chosen to explore the migration of free NO.

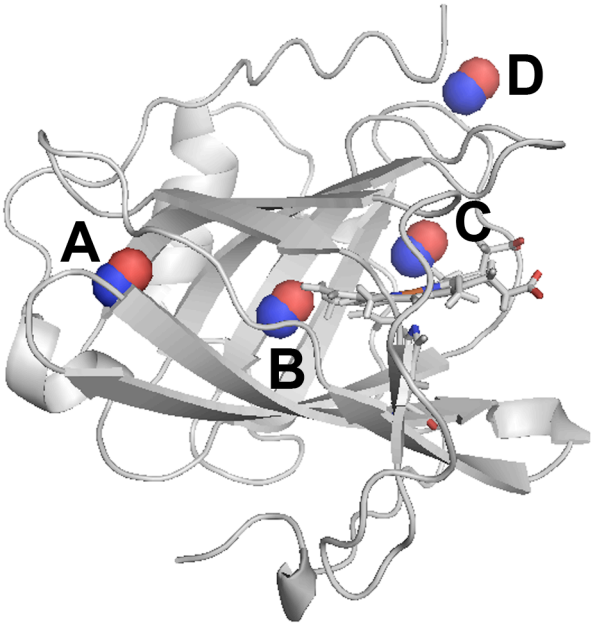

Figure S7. Superposition of the energy-minimized average structures derived from Charmm simulations of wild type NP7 and NP7(Δ1-3) in (a) open and (b) closed states. The regions corresponding to the first three residues at the N-terminus (in wild type NP7), loop AB and loop GH are shown as magenta, green and blue, respectively. The CO-bound ferriheme, the proximal histidine (His60) and the residues involved in hydrogen bonding in the closed state, Asp32 and Ile132, are shown as colored sticks.

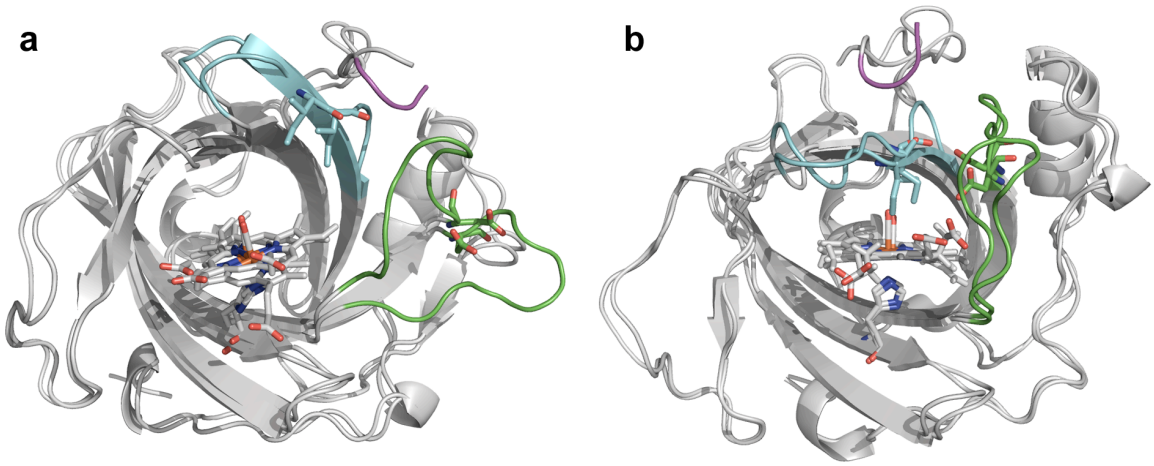

Chapter IV: Conclusions

Truncated Hemoglobin N from Mycobacterium Tuberculosis

- ✓ The mutation of PheE15 residue to Ala, Ile and Tyr in trHbN does not induce relevant structural changes neither on the protein global fold nor on the O_2 ligand kinetics, but shows a significant decrease in the NO detoxification activity.

- ✓ The diffusion of nitric oxide through the long branch of the tunnel is partially blocked for the PheE15 to Ala mutation as the introduction of a less voluminous residue promotes the narrowing of the channel at the entrance of the tunnel.

- ✓ For the other mutants, PheE15Ile and PheE15Tyr, the reduction of the NO detoxification may be explained by the blockage of the tunnel at the E15 position as in both cases opening of the channel is more difficult, thus limiting the access to the active site.

- ✓ The PheE15 residue is crucial for proper ligand migration to the active site and also contributes to avoid the collapse of helices B and E, thus preserving the ligand accessibility along the tunnel long branch.

- ✓ The complex between trHbN and Fdr is stabilized by several salt bridges formed by residues located in helices B and E and loop F of trHbN, which guide the interaction with the reductase partner and place both heme and FAD cofactors at a distance ranging from 6 to 9 Å.

- ✓ The CD-loop is essential for properly positioning of trHbN in the formation of the complex with its putative flavodoxin reductase, Fdr, and the efficiency of the ET process.

- ✓ An effective ET pathway is proposed to occur between the heme and the FAD cofactor mediated by water molecules ($FADH_2$ --- H_2O --- H_2O-Heme cofactor) and the polar residues of the CD-loop, Thr48 and Asn49.

Nitrophorin 7

- ✓ The structural analysis of NP7 and NP7 (Δ1-3) mutant proteins at both (low pH) closed and (high pH) open conformations pointed out the existence of three main cavities in the interior of the β-barrel that are mainly composed of hydrophobic residues. These cavities allow the diffusion of the ligand between the distal pocket and the back of the β-barrel (opposite position of the heme site).

- ✓ The analysis of the simulations run for NP7 and NP7 (Δ1-3) mutant proteins argues against a drastic effect of the first three residues on the structural properties of the protein, in agreement with the similar rate constants obtained from kinetic assays.

- ✓ Diffusion of the ligand through the inner cavities is modulated by the fluctuations of the residues that delineate the tunnel. For the closed conformation, higher fluctuations are found and the ligand diffuses from/to the solvent easily than in the closed form.

- ✓ The significant number of lysines located at the rear part of the protein enable the interaction of NP7 with negatively charged cell surfaces, a property that NP1-4 does not exhibit. The presence of transient docking sites inside the protein may allow ligand release of NO into cells through the membrane.

Chapter V: Appendix

5.1. Molecular simulations of globins: Exploring the relationship between structure, dynamics and function

In this chapter we describe a comparative analysis of the results obtained from the application of different computer simulation schemes, namely classical molecular dynamics simulations and hybrid quantum/classical (QM/MM) calculations to shed light on the structure and dynamics of globins, and on its kinetic behavior.

In globins the association rate constant reflect the balance between the ligand diffusion from the solvent protein until the heme cavity, and the ligand coordination to the heme. On the other hand, the dissociation rate constant depends also on the thermal breaking of the protein-ligand interactions and the ligand escape from the distal pocket to the solvent. The impact of these processes was here examined for diverse globins taken as representative examples from previous studies in the research group.

a) On the other hand, in absence of surround residues able to establish a permanent hydrogen bond, the heme may experience a number of “in-plane” and “out-of-plane” deformations, which can affect the O_2 binding affinity. The results show that out-of-plane distortions decrease the binding affinity, while in-plane distortions can increase or decrease it. Among in-plane distortions, the *breathing* mode, which involves the symmetric compression-expansion of the porphyrin ring, strongly modulates the binding affinity detail. These findings suggest that “steric compression” might have been exploited to modulate the binding affinity for gaseous ligands in *M. acetivorans* protoglobin, a protein found in Archea that contains a highly distorted heme.

b) Truncated hemoglobins (trHbs) are characterized by a typical structural fold with a two-over-two helical structure, and by a remarkable variability in the structure of the amino acid residues within the heme cavity, which provides a highly polar distal environment. The distal amino acid residues play an important role in regulating ligand binding. In particular, usually three potential hydrogen-bond donor may affect the binding of exogenous ligands: TrpG8 in trHbO, and TyrB10 and GlnE11 in trHbN.

In addition, trHbN displays an apolar tunnel system that connects the solvent with the active site, which may constitute a possible pathway to ligand entry, and the presence of two conformations for the residue PheE15, open and closed, which may regulate the nitric oxide access to the heme cavity through the long branch tunnel. These features have given rise to the hypothesis of a dual path-ligand dependent mechanism, bin which entry of O_2 through the short branch of the tunnel and subsequent binding to the heme would facilitate the opening of the long branch, which would in turn permit the entry of NO to accomplish the NO dioxygenase activity in the heme cavity.

c) Finally, in neuroglobin both proximal and axial positions are occupied by histidine residue. The direct coordination of HisE7 to the Fe atom leads to the formation of a endogenous reversible hexacoordinated globin (6c). This opens the way to another mechanism for regulating the accessibility of ligands to the heme, which would be mediated by the equilibrium between hexaccordinated and pentacoordinated forms of the globin. Therefore, the alteration of this equilibrium by a number of factors could facilitate or impede the binding of ligands and hence to regulate the biological function of the globin. In this context, the effect of pressure has been examined for neuroglobin and myoglobin. The results showed that under high pressure conditions the binding of O_2 was impeded due to the overall reduction of the protein mobility, particularly regarding the CD loop, while at normal pressure the protein reveal higher flexibility and a pentacoordination coordination is then favored.

Transworld Research Network
37/661 (2), Fort P.O.
Trivandrum-695 023
Kerala, India

Recent Advances in Pharmaceutical Sciences, 2011: 133-153 ISBN: 978-81-7895-528-5
Editor: Diego Muñoz-Torrero

6. Molecular simulations of globins: Exploring the relationship between structure, dynamics and function

Flavio Forti[1], Leonardo Boechi[2], Ana Novo de Oliveira[1], Damian Bikiel[2]
Pau Arroyo[2], Alejandro Nadra[3], Luciana Capece[2], Axel Bidon-Chanal[1]
Marcelo A. Martí[2,3], Darío Estrín[2] and F. Javier Luque[1]

[1]Departament de Fisicoquímica, Facultat de Farmàcia, and Institut de Biomedicina, Universitat de Barcelona, Avda. Diagonal 643, 08028 Barcelona, Spain; [2]Departamento de Química Inorgánica, Analítica, y Química Física, INQUIMAE-CONICET, Facultad de Ciencias Exactas y Naturales, Universidad de Buenos Aires, Buenos Aires, Argentina
[3]Departamento de Química Biológica, Facultad de Ciencias Exactas y Naturales Universidad de Buenos Aires, Buenos Aires, Argentina

Abstract. The discovery in the last two decades of novel members of the globin superfamily has challenged the conventional view about the structure and function of globins. Thus, peculiar structural differences are expected to have direct influence on properties related to ligand migration, binding affinity and heme reactivity. Molecular simulations are a valuable tool to gain insigth into the molecular mechanisms that underlie those structural differences, and their relationship with the diversity of functional roles. In this work, the impact of molecular simulations in exploring

Correspondence/Reprint request: Dr. F. J. Luque, Departament de Fisicoquímica, Facultat de Farmàcia Universitat de Barcelona, Avda. Diagonal 643, 08028 Barcelona, Spain. E-mail: fjluque@ub.edu
Dr. D. Estrín Departamento de Química Inorgánica, Analítica y Química Física, INQUIMAE-CONICET Facultad de Ciencias Exactas y Naturales, Universidad de Buenos Aires, Buenos Aires, Argentina
E-mail: dario@qi.fcen.uba.ar

the linkage between structure, dynamics and function is highlighted for three representative cases: the migration of ligands through the protein matrix of truncated hemoglobins, the modulation of binding affinity by heme distortion in protoglobin, and finally the functional implications due to the equilibrium between penta- and hexacoordination of the heme with distal histidine in neuroglobin.

Introduction

Globins are a family of heme-containing proteins found in all kingdoms of life. They belong to the hemeprotein superfamily, though they share some distinctive characteristics. In the Protein Data Bank around 2300 hemeproteins can be found, and they can be clustered in 34 different groups with very diverse structural and functional characteristics [1]. As members of this superfamily, globins are supposed to have evolved from a common ancestor and their characteristic tertiary structure is typically known as *globin fold*. This fold was identified in 1958 in myoglobin (Mb) [2], which was the first protein whose structure became solved by X-ray diffraction. In this sense, the *globin fold* was the first protein fold to be discovered. Though it originally consisted of a bundle of eight alpha helices, its generalized definition has been challenged in the last decades due to the discovery of new globins, which have a number of peculiar structural features. The *globin fold* is an all-alpha protein fold, since the only secondary structure found is the alpha-helix. Though primary sequences of globins can have as low as 16% sequence identity, the *globin fold* is highly conserved throughout the family.

Globins have evolved to play a variety of biological roles, such as transport and sensing of gases and catalysis of reactions between nitrogen and reactive oxygen species [3-5]. Some of them are present as monomers under physiological conditions, though others form multimeric species, as illustrated by the prototypical cases of mammalian Mb –monomeric– and hemoglobin (Hb) –tetrameric- [5-8]. As mentioned before, globins generally adopt a common *globin fold* characterized by a 3-over-3 helical sandwich (A/BC/E and F/G/H helices), which contains the hydrophobic pocket that accommodates the heme group. The heme iron is coordinated to the only fully conserved residue along this family: the proximal HisF8 [9], leaving the sixth coordination position in the distal side usually free for binding of the exogenous ligand. Typical exogenous ligands are NO, CO and O_2, being molecular oxygen the most abundant and the one with the lowest affinity for free heme. Therefore, O_2 affinity is a key parameter for gaining insight into the function of globins.

The affinity of a protein for a ligand is characterized by the equilibrium constant K, which in turn can be related with the ratio between the apparent kinetic rate constants for the association and dissociation processes, called k_{on} and k_{off} respectively (see Fig. 1 for the binding of O_2 to the ferrous form of a hemeprotein).

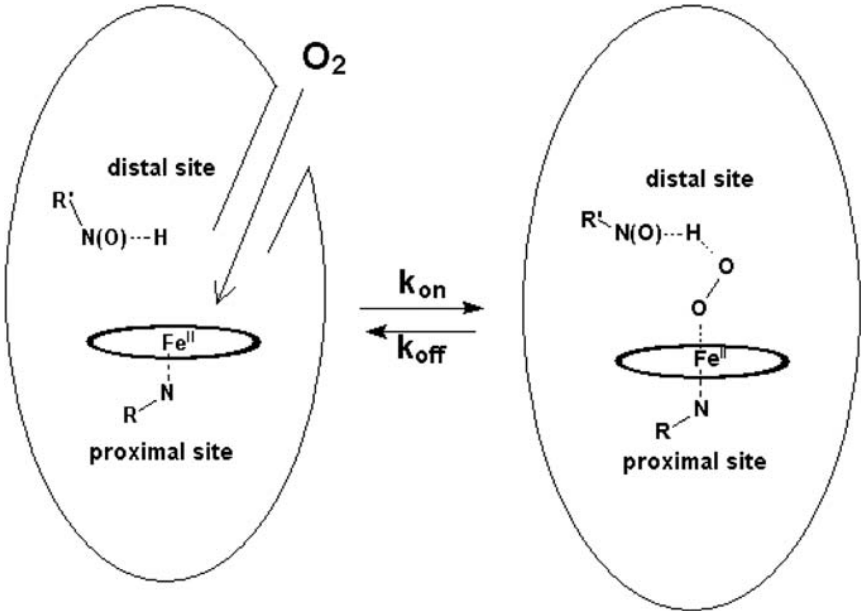

Figure 1. Schematic representation of the association and dissociation processes of small molecules to the heme moiety in globins.

In most globins, the association rate constant depends on two processes: i) ligand migration from the solvent to the heme active site, and ii) ligand coordination to the heme iron [3]. The ligand migration process is regulated by the presence of internal pockets or even tunnels [10-12], and the presence of specific residues that are capable to act as "gates" [7]. In some cases, a distal site residue (mainly His, Tyr) is able to bind to the Fe atom in the so-called *internal hexacoordination*, which affects the entire process [13-16]. On the other hand, non-coordinated water molecules located in the distal site can also modulate the k_{on}, adding another variable to the complexity of the association process [17-19]. Moreover, the coordination step depends on the spin state of the ligand and the relative in-plane position of the iron. For these reasons, in most cases the value of k_{on} for O_2 is higher than for CO, whereas the k_{on} value for NO is even higher [7]. The association rates span a wide range of values (spanning up to five orders of magnitude), starting at about 10^4 $M^{-1}s^{-1}$ in those systems with very low accessibility to the iron, and rising to 10^9 $M^{-1}s^{-1}$ when the association rate is mainly controlled by the diffusion from the solvent to reach the protein, as observed for isolated porphyrins [7,20].

The dissociation constant (k_{off}) involves two processes: i) thermal breaking of the protein-ligand interactions, and ii) ligand escape from the active site into the solvent. Dissociation rate constants are generally regulated mainly by the protein-ligand thermal breaking step, and span a range of roughly seven orders of magnitude (from 10^{-3} s^{-1} to 10^4 s^{-1} [3, 7, 21]). Both

diffusion and breaking of protein-ligand interaction are processes that vary from ligand to ligand, thus leading to a wide range of ligand affinities. Oxygen binds exclusively to ferrous (Fe_{II}) heme, and its dissociation rate constant is strongly influenced by interactions between the coordinated O_2 and the protein matrix [22]. For CO and NO, the dissociation from ferrous heme is mostly dominated by breaking of the Fe-ligand bond, and similarly low values ($\approx 1 \times 10^{-2}$ s^{-1}) are observed for many different proteins [3]. In the O_2 case, the energy required for breaking the protein-ligand bond is regulated by several factors, which include [23,24]:

- *distal effect*, which accounts for the interaction of the ligand with hydrogen-bond donor residues present in the distal cavity,
- *proximal effect*, which takes into account the influence of the local structure of the axial histidine, and
- *heme distortion*, which alters the strength of the Fe-ligand bond.

In the last decades new members of the globin family have been discovered, greatly expanding the globin world. Thus, globins are widely distributed and exhibit an intricate and complex phylogenetic network, which has been proposed to be divided in three main lineages [25]. Novel globins show distinct structural and functional features when compared to the emblematic mammalian Mb and Hb (Fig. 2). Apart from the canonical 3/3 Mb fold, which encompasses many different globins, another lineage shows a characteristic fold denoted as 2/2 Hb, which has been found in the three domains of life [25]. The 2/2 Hb fold, also referred to as *truncated* Hb, is around 20-30 residues shorter than Mb and exhibits a 2-over-2 sandwich fold involving only BC/E and G/H helices, in contrast to the classical 3-over-3 fold. The 2/2 Hbs have been proposed to act as small gas molecule sensors, oxygen carriers and pseudoenzimes.

Another of these lineages includes protoglobin and globin-coupled sensor (GCS) proteins, whose globin domain is bigger than Mb (~190 amino acids; [25-28]). Protoglobins are the first single-domain GCS-related globins found in *Archaea*. They can bind O_2, CO and NO reversibly *in vitro*, but so far their function is unknown [25,26,28] .

In the following sections we firstly describe the main features of Mb, which can be considered a prototypical example found in many textbooks, and three different globins with specific characteristics that make them to be representative examples of the structural and functional diversity of the globin family (Fig. 2):

- *Truncated hemoglobins*: Members of the 2/2 Hb subgroup, the second lineage of the globin family. In some cases, they have been related to the defense of the bacteria against nitrosative stress.

- *Protoglobin*: The 3D structure has been recently solved [29], though its function remains unknown. This protein hosts an unusually distorted heme and exhibits a very low dissociation constant for O_2.
- *Neuroglobin*: Member of the subgroup of globins with relevant internal hexacoordinated phenomena.

Brief survey of mammalian *myoglobin* (Mb)

Mb is not only a member of the first lineage of globins, but one of the most studied proteins. For this reason it is often referred to as the hydrogen atom of biology [30]. Its 3D structure was solved more that 50 years ago by J. Kendrew and coworkers [2], finding that deserved the Nobel Prize in Chemistry in 1962. Despite being one of the most studied proteins, there is still intense research effort due to its complexity, biological relevance and ongoing debate of its physiological function [31].

Mb is a cytoplasmic globin consisting of 154 amino acids expressed in cardiac mytocytes and oxidative skeletal muscle fibers. Like Hb, Mb reversibly binds O_2. However, Mb has a characteristic Michaelis-Menten hyperbolic O_2-saturation curve, while a sigmoid-shaped curve is seen in tetrameric Hb, thus reflecting the well known allosterism effect in this latter protein. From a biochemical point of view, Mb acts as O_2 storage protein in muscle, which is especially evident in marine mammals and birds that undergo extended periods of apnea, or in humans and other species living at high altitude. It has also been proposed as a buffer of intracellular O_2 pressure in a number of species [31], maintaining O_2 concentration relatively constant despite the occurrence of induced changes in O_2 level.

There is more controversy about the role of Mb in assisting O_2 diffusion in the cell. Desaturated Mb close to the cell membrane could bind O_2 and diffuse to the mitochondria, thus representing an alternative way of simple O_2 diffusion [31]. However, contrary to what it could be expected from its role, knockout experiments in mice with no Mb in skeletal muscles showed survival of the organism without severe biological consequences. This raises the question of whether other proteins could compensate for Mb absence. Beyond O_2 biochemistry, Mb has also been related to inactivation of NO and scavenging reactive O_2 species [31].

Besides the described roles and the increasing number of studies done so far, there are still open questions about Mb that require further research. For instance, what are the factors that regulate its expression in response to hypoxic situations? The discovery of other tissue globins such as neuroglobin (presented in the last section) and cytoglobin raises the question about the complexity of the underneath physiological model governing skeletal muscle biology.

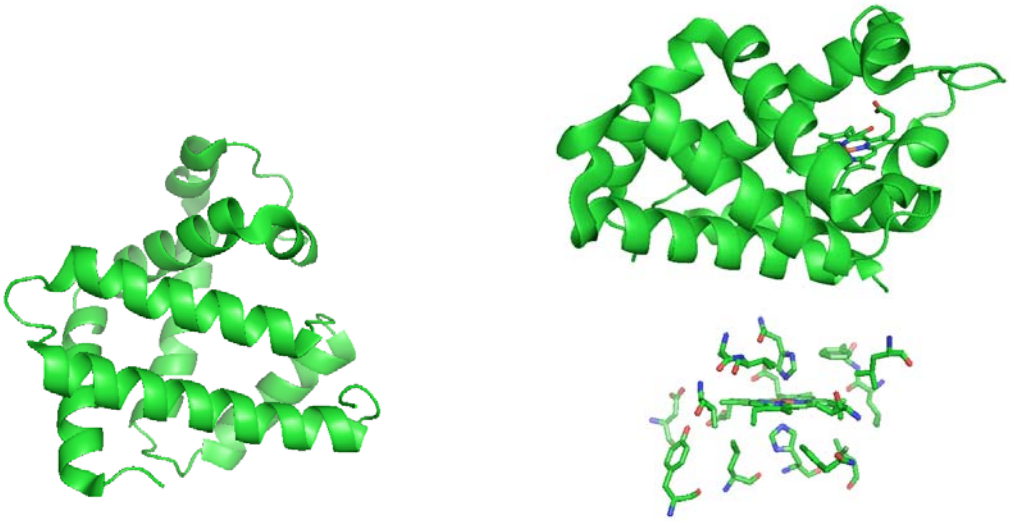

3-on-3 globin fold
Myoglobin

Hexacoordination
Neuroglobin:

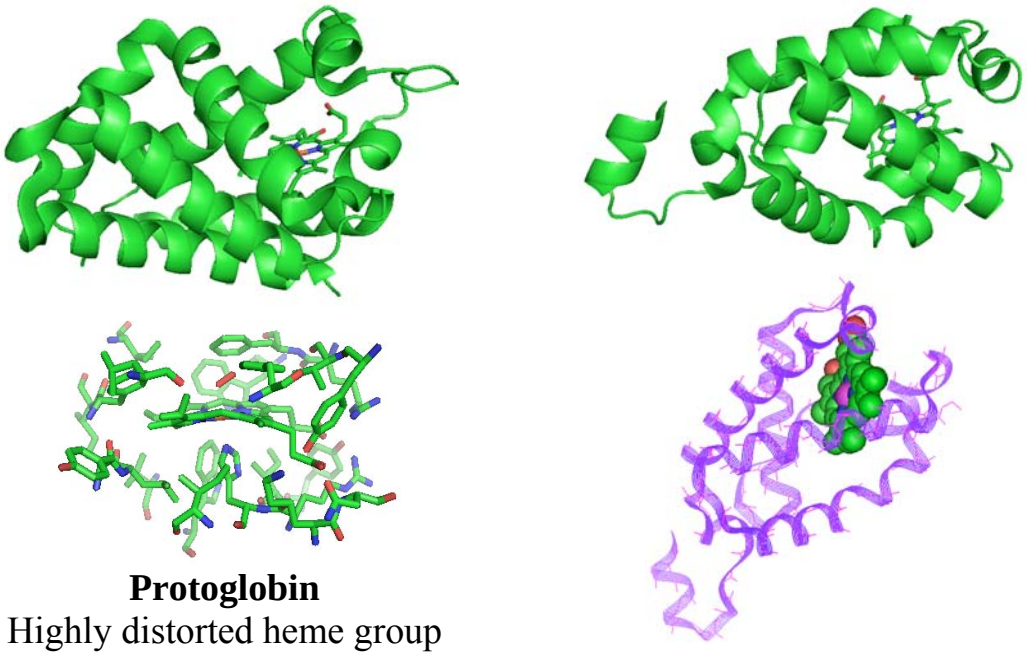

Protoglobin
Highly distorted heme group

Truncated hemoglobin N:
2-2 Sandwich fold

Figure 2. Globin diversity represented by *myoglobin (upper-left), neuroglobin (upper-right), protoglobin (lower left) and truncated hemoglobin N (lower right).*

1. 2/2 Hbs (truncated) proteins

The 2/2 Hb family can be further divided into 3 groups: I, II, III (also known as N, O, P). Group I shows a typical tunnel system that connects the solvent with the distal site. Groups II and III share a common TrpG8 and

generally do not exhibit well delineated tunnels for ligand migration. A network of hydrogen bonds stabilizing the exogenous ligand in the heme distal site is found in all three groups.

Truncated hemoglobin N of *Mycobacterium tuberculosis* (Mt-trHbN) is the most studied member of the 2/2 globins. For that reason, we will focus on the description of the mechanism of ligand migration from the solvent to the heme pocket in this protein, and later we compare these results with other Hbs belonging to groups O and P.

The Mt-trHbN case

Mycobacterium tuberculosis is responsible for tuberculosis in humans [32]. During the first stages of the infection the bacteria is attacked by macrophages that generate large amounts of NO [33]. It has been shown that certain Hbs that are present in some microorganisms are related to its ability to detoxify NO [34,35]. These defense mechanism would be related to O_2-bound globins that could convert NO to nitrate anion following the reaction Fe(II)-O_2 + NO → Fe(III) + NO_3^-. In *M. tuberculosis* two 2/2 Hbs are capable of performing such detoxifying reaction: *truncated Hb N* and *truncated Hb O*. One of the most interesting characteristics of these globins is the presence of an apolar tunel system that connects the solvent with the active site [36], which is postulated to be involved in migration of ligands (O_2, NO). In particular, in Mt-trNHb there are two perpendicular tunnels: the so-called Short Tunnel G8 (STG8), which is around 8 Å long and is delineated by residues in helices G and B, and the Long Tunnel (LT), which is around 20 Å long and is mainly defined by helices B and E (Fig. 3).

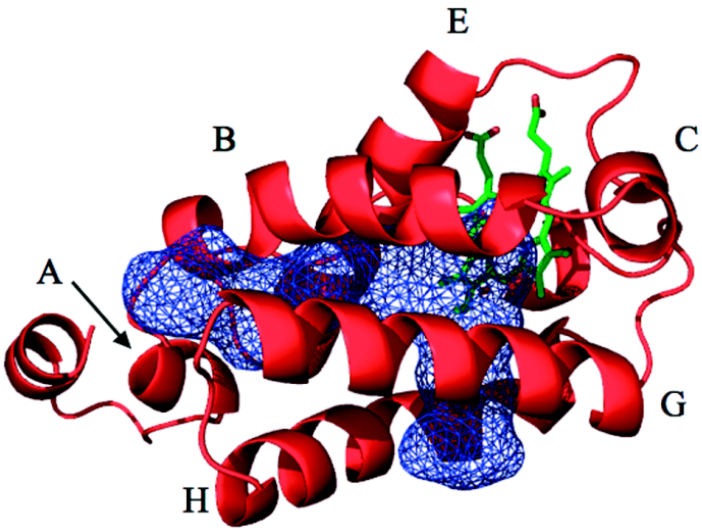

Figure 3. Representation of the two orthogonal branches of the apolar tunnel found in the protein matrix of Mt-trHbN.

In the crystal structure of the oxygenated globin (PDB code 1IDR [37]) PheE15, which is placed in the middle of the LT, shows two conformations defined by a rotation of ~63º along the C_α-C_β bond. In one conformation the benzene ring is parallel to the tunnel axis, while in the other it is roughly perpendicular. This suggests that the residue could act as a gate for ligand migration being these two conformations, which will be denoted open and closed states, respectively [37].

Molecular dynamics (MD) simulations of the oxygenated form of Mt-trHbN [10] showed several transitions between these two conformational states, in agreement with the conformational flexibility seen in the X-ray structure. In order to explore the functional implications of these findings, *Multiple Steered Molecular Dynamics* simulations coupled with Jarzinski's equality were used to obtain free energy profiles for NO migration through the tunnel for both open and closed conformations [10]. When PheE15 is in the open conformation, a small barrier (around 2 kcal/mol) has to be surpassed in order to access the heme cavity. On the other hand, for the closed state access to the active site is accompanied by a steep increase in the free energy, leading to a barrier of around 5 kcal/mol (Fig. 4). Similar studies performed for the STG8 show a higher barrier of around 7 kcal/mol. This means that NO entry for the oxygenated Mt-trHbN should mainly occur through the LT.

For the NO detoxifying reaction to take place, the protein must be firstly loaded with O_2. MD simulations run for the deoxygenated form of Mt-trHbN showed that PhE15 is only found in the closed state. This is consistent with the free energy barrier for the open/closed torsional transition obtained by

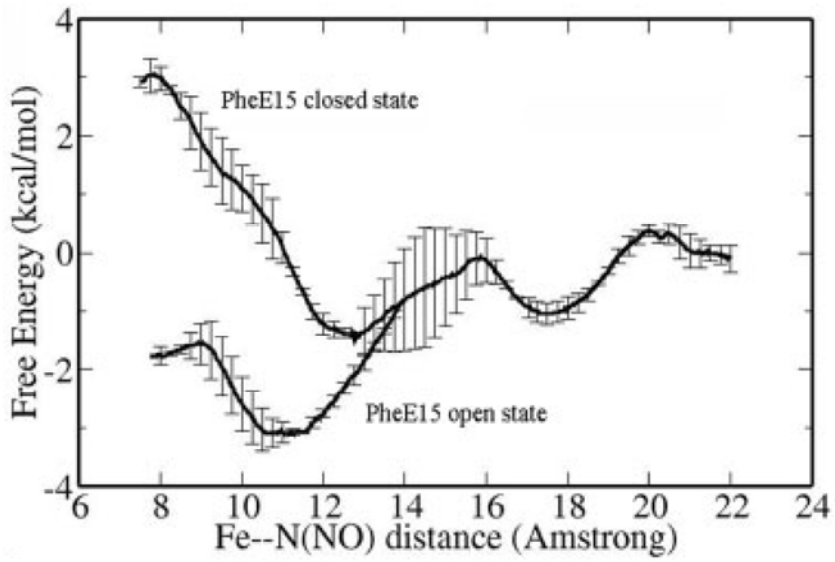

Figure 4. Free energy profile for the migration of NO through the LT in both open and closed states of the PheE15 gate.

Umbrella Sampling: while the open↔closed transition involves a barrier of 3 kcal/mol in the oxygenated protein, the barrier increases up to 6 kcal/mol in the deoxygenated protein. Oxygen entry is then supposed to be achieved through the STG8, as supported by the free energy profiles for ligand migration through this tunnel for the oxygenated and deoxygenated forms. While 7 kcal/mol are needed for NO to gain access to the active site in the oxygenated form, only 4 kcal/mol must be surpassed by O_2 in the deoxygenated form (Fig. 5).

This behavior suggests that once the Mt-trHbN-O_2 complex is formed, some residues sense the ligand in the distal cavity and favors the conformational change in PheE15, which triggers the aforementioned opening events. This allows NO to enter through the LT and reach the distal cavity for the detoxifying reaction to take place.

A plausible hypothesis to explain the sensing properties of Mt-trHbN relies on residues GlnE11 and TyrB10. In the deoxygenated protein those residues interact by hydrogen bonding between the amide group in GlnE11 and the hydroxyl group in TyrB10. MD simulations show that sometimes GlnE11 is acting as hydrogen-bond donor (and TyrB10 as acceptor), whereas in other snapshots the side chain carbonyl group of GlnE11 is hydrogen-bond acceptor (and TyrB10 is the donor). In all cases GlnE11 is primarily found in an extended *all-trans* conformation. This fluctuating hydrogen-bond network is drastically altered in the oxygenated protein. Thus, TyrB10 forms a hydrogen-bond with the heme-bound O_2 and forces GlnE11 to adopt a folded conformation in order to maintain a hydrogen-bond with TyrB10. In this conformational state, the side chain of GlnE11 is much closer to PheE15, and thermal fluctuations of the side chains would facilitate the opening of the gate.

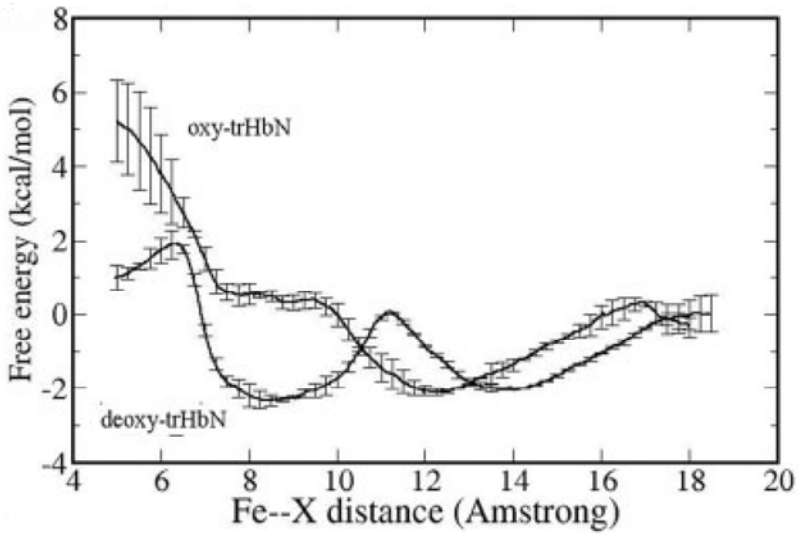

Figure 5. Free energy profile for the migration of NO through the STG8 in both deoxygenated and oxygenated states of the protein.

Support to this hypothesis also comes from MD simulations run for the TyrB10→Phe mutant [16]. Thus, the analysis of the trajectory reveals an increase in the distance between GlnE11 and PheE15, which implies a reduction in the mechanical pressure exerted by the former residue on the gate. This is due to the fact that in this mutant GlnE11 adopts an extended conformation, which enables the terminal amido group to form a hydrogen-bond directly with the heme-bound O_2. For the GlnE11→Ala mutant the protein is predicted to be also inactive, as the lack of the contacts between AlaE11 and PheE15 would make the gate to populate mainly the closed state in the mutant.

These results suggest that multiligand chemistry in Mt-HbN has evolved in such a way that there is a distinct access pathway to the active site for the molecules involved in the reaction: NO and O_2. Oxygen would first enter through the STG8 and bind to the heme. Upon oxygen binding, the hydrogen bond network formed by TyrB10 and GlnE11 is the key feature that regulates the mechanism that triggers the opening of PheE15 gate of the LT for NO entrance.

Other trHbs

Several efforts have been made in the last years to examine other trHbs by solving X-ray structures, or determining kinetic constants and spectroscopic data, as well as by using MD simulations. At this point, our group has been working on the ligand migration properties in *M. tuberculosis* trHb (Mt-trHbO) and *B. subtilis* trHb (Bs-trHbO).

For Mt-trHbO, even though a Leu residue occupies the E15 position (thus avoiding the PheE15 gate), the LT is blocked near the heme group. The only accessible tunnel for ligand migration is the Short Tunnel E7 (STE7), which is oriented toward the propionate groups (Fig. 6). This tunnel is topologically

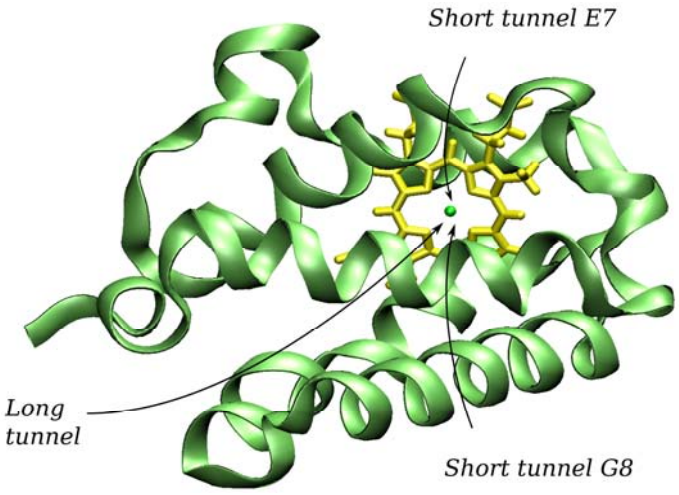

Figure 6. Representation of the backbone in Mt-trHbO and schematic view of the three main tunnels found in trHbs.

related to the E7 "gate" found in Mb. However, although STE7 showed a lower barrier for ligand migration than the LT one [11], it is even higher compared to that observed for Mt-trHbN, a fact that probably explains its low association rate.

Mutation of TrpG8 to smaller residues consistently lowers the O_2 entry barrier and increases the association rate, in agreement with the available experimental data [11]. These findings support the important role of TrpG8 in regulating the ligand migration through the LT (Fig. 7). In particular, the mutant TrpG8→Ala opens the STG8 (mentioned above for Mt-trHbN). Therefore, TrpG8 not only blocks LT, but also STG8. Noteworthy, sequence alignment shows that there is a Trp residue at position G8 along the whole O and P groups of this sub-family.

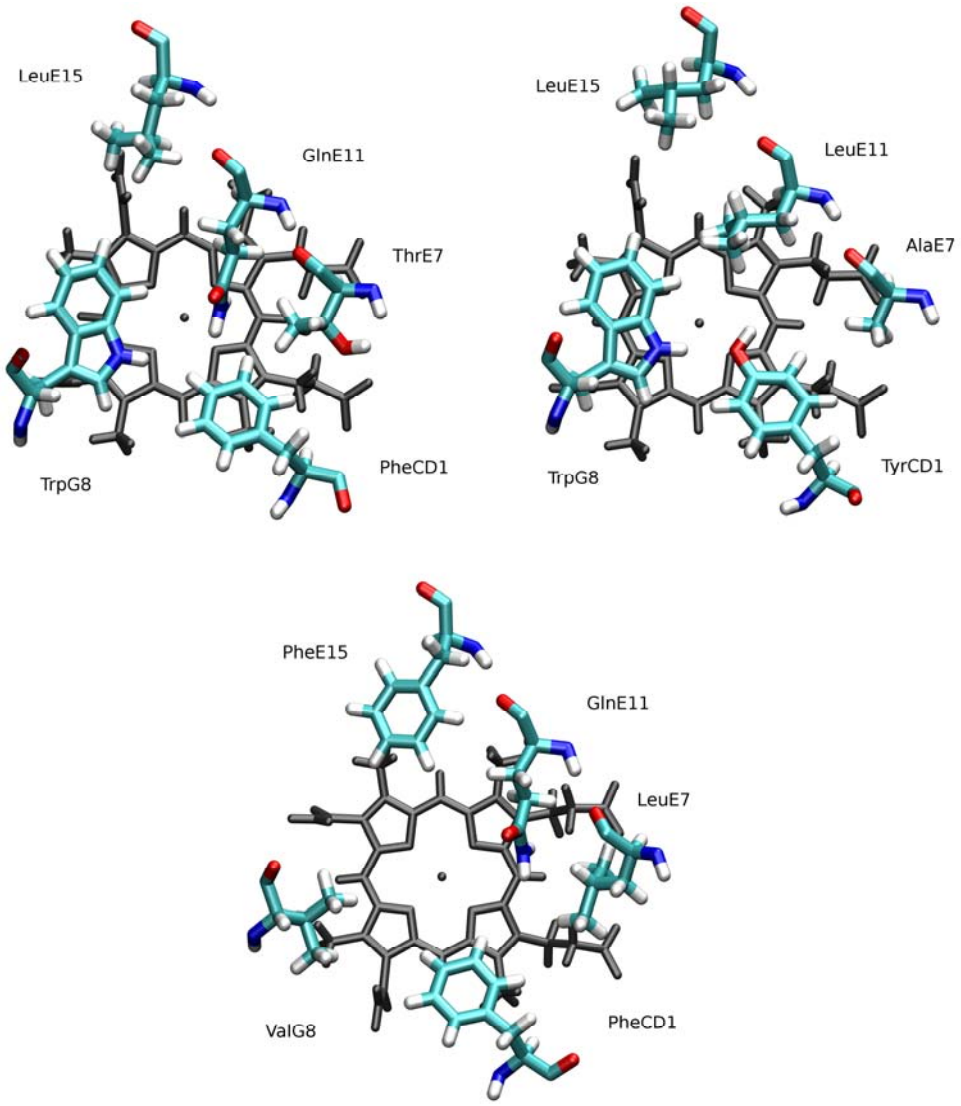

Figure 7. Representation of the main residues at the distal site in (*top, left*) Bs-trHbO, (*top, right*) Mt-trHbO, and (*bottom*) Mt-trHbN.

The case of Bs-trHbO is even more interesting. Even though inspection of the X-ray structure does not reveal a well-defined tunnel, this protein displays a high association rate [38]. The simulation results showed that GlnE11 adopts a different conformation compared to the position in the crystal structure, opening the LT (Fig. 7). Although Bs-trHbO presents TrpG8 (as in the case of Mt-trHbO), the presence of GlnE11 seems to suffice for opening of the LT. Thus, steered MD simulations run for the Bs-trHbO GlnE11→Leu mutant (designed to mimic Mt-trHbO) showed a large barrier for the migration through the LT, thus indicating that both TrpG8 and LeuE11 are responsible of blocking the LT. Although the presence of TrpG8 was expected to be enough to control ligand entry in these proteins, the presence of GlnE11 –as compared to Leu in Mt-trHbO– clearly contributes to opening of the LT and facilitates ligand entry, in agreement with the experimental values determined for the association rate constants.

Overall, this brief discussion suffices to highlight the close relationship between subtle changes in the nature of certain residues in the interior of the proteins, and the migration properties of gaseous ligands through the protein matrix of structurally related trHbs. Thus, the presence of certain residues at specific positions has a critical role in regulating ligand affinity and reactivity by controlling the barrier for migration of ligands toward the heme active site.

2. Protoglobin of *Methanosarcina acetivorans*

This section is focused in selected structural characteristics of *M. acetivorans* protoglobin (MaPgb), and particularly on the unusually distorted heme found in the X-ray structure of this protein [29], and its possible functional implications.

MaPgb contains around 190 residues and a total of 9 helices, including a pre-A segment named Z. The heme group is highly distorted (Fig. 8) and fully buried in the protein matrix. The propionates are thus inaccessible to the solvent due to the presence of extended CE and FG loops, and to a long (20 residue) N-terminal segment with no secondary structure. In general, globins host an almost planar heme and solvent exposed propionates. Therefore, the large distortion found for MaPgb suggests that heme distortion is due to some sort of tension exerted by the surrounding residues.

Figure 8. Heme distortion of (*right*) *MaPgb* compared to (*left*) the standard heme of Mb.

Access of diatomic ligands to the distal site seems feasible through a V-shaped tunnel (Fig. 9), which is topologically different from that found in other globins. Thus, two apolar tunnels connect the solvent with the heme and are delimited by the B/G (tunnel 1) and B/E (tunnel 2) helices.

As mentioned in the Introduction, the O_2 dissociation rate can be controlled by distal effects. For instance Mt-trHbN and *Ascaris* hemoglobin exhibit a very low k_{off} for O_2 due to the presence of multiple hydrogen-bond interactions [23]. In contrast to those proteins, MaPgb has no residues capable of establishing permanent hydrogen bond interactions with the ligand. The only residue that could act as hydrogen-bond donor is TyrB10, but extended MD simulations showed that TyrB10 is mainly involved in hydrogen bonding to LeuE4. Therefore, the low dissociation rate determined experimentally must be related to other mechanisms, like heme distortions.

Bikiel et al. [24] have recently examined the influence played by distinct deformations of the heme on the ligand affinity. A systematic classification of heme distortions, denoted as Normal-Coordinate Structural Decomposition (NSD), has been proposed by Jentzen and coworkers [39]. This technique identifies the most relevant out-of-plane (saddling, ruffling, doming, X-waving, Y-waving and propellering) and in-plane (meso-stretching, N-pyrrole stretching, pyrrole traslation (X,Y), breathing and pyrrole rotation) normal deformation modes that relate the structure of a distorted heme compared to a reference D_{4h} structure (Fig. 10).

Table 1 shows the difference in O_2 binding affinity for selected deformations of the heme compared to an ideal planar heme determined from

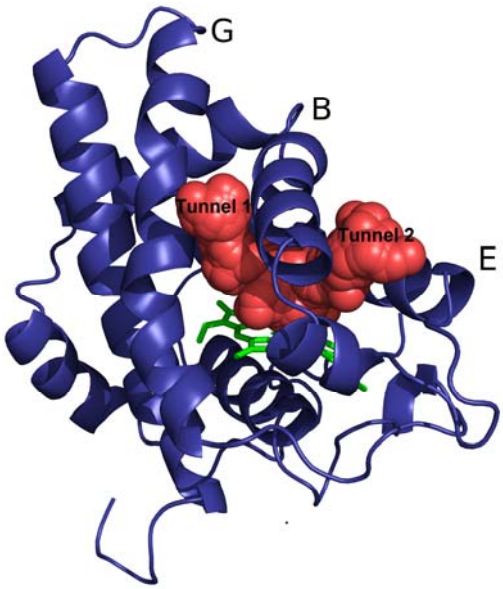

Figure 9. Representation of the V-shaped tunnel found in the X-ray structure of MaPgb.

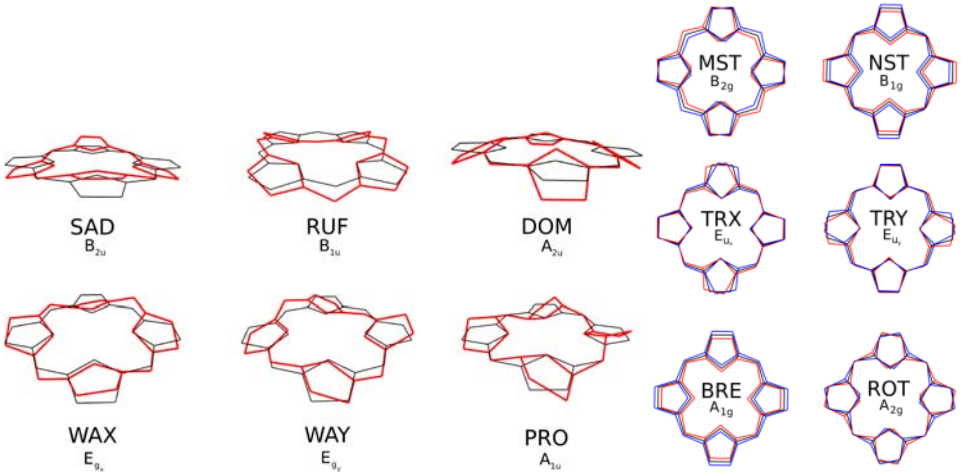

Figure 10. Representation of the normal (*left*) out-of-plane and (*right*) in-plane deformation modes of the heme.

Table 1. Difference in binding energy ($\Delta(\Delta E_{O2})$; kcal/mol) determined for selected distortions (Å) along out-of-plane and in-plane deformation modes relative to an ideal planar heme. The geometrical deviation from the planarity is measured by the root-mean square deviation (RMSD; Å).

Out-of-plane	**$\Delta(\Delta E_{O2})$**						
RMSD	**-1.2**	**-0.6**	**-0.3**	**0.0**	**0.3**	**0.6**	**1.2**
Saddling	1.9	0.5	0.1	0.0	0.1	0.5	2.4
Ruffling	2.9	0.8	0.4	0.0	-0.1	0.1	0.6
Doming	7.0	2.6	1.0	0.0	-0.3	0.0	2.1
X-waving/Y-waving	3.6	0.7	0.2	0.0	0.3	1.2	3.5
Propellering	2.2	0.5	0.1	0.0	0.1	0.5	2.2
In-plane	**$\Delta(\Delta E_{O2})$**						
RMSD	**-0.5**	**-0.25**	**-0.125**	**0.0**	**0.125**	**0.25**	**0.5**
Meso-stretching	2.1	0.8	0.2	0.0	-0.3	-0.2	0.1
N-pyrrole stretching	2.0	1.1	0.3	0.0	0.3	1.1	2.0
Pyrrole traslation X/Y	0.3	0.1	0.0	0.0	0.0	0.0	0.2
Breathing	11.3	5.6	3.1	0.0	-3.6	-6.7	-11.3
Pyrrole rotation	2.0	0.6	0.2	0.0	0.0	0.2	1.3

B3LYP/6G-31G** calculations [24]. All out-of-plane and in-plane distortions lead to an increase in the energy difference, which tends to reduce the ligand affinity. Fig. 11 shows the energy profiles arising from the ruffling (RUF) deformation as an example of this general trend: both positive and negative values of distortion decrease affinity. Only very small negative values are observed for slight distortions along the MST, DOM and RUF modes, but they do not alter the general trend. The only exception to this behavior is the in-plane BRE distortion, since a negative trend in Δ(ΔE) is clearly observed for positive values of BRE. This is represented in Fig. 11, where negative values for BRE distortion behave similarly to the rest of the normal modes, while positive values show negative Δ(ΔE), that is, compression of the heme (positive BRE) increases the ligand affinity.

The NSD analysis of the porphyrin ring in MaPgb shows that the main out-of-plane contribution to the heme deformation is ruffling, which accounts for a distortion of 1.42 Å (in Mb, this distortion only amounts to 0.02 Å). Regarding in-plane distortions, MaPgb results in a displacement around 10-fold larger compared to Mb, which is mainly due to breathing. Whereas the

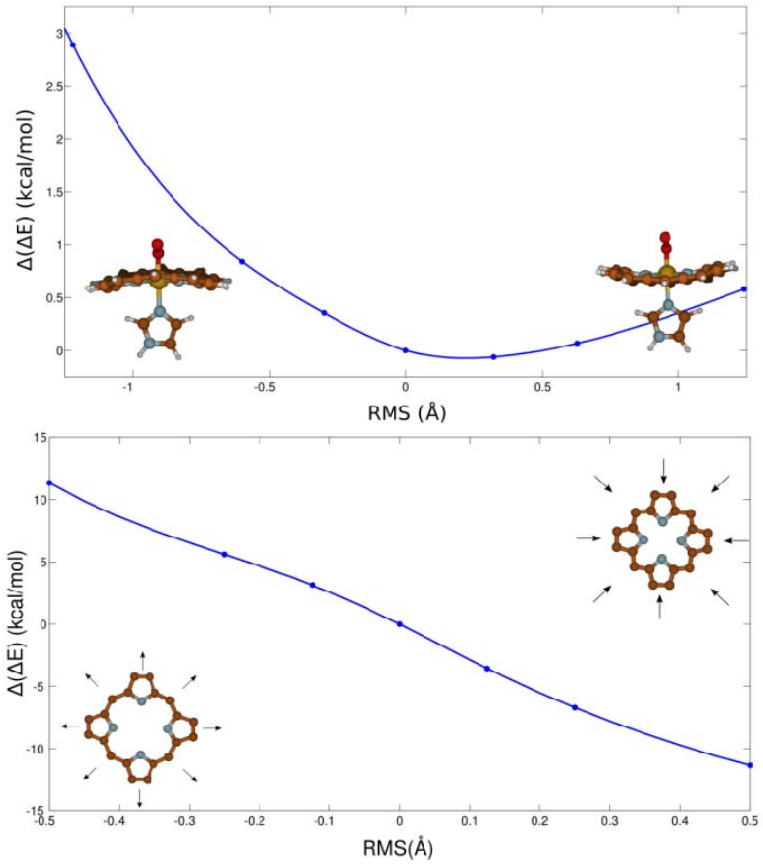

Figure 11. Representation of energy difference profiles due to (*top*) RUF and (*bottom*) BRE deformation modes.

out-of-plane distortions in MaPgb reduce the binding affinity by 1.5 kcal/mol, the positive breathing enhances ligand binding by 4.7 kcal/mol. The net effect is an overall increase in oxygen affinity for MaPgb due to heme distortion.

These findings suggest that evolution has led to the design of a tighter cavity for the heme in MaPgb, which induces an overall heme compression and in turn an increase in oxygen affinity. Although the function of MaPgb is still unkown, these results can shed light on an inherent modulation mechanism for ligand affinity in globins.

3. Neuroglobin

Neuroglobin (Ngb) is a member of the group formed by endogenous reversibly hexacoordinated globins. Many globins contain HisE7, normally responsible for O_2 stabilization by H bonding upon heme-O_2 complex is formed. However, in some globins, HisE7 is directly bound to the sixth coordination site of Fe in the heme, forming an hexacoordinated (6c) globin. This is the case of Ngb.

Ngb was firstly identified by Burmester *et al.* in 2000 [40] in man and mouse, and the X-ray structure of human and murine Ngbs have been solved [41, 42]. Later Ngb has also been identified in rat, pufferfish and zebrafish [43, 44], which suggests a widespread distribution among vertebrate species. Its function might be related to the protection of cells from stroke damage, amyloid toxicity and injury due to lack of oxygen, and neuroprotection [45]. Although the exact mechanisms by which Ngb protects cells are still unclear, it is suggested that it maintains the function of mitochondria and regulates the concentration of important chemicals in the cell. Increased risk of Alzheimer's disease has been related to low levels of Ngb [46]. Ngb mRNA and protein have been shown to be upregulated by hypoxia and post-anoxia re-oxygenation, which suggest a putative role as a reactive oxygen species scavenger [47].

Ngb is a monomeric 151-residue globin that shows less than 25% sequence identity with Mb. Though it retains the canonical 3-over-3 α-helical sandwich of mammalian Mb and Hb, notable structural deviations are found in the CD-D region and in the N-terminal half of the E helix. As a result of hexacoordination through HisE7, E helix is pulled toward the heme relative to Mb.

Pentacoordinated (5c) Ngb exhibits a very high affinity for O_2 but because of the endogenous hexacoordination, it results in a moderate O_2 affinity (P_{O2}=2 torr), similar to Mb. The reversible hexacoordination could serve as a way to fine tune the O_2 affinity. When 5c state is favoured affinity should be higher, though it also depends on the residues present in the distal cavity. This hypothesis was confirmed by experiments that drive the 5c-6c equilibrium toward the pentacoordinated state under oxidizing conditions that favor Cys disulfide bridge formation [48, 49].

MD simulations (MD), essential dynamics and steered molecular dynamics have been used to gain a molecular-level picture of the 5c↔6c transition and to estimate its thermodynamic properties [50]. Fig. 12 shows the free energy profile for the 6c to 5c transition in Cys reduced and oxidized states, called Cred and Cox, respectively. Reduction of disulfide bridge increases the barrier for the transition from 6.2 to 7.3 kcal/mol, with a 2.6 kcal/mol increase in the free energy of 5c-Cred state (relative to the 5c.Cox) state. In terms of rate constant, this implies a decrease by a factor of 6, and around 78 in the equilibrium constant.

These trends agree with the experimental results reported by Hamdane and coworkers [48, 49]. The overall conclusion is that Cys oxidation stabilizes the 5c state, favoring more avid-for-oxygen species, which supports a mechanism of oxygen release in case of hypoxic conditions, thus suggesting an O_2 storage function for Ngb. If oxygen concentration becomes critically low, the disulfide bridge in Ngb would be in the reduced state, which would in turn release oxygen to the cell. If oxygen concentration increases the disulfide bridge will form, triggering an increase in affinity for molecular oxygen.

Capece et al. [51] gained insight into the 5c↔6c equilibrium molecular determinants by means of MD simulations of Ngb and Mb at normal (1 bar) and high (3 kbar) pressure conditions in both coordination states. The overall conclusion of these studies is that the main differences between both proteins are located in the CD loop, whose structure is much more sensitive to both pressure and coordination state in Ngb than in Mb. This is reflected in the free energy profiles for the 5c↔6c transition in Ngb and Mb (Fig. 13). In Ngb the barrier increases from 7 kcal/mol at 1 bar to 13 kcal/mol at 3 kbar, with a destabilization of 4 kcal/mol of the 5c state. As shown experimentally, the

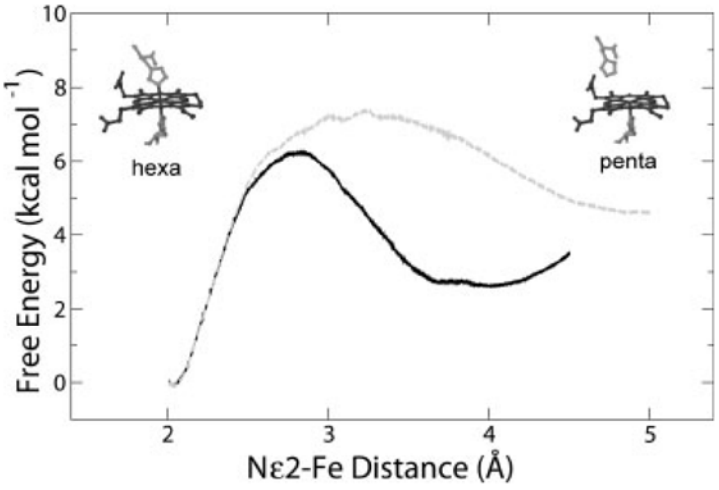

Figure 12. Free energy profile for the 5c↔6c transition with Cys residues in both reduced (gray) and oxidized (black) states.

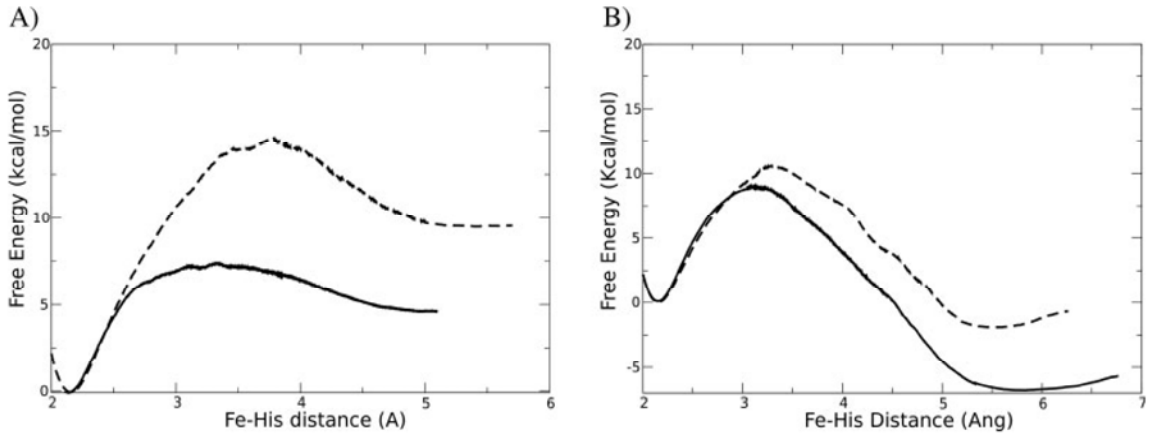

Figure 13. Free energy profile for the 5c↔6c transition at 1 bar (solid line) and 3 kbar (dashed line) in (A) Ngb and (B) Mb.

hexacoordination state is favored by an increase in pressure [52]. For Mb, the pentacoordinated state in more stable at 1 bar than the hexacoordinated state by 6 kcal/mol, whereas this difference is reduced to 1 kcal/mol at 3 kbar, with a reduction in the barrier for the transition.

Following the previous work by Nadra et al. [50], the disulfide bridge is found to have an important effect on the structure of the CD region in both coordination states, being the effect smaller than the variation with pressure. It seems that the oxidation state of the key Cys has an impact focused on the CD loop, while pressure has a more general influence on the overall structure of the protein.

The preceding results show that pressure alters the dynamics of globins, specifically reducing mobility and shifting the 5c ↔ 6c equilibrium toward the hexacoordinated state. However the reasons for this shift are different in Mb and Ngb. In Ngb, pressure mainly affects the mobility in the CD region and increases the barrier for the 5c ↔ 6c transition. In contrast, the coordination equilibrium in Mb involves a more global structural rearrangement and pressure destabilizes the 5c state. Although the overall trend for the 5c ↔ 6c transition is the same in both cases –the higher the pressure, the more favored the hexacoordination–, the underlying differences highlight the existence of diverse response mechanisms upon changes in external conditions within the globin world.

Conclusion

The advances made in the last decade on the structural and functional variation found within the globin world reinforces the idea that the thoroughly studied Mb and Hb are just specialized cases in a broad evolutionary

superfamily that evolved specifically to the demands of circulatory systems and muscles. The three cases presented here (Ngb, MaPgb and MtHbN) are representative examples of the growing diversity discovered within globins. Even though they reflect the basic chemical properties of a heme group buried in a conserved *globin fold*, it is clear that a proper understanding of the structural and dynamical differences between globins is fundamental to gain insight into the functional role of novel globins.

Acknowledgements

This work was partially supported by the University of Buenos Aires, ANPCyT (PICT-25667), CONICET, the Spanish Ministerio de Innovación y Ciencia (SAF200805595 and PCI2006-A7-0688), the Generalitat de Catalunya (2009-SGR00298), and the EU FP7 program (project NOStress).

References

1. Smith, L. J., Kahraman, A., Thornton, J. M. *Proteins ,* 78, 2349.
2. Kendrew, J. C., Bodo, G., Dintzis, H. M., Parrish, R. G., Wyckoff, H., Phillips, D. C. 1958, *Nature,* 181, 662.
3. Ghosh, A. 2007, *The smallest biomolecules: diatomics and their interactions with heme proteins*, Elsevier.
4. Paoli, M., Marles-Wright, J., Smith, A. 2002, *DNA Cell. Biol.* 21, 271.
5. Vinogradov, S. N., Moens, L. 2008, *J. Biol. Chem.,* 283, 8773.
6. Frauenfelder, H., McMahon, B. H., Fenimore, P. W. 2003, *Proc. Natl. Acad. Sci. USA,* 100, 8615.
7. Scott, E. E., Gibson, Q. H., Olson, J. S. 2001, *J. Biol. Chem.,* 276, 5177.
8. Wittenberg, J. B., Wittenberg, B. A. 2003, *J. Exp. Biol.,* 206, 2011.
9. Kapp, O. H., Moens, L., Vanfleteren, J., Trotman, C. N., Suzuki, T., Vinogradov, S. N. 1995, *Prot. Sci.,* 4, 2179.
10. Bidon-Chanal, A., Marti, M. A., Crespo, A., Milani, M., Orozco, M., Bolognesi, M., Luque, F. J., Estrin, D. A. 2006, *Proteins,* 64, 457.
11. Boechi, L., Marti, M. A., Milani, M., Bolognesi, M., Luque, F. J., Estrin, D. A. 2008, *Proteins,* 73, 372.
12. Boechi, L., Manez, P. A., Luque, F. J., Marti, M. A., Estrin, D. A. 2009, *Proteins,* 78, 962.
13. Nadra, A. D., Martí, M. A., Pesce, A., Bolognesi, M., Estrin, D. A. 2007, *Proteins,* 71, 695.
14. Brunori, M., Vallone, B. 2007, *Cell. Mol. Life Sci.,* 64, 1259.
15. Lama, A., Pawaria, S., Bidon-Chanal, A., Anand, A., Gelpi, J. L., Arya, S., Marti, M., Estrin, D. A., Luque, F. J., Dikshit, K. L. 2009, *J. Biol. Chem.,* 284, 14457.
16. Bidon-Chanal, A., Marti, M. A., Estrin, D. A., Luque, F. J. 2007, *J. Am. Chem. Soc.,* 129, 6782.

17. Goldbeck, R. A., Pillsbury, M. L., Jensen, R. A., Mendoza, J. L., Nguyen, R. L., Olson, J. S., Soman, J., Kliger, D. S., Esquerra, R. M. 2009, *J. Am. Chem. Soc.,* 131, 12265.
18. Goldbeck, R. A., Bhaskaran, S., Ortega, C., Mendoza, J. L., Olson, J. S., Soman, J., Kliger, D. S., and Esquerra, R. M. 2006, *Proc. Natl. Acad. Sci. USA,* 103, 1254
19. Ouellet, Y. H., Daigle, R., Laguee, P., Dantsker, D., Milani, M., Bolognesi, M., Friedman, J. M., Guertin, M. 2008, *J. Biol. Chem.,* 283, 27270.
20. Laverman, L. E., Ford, P. C. 2001, *J. Am. Chem. Soc.,* 123, 11614.
21. Milani, M., Pesce, A., Nardini, M., Ouellet, H., Ouellet, Y., Dewilde, S., Bocedi, A., Ascenzi, P., Guertin, M., Moens, L., Friedman, J. M., Wittenberg, J. B., Bolognesi, M. 2005, *J. Inorg. Biochem.,* 99, 97.
22. Bikiel, D. E., Boechi, L., Capece, L., Crespo, A., De Biase, P. M., Di Lella, S., González Lebrero, M. C., Martí, M. A., Nadra, A. D., Perissinotti, L. L., Scherlis, D. A., Estrin, D. A. 2006, *Phys. Chem. Chem. Phys.,* 8, 5611.
23. Marti, M. A., Crespo, A., Capece, L., Boechi, L., Bikiel, D. E., Scherlis, D. A., Estrin, D. A. 2006, *J. Inorg. Biochem.,* 100, 761.
24. Bikiel, D. E., Forti, F., Boechi, L., Nardini, M., Luque, F. J., Martí, M. A., Estrin, D. A. 2010, *J. Phys. Chem. B,* 114, 8536.
25. Vinogradov, S. N., Hoogewijs, D., Bailly, X., Mizuguchi, K., Dewilde, S., Moens, L., Vanfleteren, J. R. 2007, *Gene,* 398, 132.
26. Vinogradov, S., Hoogewijs, D., Bailly, X., Arredondo-Peter, R., Gough, J., Dewilde, S., Moens, L., Vanfleteren, J. 2006, *BMC Evol. Biol.,* 6, 31.
27. Freitas, T. A. K., Hou, S., Dioum, E. M., Saito, J. A., Newhouse, J., Gonzalez, G., Gilles-Gonzalez, M.-A., Alam, M. 2004, *Proc. Natl. Acad. Sci. USA,* 101, 6675.
28. Hou, S., Freitas, T., Larsen, R. W., Piatibratov, M., Sivozhelezov, V., Yamamoto, A., Meleshkevitch, E. A., Zimmer, M., Ordal, G. W., Alam, M. 2001, *Proc. Natl. Acad. Sci. USA,* 98, 9353.
29. Nardini, M., Pesce, A., Thijs, L., Saito, J. A., Dewilde, S., Alam, M., Ascenzi, P., Coletta, M., Ciaccio, C., Moens, L., Bolognesi, M. 2008, *EMBO Rep.,* 9, 157.
30. Tomita, A., Sato, T., Ichiyanagi, K., Nozawa, S., Ichikawa, H., Chollet, M., Kawai, F., Park, S.-Y., Tsuduki, T., Yamato, T., Koshihara, S.-Y., Adachi, S.-I. 2009, *Proc. Natl. Acad. Sci. USA,* 106, 2612.
31. Ordway, G. A., Garry, D. J. 2004, *J. Exp. Biol.,* 207, 3441.
32. Bloom, B. 1994, *Tuberculosis: pathogenesis, protection and control*, ASM Press, Washington, DC.
33. MacMicking, J. D., North, R. J., LaCourse, R., Mudgett, J. S., Shah, S. K., Nathan, C. F. 1997, *Proc. Natl. Acad. Sci. USA,* 94, 5243.
34. Ouellet, H., Ouellet, Y., Richard, C., Labarre, M., Wittenberg, B., Wittenberg, J., Guertin, M. 2002, *Proc. Natl. Acad. Sci. USA,* 99, 5902.
35. Couture, M., Yeh, S.-R., Wittenberg, B. A., Wittenberg, J. B., Ouellet, Y., Rousseau, D. L., Guertin, M. 1999, *Proc. Natl. Acad. Sci. USA,* 96, 11223.
36. Pesce, A., Nardini, M., Milani, M., Bolognesi, M. 2007, *IUBMB Life*, 59, 535.
37. Milani, M., Pesce, A., Ouellet, Y., Ascenzi, P., Guertin, M., Bolognesi, M. 2001, *EMBO J.,* 20, 3902.

38. Giangiacomo, L., Ilari, A., Boffi, A., Morea, V., Chiancone, E. 2005, *J. Biol. Chem.,* 280, 9192.
39. Jentzen, W., Song, X. Z., Shelnutt, J. A. 1997, *J. Phys. Chem. B,* 101, 1684.
40. Burmester, T., Weich, B., Reinhardt, S., Hankeln, T. 2000, *Nature,* 407, 520.
41. Pesce, A., Dewilde, S., Nardini, M., Moens, L., Ascenzi, P., Hankeln, T., Burmester, T., Bolognesi, M. 2003, *Structure,* 11, 1087.
42. Vallone, B., Nienhaus, K., Brunori, M., Nienhaus, G. U. 2004, *Proteins,* 56, 85.
43. Awenius, C., Hankeln, T., Burmester, T. 2001, *Biochem. Biophys. Res. Commun.,* 287, 418.
44. Zhang, C., Wang, C., Deng, M., Li, L., Wang, H., Fan, M., Xu, W., Meng, F., Qian, L., He, F. 2002, *Biochem. Biophys. Res. Commun.,* 290, 1411.
45. Greenberg, D. A., Jin, K., Khan, A. A. 2008, *Curr. Opin. Pharmacol.,* 8, 20.
46. Raychaudhuri, S., Skommer, J., Henty, K., Birch, N., Brittain, T. 2009, *Apoptosis,* 15, 401.
47. Nayak, G. H., Milton, S. L., Prentice, H. M. 2007, *FASEB J.,* 21, A924.
48. Hamdane, D., Kiger, L., Dewilde, S., Green, B. N., Pesce, A., Uzan, J., Burmester, T., Hankeln, T., Bolognesi, M., Moens, L., Marden, M. C. 2004, *Micron,* 35, 59.
49. Hamdane, D., Kiger, L., Dewilde, S., Green, B. N., Pesce, A., Uzan, J., Burmester, T., Hankeln, T., Bolognesi, M., Moens, L., and Marden, M. C. 2003, *J Biol. Chem.,* 278, 51713
50. Nadra, A. D., Martí, M. A., Pesce, A., Bolognesi, M., Estrin, D. A. 2008, *Proteins,* 71, 695.
51. Capece, L., Marti, M. A., Bidon-Chanal, A., Nadra, A., Luque, F. J., Estrin, D. A. 2008, *Proteins,* 75, 885.
52. Hamdane, D., Kiger, L., Hoa, G. H. B., Dewilde, S., Uzan, J., Burmester, T., Hankeln, T., Moens, L., Marden, M. C., 2005, *J. Biol. Chem.,* 280, 36809.